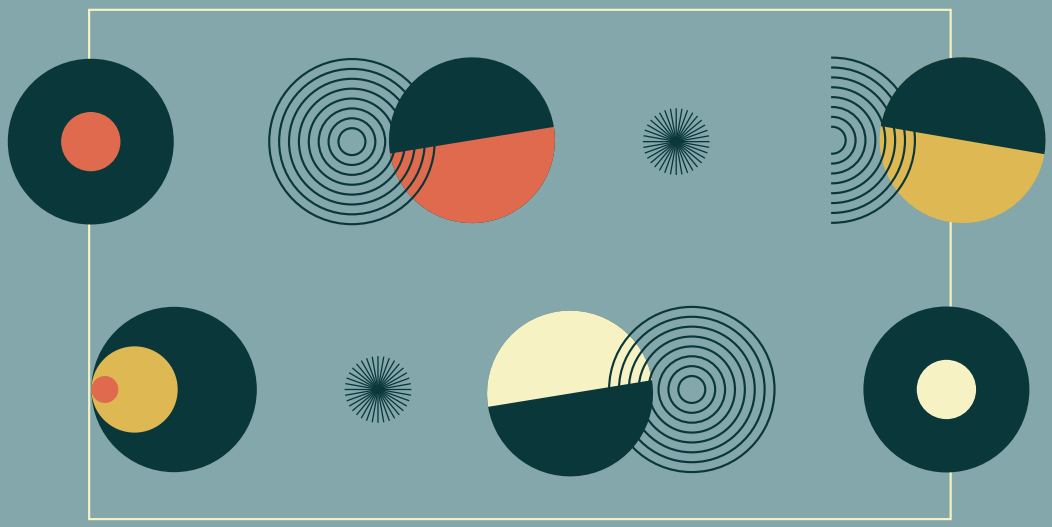

MRI for planning and characterization of uveal melanoma patients treated with proton beam therapy

Myriam Jaarsma-Coes

MRI for planning and characterization of uveal melanoma patients treated with proton beam therapy

Myriam Jaarsma-Coes

MRI for planning and characterization of uveal melanoma patients treated with proton beam therapy

Proefschrift

ter verkrijging van
de graad van doctor aan de Universiteit Leiden,
op gezag van rector magnificus prof. dr. ir. H. Bijl,
volgens besluit van het college voor promoties
te verdedigen op donderdag 2 februari 2023
klokke 10:00 uur

door

Myriam Jaarsma-Coes
geboren te Gouda
in 1991

Promotoren

Prof. dr. A.G. Webb[1]
Prof. dr. G.P.M. Luyten[2]

Copromotor

dr.J.W.M. Beenakker[1,2,3]

Promotiecommissie

Prof. dr. ir. M.P.J. van Osch[1]
dr. P. de Graaf[4]
Prof. dr. M.S. Hoogeman[5]
Prof. dr. M.J. Jager[2]
Prof. dr. A.M. Joussen[6]

[1] *Radiology, C.J. Gorter MRI Centre, Leiden University Medical Centre*
[2] *Ophthalmology, Leiden University Medical Centre*
[3] *Radiation oncology, Leiden University Medical Centre*
[4] *Radiology and Nuclear Medicine, Amsterdam UMC Locatie VUmc*
[5] *Radiation Oncology, Erasmus medical center*
[5] *Ophthalmology, Charité, Berlin, Germany*

This work is part of the research program 'Protons4Vision' with project number 14654, which is financed by the Dutch Research Council (NWO). Typesetting by M.G. Jaarsma-Coes in LaTeX. Cover design by M.G. Jaarsma-Coes.

An electronic version of this dissertation is available at the Leiden University Repository.

Contents

1

General introduction

Uveal melanoma (UM) arises from melanocytes and is the most common primary intraocular tumour in adults, occurring at a rate of approximately 14 cases per million person-years[1,2]. UM is a deadly disease, as up to 50% of the UM patients die from metastases[3], although this varies as the 5 year metastasis-free survival for ruthenium brachytherapy patients was 6.2%[4]. The diagnosis of UM is commonly based on clinical characteristics obtained by an ophthalmologist using fundoscopy, fluorescein angiography and ultrasound imaging[5,6], as for example in figure 1.1. UM is often visible as an (un)pigmented lesion with fundoscopy where the fundus is studied using a magnifying lens and a light, as shown in figure 1.1A. With fluorescein angiography, a contrast agent (fluorescein) is administered intravenously and the fundus is imaged every few seconds for several minutes using a special camera. UM generally enhances and shows pinpoint leakage after several minutes[7]. Finally, ultrasound is mostly used to determine the size of the lesion, although the internal reflectivity (low or intermediate as in figure 1.1C) can also be an indication of UM[6,8].

UM is most commonly treated with radiotherapy or enucleation. At the LUMC these patients are often treated with Ru-106 brachytherapy if the tumour is smaller than 16mm in diameter and the prominence is less than 7mm[4]. For larger tumours or tumours in close proximity to the optic disk, proton beam therapy is available at the HollandPTC since December 2019. With the increased availability of proton beam therapy (PT), the number of patients treated with ocular PT is rising[9].

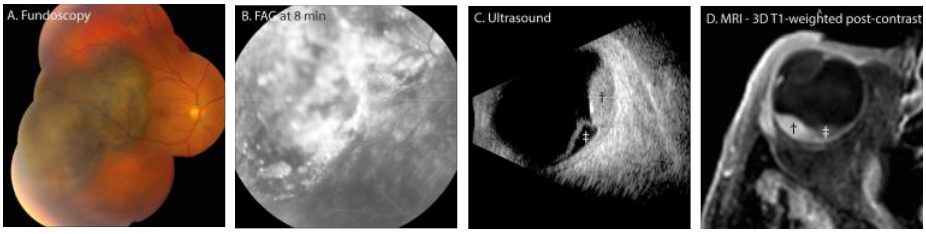

Figure 1.1: (A-C) Conventional ophthalmic imaging of UM. The fundus photo (A) shows a pigmented lesion. The lesion enhances, shown as pinpoints on the fluorescent angiography (FAG, B). On ultrasound (C), the lesion (dagger) has an intermediate reflectivity, while the retinal detachment (double dagger) has a low reflectivity. On MRI, an enhancing lesion (dagger) with associated retinal detachment (double dagger) are visible (D).

In preparation for ocular PT, radiopaque (tantalum) markers are sutured to the sclera near the tumour border by an ophthalmologist for treatment planning and position verification during treatment[10]. Currently, data from different, mostly ophthalmic, sources, such as ultrasound and fundoscopy, are combined to create a geometrical tumour-and-eye model[9,11]. In this model,the dimensions of the eye are scaled to the axial length, as obtained by biometry. Additionally, several other parameters such as limbus diameter can be personalised. The tumour geometry is primarily based on its prominence and basal diameters, as obtained from ocular ultrasound, while perioperatively obtained marker-tumour distances and fundus photographs are used to define the tumour base.

An alternative imaging method to US, that is commonly used in radiology and radiotherapy is magnetic resonance imaging (MRI). MRI has been used to image UM since the 1980s [12, 13], although the clinical value was limited in the first decades due to the low image quality. At the start of this research project in 2017, ocular MRI was not yet widely used clinically. However, in research settings many steps had already been taken at the LUMC to make ocular MRI possible on a high field (7T) MRI[14]. Moreover, it had been shown that MRI can have important clinical implications, as it can yield a more accurate measurement of the tumour dimension, which can even lead to a different treatment[15]. During this project I worked on technical aspects regarding MRI-based proton-beam planning. In the meantime, I also worked together with our team at the LUMC, currently one of the leading centres for ocular MRI, to develop and evaluate a modern ocular MRI protocol and make ocular MRI available for patients in the clinic[16,17].

1.1 Uveal melanoma on MRI

MRI is fundamentally different than conventional ophthalmic imaging modalities, such as ultrasound and fundoscopy, as it uses a combination of radio waves and a strong magnetic field to create an image. As the image contrast in MRI is a result of differences in the tissue's magnetic properties, different biological aspects, such as the tissue's cellularity, can be probed. This allows for evaluation of a entirely different range of tissue properties, such as quantitative MRI biomarkers of tumour perfusion and cellular density, which proved to aid in the diagnosis and follow-up of patients with uveal melanoma and other types of intraocular masses[17–21].

At the Gorter MRI center (LUMC) we started with ocular MRI on the ultra-high-field research MRI[15] and transitioned these techniques to regular clinical MRI scanners to make MRI available for patients in the clinic[16,17]. The protocol I developed together with my colleagues contains both 2D and 3D anatomical sequences and functional imaging[16,22,23]. The 2D sequences are particularly useful to evaluate anatomy, layer of origin, and also to assess the margins and shape of the lesion, while the 3D sequences enable assessment of tumour geometry and visualisation at all angles (figure 1.3D). This proved to be valuable in the determination of the tumour extent in the context of therapy selection[15–17]. The possibilities for the use of MRI in conventional ocular PT planning and follow-up after treatment will be discussed in chapter 4 and the discussion (chapter 7).

In MRI, multiple images with different contrasts are generally jointly evaluated. For the eye, these contrasts should at least include T2-weighted scans and T1-weighted scans, where the latter should be acquired before and after administration of an intravenous contrast agent, such as gadolinium (figure 1.2A-C). These contrasts provide complementary information needed to differentiate different pathologies such as uveal melanoma, associated retinal detachment necrosis and other treatment-related effects[24–27].

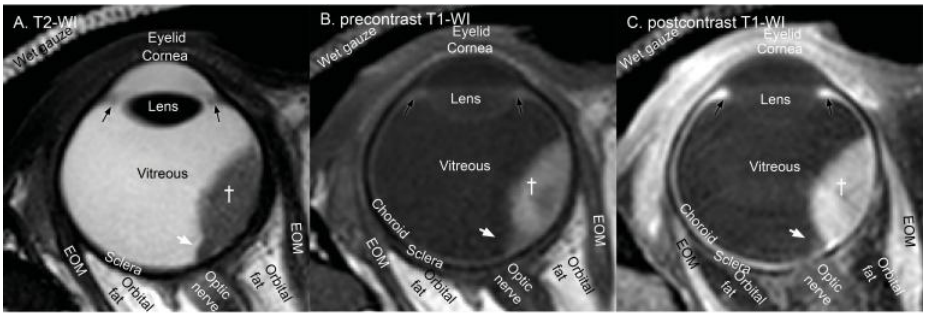

Figure 1.2: Transversal anatomical MR-images of a patient with a uveal melanoma (dagger) and associated retinal detachment (white arrow). (A) T2-weighted imaging showing a hypointense tumour. (B) T1-weighted imaging before contrast agent without fat suppression and (C)T1-weighted imaging after contrast agent administration with fat suppression showing an hyperintense tumour which is enhancing. Note that the choroid, extra ocular muscles (EOM), ciliary body (black arrow) and eyelid which enhances.

The signal intensity characteristics of UM have been described extensively[14–18,21,23,28–49]. Most importantly, all UM enhance after contrast administration. Almost all intraocular lesions, including UM, are hyperintense on T1- and hypointense on T2-weighted imaging (WI) compared to the vitreous. Therefore, we proposed to use the signal intensity of the choroid as reference on T1-WI and the nearby extra-ocular muscle on T2-WI[17]. We found that UM are mostly hyperintense compared to the muscle on T2-WI and hyperintense or isointense compared to the choroid on T1-WI. The signal intensity on T1 is significantly related to pigmentation[17,34], which is also clearly visible in figure 1.3B. This figure shows that the melanotic part (figure 1.3B, blue arrow) is more hyperintense compared to the amelanotic part (figure 1.3B, pink arrow). These characteristics are an important first step to differentiate UM from other intraocular masses.

Detachments of the retina and choroid can be identified based on signal intensity and morphology[27,50]. The signal intensity of retinal detachment varies, based on its contents[23] and can have a similar signal intensity as the UM (figure 1.2A,B, arrow). Therefore, postcontrast T1 scans are important to differentiate retinal detachment from UM, as retinal detachment does not enhance (figure 1.2B,C, arrow)[16,17,27]. Retinal detachment has been observed with MRI in approximately 2/3 of the UM[17,40], however, with low resolution MR-images small retinal detachment might be missed[51]. In contrast to retinal detachment, necrosis and inflammation are better depicted on T2-WI[27]. This is illustrated in figure 1.3, which shows that the necrotic core that is visible on T2-WI (figure 1.3A, yellow arrow) is not visible on the pre-contrast T1-WI (figure 1.3B).

One of the advantages of MRI, compared to ultrasound and fundoscopy, is that the complete orbit can be evaluated, allowing for a more accurate screening for extrascleral extension, optic nerve invasion and inflammatory processes[17,23,52–70]. MRI generally outperforms ultrasound in the screening for extrascleral extension (figure 1.3C)[17,56,66,70].

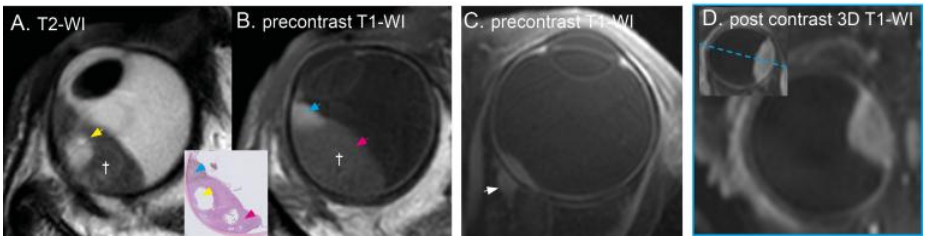

Figure 1.3: (A-C) patient with necrosis (A, yellow arrow) in a bilobar tumour. The amelanotic lobe (B, pink arrow) is isointense to the choroid whereas the melanotic lobe (B, blue arrow) is hyperintense compared to the choroid on the T1 weighted scan before contrast agent administration and was confirmed with histopathology (Insert, adapted with permission from Ferreira et al.[17]). (C) Extra ocular extension is best visualized on the post contrast T1-weighted scan with fat suppression. D) Volumetric scans (3D) allow for measurements of the tumour dimensions in all directions as the scan can be visualized in every arbitrary direction.

1.2 Functional scans

In addition to these anatomical assessments, MRI can provide multiple quantitative imaging contrasts and biomarkers[39,71–73]. One of the most commonly functional-MRI techniques used in oncology is perfusion weighted imaging (PWI). This technique has proved to be valuable in other types of malignancies and has been reported to aid in the differential diagnosis and assessment of therapy response.

In PWI, similarly as in fluorescein angiography, an image is acquired every few seconds during contrast administration and the following minutes (figure 1.4A,B). In contrast to fluorescein angiography, the complete lesion, and not only its ventral surface, can be assessed in 3D. With our newly developed protocol it is possible to acquire a 3D image with a resolution of 1.5mm isotropic every 2 seconds[16].

1.3 This thesis

This thesis is part of the Protons4Vision project which aims to improve the accuracy of proton-beam therapy and ultimately save the patient's vision without the need for surgery for marker placement by (I) developing high-resolution MRI techniques to localize UM in three dimensions, (II) develop techniques to plan ocular PT on MRI and (III) develop techniques to track eye motion at the ocular PT site and inside the MRI. In this thesis I will focus on the first part of the project: to develop high-resolution ocular MRI.

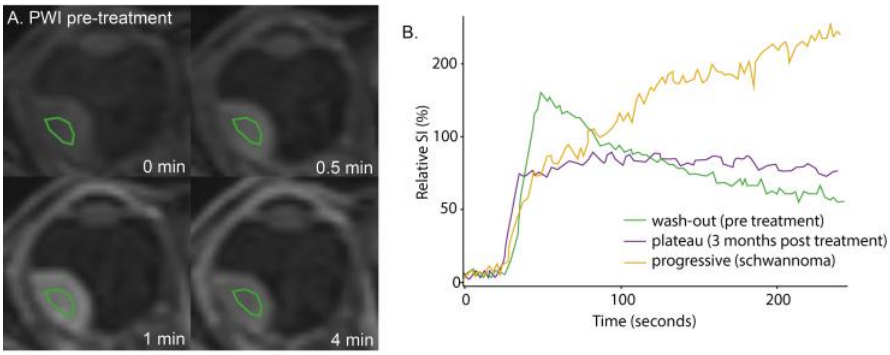

Figure 1.4: (A) Four timepoints of the DCE-MRI of a patient before treatment, showing increase in signal in the tumour at timepoint 0.5 & 1 min and decrease in signal towards the end of the scan (4 min) resulting in the green time intensity curve (B). (B) Three different time intensity curves (TICs). A wash-out TIC of a patient before after treatment showing which changed into a plateau TIC 3 months after treatment. A progressive curve has been observed in a patient with a schwannoma.

Before MRI-based-ocular PT planning can be implemented, two main topics need to be addressed. Firstly, MRI scans are performed with the patient in the prone position, while ocular PT is performed with the patient in the "seated" position. This change in orientation with respect to that of gravitational pull might induce a geometric mismatch in tumour and/or eye shape between both postures. Therefore, we have assessed the effect of body pose on the eye- and tumour-shape in **chapter 2**. Secondly, the inter-observer variation of the gross target volume (GTV) is one of the important parameters to design safety margins for a reliable treatment. The inter-observer variation of the GTV delineation based on MRI was investigated in **chapter 3**.

In December 2019, the HollandPTC started to treat UM patients with proton-beam therapy. As MRI-based planning is not yet available, conventional planning is used at the HollandPTC. Conventional ocular PT is planned using measurements obtained by an ophthalmologist using ultrasound, fundoscopy, biometry and intraoperative assessments. I have developed a dedicated MR protocol for ocular PT planning and evaluated it with all parties involved. This protocol and its evaluation are described in **chapter 4**. With this protocol it is now possible to acquire high-resolution three-dimensional images of the eye, providing the opportunity to use MRI based measurements in the current ocular PT planning workflow.

Uveal melanoma can be complicated by exudative retinal detachment (RD). Sometimes, exudative RD is mistaken for a rhegmatogenous detachment and subsequently treated with vitrectomy with silicone oil (SiOil) tamponade. We have also seen patients with SiOil where a mass was found during lens-replacement surgery. The diagnosis, treatment planning and/or follow-up of UM underlying the detachment are often severely hindered due to the presence of SiOil. In **chapter 5** a dedicated MRI protocol for patients with SiOil was developed and subsequently evaluated pro-

viding new opportunities for diagnosis, treatment planning and/or follow-up of these patients.

Finally, MRI provides the opportunity to do functional imaging. In addition to the signal intensity, the exact concentration of contrast agent can be estimated, which provides quantitative information on the tissue's microvasculature[34,37,74]. However, reliable quantitative analysis is challenging due to eye motion during the long period of scanning, an inhomogeneous magnetic field and differences in pigmentation of UM. In **chapter 6**, these challenges in the analysis of dynamic contrast-enhanced MRI of patients with intraocular masses will be addressed.

1.4 References

[1] IKNL, *NKR cijfers*. [Online]. Available: https://iknl.nl/nkr-cijfers.

[2] A. D. Singh, M. E. Turell, and A. K. Topham, "Uveal melanoma: Trends in incidence, treatment, and survival," *Ophthalmology*, vol. 118, no. 9, pp. 1881–1885, 2011, ISSN: 01616420. DOI: 10.1016/j.ophtha.2011.01.040.

[3] C. D. Roelofsen *et al.*, "Five decades of enucleations for uveal melanoma in one center: More tumors with high risk factors, no improvement in survival over time," *Ocular Oncology and Pathology*, vol. 7, no. 2, pp. 133–141, 2021.

[4] M. Marinkovic *et al.*, "Ruthenium-106 brachytherapy for choroidal melanoma without transpupillary thermotherapy: Similar efficacy with improved visual outcome," *European Journal of Cancer*, vol. 68, pp. 106–113, 2016.

[5] C. L. Shields *et al.*, "Choroidal nevus transformation into melanoma: Analysis of 2514 consecutive cases," *Arch Ophthalmol*, vol. 127, no. 8, pp. 981–7, 2009, ISSN: 0003-9950. DOI: 10.1001/archophthalmol.2009.151.

[6] M. J. Jager *et al.*, "Uveal melanoma," *Nat Rev Dis Primers*, vol. 6, no. 1, p. 24, 2020, ISSN: 2056-676x. DOI: 10.1038/s41572-020-0158-0.

[7] J. Shields, C. Shields, P. De Potter, and A. Singh, "Diagnosis and treatment of uveal melanoma," *Seminars in oncology*, vol. 23, no. 6, pp. 763–767, Dec. 1996, ISSN: 0093-7754. [Online]. Available: http://europepmc.org/abstract/MED/8970600.

[8] B. H. Lorek, M. E. Aronow, and A. D. Singh, "Diagnostic techniques: Ophthalmic ultrasonography," in *Clinical Ophthalmic Oncology*, Springer, 2014, pp. 215–235.

[9] J. Hrbacek *et al.*, "Practice patterns analysis of ocular proton therapy centers: The international optic survey," *Int J Radiat Oncol Biol Phys*, vol. 95, no. 1, pp. 336–343, 2016, ISSN: 0360-3016. DOI: 10.1016/j.ijrobp.2016.01.040.

[10] K. K. Mishra and I. K. Daftari, "Proton therapy for the management of uveal melanoma and other ocular tumors," *Chinese Clinical Oncology*, 2016, ISSN: 23043873. DOI: 10.21037/cco.2016.07.06.

[11] M. Marinkovic *et al.*, "Clinical outcomes after international referral of uveal melanoma patients for proton therapy," *Cancers*, vol. 13, no. 24, p. 6241, 2021.

[12] R. J. de Keizer, G. J. Vielvoye, and D. de Wolff-Rouendaal, "Nuclear magnetic resonance imaging of intraocular tumors," *Am J Ophthalmol*, vol. 102, no. 4, pp. 438–41, 1986, ISSN: 0002-9394 (Print) 0002-9394. DOI: 10.1016/0002-9394(86)90070-x.

[13] R. C. Hawkes, G. N. Holland, W. S. Moore, S. Rizk, B. S. Worthington, and D. M. Kean, "Nmr imaging in the evaluation of orbital tumors," *AJNR Am J Neuroradiol*, vol. 4, no. 3, pp. 254–6, 1983, ISSN: 0195-6108 (Print) 0195-6108.

[14] J. W. Beenakker, G. A. van Rijn, G. P. Luyten, and A. G. Webb, "High-resolution mri of uveal melanoma using a microcoil phased array at 7 t," *NMR Biomed*, vol. 26, no. 12, pp. 1864–9, 2013, ISSN: 0952-3480. DOI: 10.1002/nbm.3041. [Online]. Available: https://analyticalsciencejournals.onlinelibrary.wiley.com/doi/pdfdirect/10.1002/nbm.3041?download=true.

[15] J. W. Beenakker *et al.*, "Clinical evaluation of ultra-high-field mri for three-dimensional visualisation of tumour size in uveal melanoma patients, with direct relevance to treatment planning," *Magma*, vol. 29, no. 3, pp. 571–7, 2016, ISSN: 0968-5243 (Print) 0968-5243. DOI: 10.1007/s10334-016-0529-4. [Online]. Available: https://www.ncbi.nlm.nih.gov/pmc/articles/PMC4891368/pdf/10334_2016_Article_529.pdf.

[16] T. A. Ferreira, L. Grech Fonk, M. G. Jaarsma-Coes, G. G. R. van Haren, M. Marinkovic, and J. M. Beenakker, "Mri of uveal melanoma," *Cancers (Basel)*, vol. 11, no. 3, 2019, ISSN: 2072-6694 (Print) 2072-6694. DOI: 10.3390/cancers11030377.

[17] T. A. Ferreira *et al.*, "Mr imaging characteristics of uveal melanoma with histopathological validation," *Neuroradiology*, 2021, ISSN: 0028-3940. DOI: 10.1007/s00234-021-02825-5.

[18] P. V. Foti *et al.*, "Uveal melanoma: Quantitative evaluation of diffusion-weighted mr imaging in the response assessment after proton-beam therapy, long-term follow-up," *Radiol Med*, vol. 122, no. 2, pp. 131–139, 2017, ISSN: 0033-8362. DOI: 10.1007/s11547-016-0697-3.

[19] A. R. Sepahdari, V. K. Aakalu, P. Setabutr, M. Shiehmorteza, J. H. Naheedy, and M. F. Mafee, "Indeterminate orbital masses: Restricted diffusion at mr imaging with echo-planar diffusion-weighted imaging predicts malignancy," *Radiology*, vol. 256, no. 2, pp. 554–64, 2010, ISSN: 0033-8419. DOI: 10.1148/radiol.10091956.

[20] A. R. Sepahdari, L. S. Politi, V. K. Aakalu, H. J. Kim, and A. A. Razek, "Diffusion-weighted imaging of orbital masses: Multi-institutional data support a 2-adc threshold model to categorize lesions as benign, malignant, or indeterminate," *AJNR Am J Neuroradiol*, vol. 35, no. 1, pp. 170–5, 2014, ISSN: 0195-6108 (Print) 0195-6108. DOI: 10.3174/ajnr.A3619.

[21] Y. Yuan, X. P. Kuai, X. S. Chen, and X. F. Tao, "Assessment of dynamic contrast-enhanced magnetic resonance imaging in the differentiation of malignant from benign orbital masses," *Eur J Radiol*, vol. 82, no. 9, pp. 1506–11, 2013, ISSN: 0720-048x. DOI: 10.1016/j.ejrad.2013.03.001.

[22] P. de Graaf *et al.*, "Guidelines for imaging retinoblastoma: Imaging principles and mri standardization," *Pediatr Radiol*, vol. 42, no. 1, pp. 2–14, 2012, ISSN: 0301-0449 (Print) 0301-0449. DOI: 10.1007/s00247-011-2201-5.

[23] P. V. Foti *et al.*, "Diagnostic methods and therapeutic options of uveal melanoma with emphasis on mr imaging-part i: Mr imaging with pathologic correlation and technical considerations," *Insights Imaging*, vol. 12, no. 1, p. 66, 2021, ISSN: 1869-4101 (Print) 1869-4101. DOI: 10.1186/s13244-021-01000-x.

[24] P. V. Foti *et al.*, "Histopathologic and mr imaging appearance of spontaneous and radiation-induced necrosis in uveal melanomas: Initial results," *Cancers (Basel)*, vol. 14, no. 1, 2022, ISSN: 2072-6694 (Print) 2072-6694. DOI: 10.3390/cancers14010215.

[25] S. Chen *et al.*, "The value of mri in evaluating the efficacy and complications with the treatment of intra-arterial chemotherapy for retinoblastoma," *Oncotarget*, vol. 8, no. 24, pp. 38 413–38 425, 2017, ISSN: 1949-2553. DOI: 10.18632/oncotarget.16423.

[26] Y. J. Choi *et al.*, "Effects on periocular tissues after proton beam radiation therapy for intraocular tumors," *J Korean Med Sci*, vol. 33, no. 16, e120, 2018, ISSN: 1011-8934 (Print) 1011-8934. DOI: 10.3346/jkms.2018.33.e120.

[27] P. V. Foti *et al.*, "Diagnostic methods and therapeutic options of uveal melanoma with emphasis on mr imaging-part ii: Treatment indications and complications," *Insights Imaging*, vol. 12, no. 1, p. 67, 2021, ISSN: 1869-4101 (Print) 1869-4101. DOI: 10.1186/s13244-021-01001-w.

[28] E. M. Becerra, M. A. Saornil, G. Blanco, M. C. Méndez, Y. Muiños, and M. R. Esteban, "Cavitary choroidal melanoma," *Can J Ophthalmol*, vol. 40, no. 5, pp. 619–22, 2005, ISSN: 0008-4182 (Print) 0008-4182. DOI: 10.1016/s0008-4182(05)80057-2.

[29] J. Biswas, R. Raghavendra, V. Ratra, S. Krishnakumar, L. Gopal, and M. P. Shanmugam, "Diffuse malignant melanoma of the choroid simulating metastatic tumour in the choroid," *Indian J Ophthalmol*, vol. 48, no. 2, pp. 137–40, 2000, ISSN: 0301-4738 (Print) 0301-4738.

[30] G. M. Damento, K. K. Koeller, D. R. Salomão, and J. S. Pulido, "T2 fluid-attenuated inversion recovery imaging of uveal melanomas and other ocular pathology," *Ocul Oncol Pathol*, vol. 2, no. 4, pp. 251–261, 2016, ISSN: 2296-4681 (Print) 2296-4657. DOI: 10.1159/000447265.

[31] K. Erb-Eigner, G. Willerding, M. Taupitz, B. Hamm, and P. Asbach, "Diffusion-weighted imaging of ocular melanoma," *Invest Radiol*, vol. 48, no. 10, pp. 702–7, 2013, ISSN: 0020-9996. DOI: 10.1097/RLI.0b013e31828eea67.

[32] P. Hirunpat, N. Sanghan, and S. Hirunpat, "White matter: A good reference for the signal intensity evaluation in magnetic resonance imaging for the diagnosis of uveal melanoma," *Neuroradiol J*, vol. 34, no. 2, pp. 113–119, 2021, ISSN: 1971-4009 (Print) 1971-4009. DOI: 10.1177/1971400920973407.

[33] V. Houle, M. Bélair, and G. S. Allaire, "Airp best cases in radiologic-pathologic correlation: Choroidal melanoma," *Radiographics*, vol. 31, no. 5, pp. 1231–6, 2011, ISSN: 0271-5333. DOI: 10.1148/rg.315105211.

[34] M. G. Jaarsma-Coes, T. A. Ferreira, P. J. van Houdt, U. A. van der Heide, G. P. M. Luyten, and J. M. Beenakker, "Eye-specific quantitative dynamic contrast-enhanced mri analysis for patients with intraocular masses," *Magma*, 2021, ISSN: 0968-5243. DOI: 10.1007/s10334-021-00961-w.

[35] H. Jeong and H. S. Sa, "Uveal melanoma with massive extraocular extension through the sclerocorneal limbus," *Korean J Ophthalmol*, vol. 29, no. 4, pp. 280–1, 2015, ISSN: 1011-8942 (Print) 1011-8942. DOI: 10.3341/kjo.2015.29.4.280.

[36] A. Jiblawi, H. Chanbour, A. Tayba, H. Khayat, and K. Jiblawi, "Magnetic resonance imaging diagnosis of choroidal melanoma," *Cureus*, vol. 13, no. 7, e16628, 2021, ISSN: 2168-8184 (Print) 2168-8184. DOI: 10.7759/cureus.16628.

[37] M. Kamrava *et al.*, "Quantitative multiparametric mri in uveal melanoma: Increased tumor permeability may predict monosomy 3," *Neuroradiology*, vol. 57, no. 8, pp. 833–40, 2015, ISSN: 0028-3940. DOI: 10.1007/s00234-015-1546-0.

[38] V. Khetan, K. Gupta, E. R. Mohan, and L. Gopal, "Uveal melanoma presenting as cataract and staphyloma," *Indian J Ophthalmol*, vol. 57, no. 3, pp. 223–5, 2009, ISSN: 0301-4738 (Print) 0301-4738. DOI: 10.4103/0301-4738.49398.

[39] K. Koolstra, J. M. Beenakker, P. Koken, A. Webb, and P. Börnert, "Cartesian mr fingerprinting in the eye at 7t using compressed sensing and matrix completion-based reconstructions," *Magn Reson Med*, vol. 81, no. 4, pp. 2551–2565, 2019, ISSN: 0740-3194 (Print) 0740-3194. DOI: 10.1002/mrm.27594.

[40] A. J. Lemke *et al.*, "Intraocular metastases: Differential diagnosis from uveal melanomas with high-resolution mri using a surface coil," *Eur Radiol*, vol. 11, no. 12, pp. 2593–601, 2001, ISSN: 0938-7994 (Print) 0938-7994. DOI: 10.1007/s003300100936.

[41] C. K. Minija and M. P. Shanmugam, "Subretinal lipid exudation associated with untreated choroidal melanoma," *Indian J Ophthalmol*, vol. 59, no. 3, pp. 233–5, 2011, ISSN: 0301-4738 (Print) 0301-4738. DOI: 10.4103/0301-4738.81041.

[42] C. P. Nagesh, R. Rao, S. B. Hiremath, and S. G. Honavar, "Magnetic resonance imaging of the orbit, part 1: Basic principles and radiological approach," *Indian J Ophthalmol*, vol. 69, no. 10, pp. 2574–2584, 2021, ISSN: 0301-4738. DOI: 10.4103/ijo.IJO_3141_20.

[43] T. N. Nguyen, C. Edelstein, M. Mansour, and J. Burnier M. N., "Primary choroidal melanoma masquerading as a hemorrhagic lesion in a patient with ocular trauma," *Can J Ophthalmol*, vol. 38, no. 3, pp. 228–9, 2003, ISSN: 0008-4182 (Print) 0008-4182. DOI: 10.1016/s0008-4182(03)80066-2.

[44] G. Rebolleda, M. Suárez Figueroa, F. J. Muñoz-Negrete, and A. Rocamora, "Magnetic resonance imaging in cavitary choroidal melanoma," *Eur J Ophthalmol*, vol. 10, no. 4, pp. 335–7, 2000, ISSN: 1120-6721 (Print) 1120-6721. DOI: 10.1177/112067210001000412.

[45] P. Romero-Aroca, M. Montero-Jaime, B. Intriago, F. Riu, K. B. Peña-Gonzalez, and M. Almena-Garcia, "18fdg-pet/ct assessing the absence of cell viability and excluding metastatic disease in a case of necrotic choroidal melanoma," *Eur J Ophthalmol*, vol. 22, no. 2, pp. 288–92, 2012, ISSN: 1120-6721. DOI: 10.5301/ejo.5000016.

[46] A. R. Sepahdari, R. Kapur, V. K. Aakalu, J. P. Villablanca, and M. F. Mafee, "Diffusion-weighted imaging of malignant ocular masses: Initial results and directions for further study," *AJNR Am J Neuroradiol*, vol. 33, no. 2, pp. 314–9, 2012, ISSN: 0195-6108 (Print) 0195-6108. DOI: 10.3174/ajnr.A2747.

[47] C. Stroszczynski *et al.*, "Choroidal hemangioma: Mr findings and differentiation from uveal melanoma," *AJNR Am J Neuroradiol*, vol. 19, no. 8, pp. 1441–7, 1998, ISSN: 0195-6108 (Print) 0195-6108.

[48] Y. Su, X. Xu, W. Wei, and J. Xian, "Using a novel mr imaging sign to differentiate retinal pigment epithelium from uveal melanoma," *Neuroradiology*, vol. 62, no. 3, pp. 347–352, 2020, ISSN: 0028-3940. DOI: 10.1007/s00234-019-02353-3.

[49] W. Wei *et al.*, "Dynamic contrast-enhanced magnetic resonance imaging of ocular melanoma as a tool to predict metastatic potential," *J Comput Assist Tomogr*, vol. 41, no. 5, pp. 823–827, 2017, ISSN: 0363-8715. DOI: 10.1097/rct.0000000000000598. [Online]. Available: https://core.ac.uk/download/212341616.pdf.

[50] C. P. Nagesh, R. Rao, S. B. Hiremath, and S. G. Honavar, "Magnetic resonance imaging of the orbit, part 2: Characterization of orbital pathologies," *Indian J Ophthalmol*, vol. 69, no. 10, pp. 2585–2616, 2021, ISSN: 0301-4738. DOI: 10.4103/ijo.IJO_904_21.

[51] C. H. Damianidis *et al.*, "Magnetic resonance imaging and ultrasonographic evaluation of retinal detachment in orbital uveal melanomas," *Neuroradiol J*, vol. 23, no. 3, pp. 329–38, 2010, ISSN: 1971-4009 (Print) 1971-4009. DOI: 10.1177/197140091002300313.

[52] G. Blanco, "Diagnosis and treatment of orbital invasion in uveal melanoma," *Can J Ophthalmol*, vol. 39, no. 4, pp. 388–96, 2004, ISSN: 0008-4182 (Print) 0008-4182. DOI: 10.1016/s0008-4182(04)80010-3.

[53] A. Bradley, A. Estes, L. Ulrich, D. Thomas, and D. Gay, "Epibulbar plasmacytoma masquerading as subconjunctival hemorrhage in a patient with multiple myeloma," *Cornea*, vol. 36, no. 2, pp. 249–251, 2017, ISSN: 0277-3740. DOI: 10.1097/ico.0000000000001071.

[54] T. A. Ferreira, P. Saraiva, S. W. Genders, M. V. Buchem, G. P. M. Luyten, and J. W. Beenakker, "Ct and mr imaging of orbital inflammation," *Neuroradiology*, vol. 60, no. 12, pp. 1253–1266, 2018, ISSN: 0028-3940 (Print) 0028-3940. DOI: 10.1007/s00234-018-2103-4.

[55] S. Fusetti, R. Parrozzani, F. Urban, M. Gurabardhi, G. Ferronato, and E. Midena, "Modified enucleation for choroidal melanoma with large extrascleral extension," *Orbit*, vol. 29, no. 2, pp. 70–5, 2010, ISSN: 0167-6830. DOI: 10.3109/01676830903294883.

[56] N. Hosten *et al.*, "Uveal melanoma: Detection of extraocular growth with mr imaging and us," *Radiology*, vol. 202, no. 1, pp. 61–7, 1997, ISSN: 0033-8419 (Print) 0033-8419. DOI: 10.1148/radiology.202.1.8988193.

[57] F. A. Jacinto and C. E. Margo, "Neglected choroidal melanoma tracking along optic nerve to brain," *Ophthalmology*, vol. 123, no. 12, p. 2488, 2016, ISSN: 0161-6420. DOI: 10.1016/j.ophtha.2016.06.023.

[58] B. H. Jacobsen, C. Ricks, and R. P. Harrie, "Ocular ultrasound versus mri in the detection of extrascleral extension in a patient with choroidal melanoma," *BMC Ophthalmol*, vol. 18, no. 1, p. 320, 2018, ISSN: 1471-2415. DOI: 10.1186/s12886-018-0990-0.

[59] H. Kiratli, İ. Koç, and B. Tarlan, "Orbital extension of an unsuspected choroidal melanoma presumably through an aqueous tube shunt," *Ocul Oncol Pathol*, vol. 2, no. 3, pp. 144–7, 2016, ISSN: 2296-4681 (Print) 2296-4657. DOI: 10.1159/000441726.

[60] Y. Li, X. Yang, Y. Huang, Y. Hei, L. Wang, and L. Xiao, "Orbital extension of uveal melanoma: Treatment and survival analysis," *Int Ophthalmol Clin*, vol. 59, no. 2, pp. 37–51, 2019, ISSN: 0020-8167. DOI: 10.1097/iio.0000000000000270.

[61] A. Mahajan, A. Crum, M. H. Johnson, and M. A. Materin, "Ocular neoplastic disease," *Semin Ultrasound CT MR*, vol. 32, no. 1, pp. 28–37, 2011, ISSN: 0887-2171 (Print) 0887-2171. DOI: 10.1053/j.sult.2010.12.001.

[62] A. Maheshwari and P. T. Finger, "Cancers of the eye," *Cancer Metastasis Rev*, vol. 37, no. 4, pp. 677–690, 2018, ISSN: 0167-7659. DOI: 10.1007/s10555-018-9762-9.

[63] N. Mittica, G. K. Vemuganti, M. Duffy, E. Torczynski, and D. P. Edward, "Late orbital recurrence of a choroidal melanoma following internal resection: Report of a case and review of the literature," *Surv Ophthalmol*, vol. 48, no. 2, pp. 181–90, 2003, ISSN: 0039-6257 (Print) 0039-6257. DOI: 10.1016/s0039-6257(02)00458-7.

[64] M. Modarres, A. Rezanejad, and K. G. Falavarjani, "Recurrence and massive extraocular extension of choroidal malignant melanoma after vitrectomy and endoresection," *Indian J Ophthalmol*, vol. 62, no. 6, pp. 731–3, 2014, ISSN: 0301-4738 (Print) 0301-4738. DOI: 10.4103/0301-4738.136247.

[65] A. M. Rahman, D. Selva, and G. Davis, "Choroidal melanoma with extrascleral extension in an australian aboriginal man," *Clin Exp Ophthalmol*, vol. 35, no. 2, pp. 187–9, 2007, ISSN: 1442-6404 (Print) 1442-6404. DOI: 10.1111/j.1442-9071.2006.01438.x.

[66] Z. Récsán, K. Karlinger, M. Fodor, A. Zalatnai, M. Papp, and G. Salacz, "Mri for the evaluation of scleral invasion and extrascleral extension of uveal melanomas," *Clin Radiol*, vol. 57, no. 5, pp. 371–6, 2002, ISSN: 0009-9260 (Print) 0009-9260. DOI: 10.1053/crad.2001.0859.

[67] R. Sambuelli, J. D. Luna, V. E. Reviglio, A. Aoki, and C. P. Juarez, "Small choroidal melanoma with massive extraocular extension: Invasion through posterior scleral emissary channels," *Int Ophthalmol*, vol. 24, no. 4, pp. 213–8, 2001, ISSN: 0165-5701 (Print) 0165-5701. DOI: 10.1023/a:1022539129449.

[68] J. A. Shields, C. L. Shields, A. S. Kimmel, and J. Eagle R. C., "Contralateral blindness from chiasmal extension of unsuspected choroidal melanoma," *Ophthalmic Plast Reconstr Surg*, vol. 20, no. 5, pp. 384–7, 2004, ISSN: 0740-9303 (Print) 0740-9303. DOI: 10.1097/01.iop.0000139522.31074.2e.

[69] A. D. Singh *et al.*, "Optic nerve assessment using 7-tesla magnetic resonance imaging," *Ocul Oncol Pathol*, vol. 2, no. 3, pp. 178–80, 2016, ISSN: 2296-4681 (Print) 2296-4657. DOI: 10.1159/000443650.

[70] T. Tartaglione *et al.*, "Uveal melanoma: Evaluation of extrascleral extension using thin-section mr of the eye with surface coils," *Radiol Med*, vol. 119, no. 10, pp. 775–83, 2014, ISSN: 0033-8362. DOI: 10.1007/s11547-014-0388-x.

[71] J. M. Beenakker, J. Wezel, J. Groen, A. G. Webb, and P. Börnert, "Silent volumetric multi-contrast 7 tesla mri of ocular tumors using zero echo time imaging," *PLoS One*, vol. 14, no. 9, e0222573, 2019, ISSN: 1932-6203. DOI: 10.1371/journal.pone.0222573. [Online]. Available: https://www.ncbi.nlm.nih.gov/pmc/articles/PMC6746372/pdf/pone.0222573.pdf.

[72] Y. Su *et al.*, "Value of mr-based radiomics in differentiating uveal melanoma from other intraocular masses in adults," *Eur J Radiol*, vol. 131, p. 109 268, 2020, ISSN: 0720-048x. DOI: 10.1016/j.ejrad.2020.109268.

[73] U. Walter *et al.*, "Ultrahigh field magnetic resonance and colour doppler real-time fusion imaging of the orbit–a hybrid tool for assessment of choroidal melanoma," *Eur Radiol*, vol. 24, no. 5, pp. 1112–7, 2014, ISSN: 0938-7994. DOI: 10.1007/s00330-014-3101-5.

[74] Q.-G. Xu and J.-F. Xian, "Role of quantitative magnetic resonance imaging parameters in the evaluation of treatment response in malignant tumors," *Chinese medical journal*, vol. 128, no. 8, pp. 1128–1133, 2015, ISSN: 2542-5641 0366-6999. DOI: 10.4103/0366-6999.155127. [Online]. Available: https://pubmed.ncbi.nlm.nih.gov/25881611%20https://www.ncbi.nlm.nih.gov/pmc/articles/PMC4832957/.

2

Measuring eye deformation between planning and proton beam therapy position using magnetic resonance imaging

M.G. Jaarsma-Coes, M. Marinkovic, E. Astreinidou, M.S. Schuurmans, F.P. Peters, G.P.M. Luyten, C.R.N. Rasch, J.W.M. Beenakker

This chapter has been published in Physics and Imaging in Radiation Oncology **16**, 33-36 (2020)[1]

Proton beam therapy (PBT) for uveal melanoma (UM) is performed in sitting position, while the acquisition of the Magnetic resonance (MR)-images for treatment planning is performed in supine position. We assessed the effect of this difference in position on the eye- and tumour- shape. Seven subjects and six UM-patients were scanned in supine and a seating mimicking position. The distances between the tumour/sclera in both positions were calculated. The median distance between both positions was 0.1 mm. Change in gravity direction produced no substantial changes in sclera and tumour shape, indicating that supinely acquired MR-images can be used to plan ocular-PBT.

2.1 Introduction

Uveal melanoma (UM) is the most common primary intraocular tumour, occurring at a rate of approximately 14 cases per million person-years[2,3]. The management of localized UM can be divided into globe-preserving therapy and enucleation, i.e. surgical removal of the eye. The three most common globe-preserving therapies are plaque brachytherapy, stereotactic radiosurgery (SRS) and proton beam therapy (PBT). The optimal treatment modality depends on several factors including size and location of the tumour, proximity to the optic disc or fovea, and patients' preference[4–6].

For larger tumours as well as tumours in close proximity to the optic nerve, stereotactic radiosurgery (SRS) or PBT is generally used. The latter has a dose distribution superior to SRS, allowing sharper dose gradients and highly conformal dose to the tumour, sparing more healthy tissue. As a consequence, PBT potentially provides better clinical outcomes in terms of vision, radiation induced side-effects and eye retention[7–9].

PBT treatment planning is currently performed on a generic model of the eye and tumour, based on X-rays, fundus photographs and ocular ultrasound data[7,10] yielding only a rudimentary representation. Magnetic resonance imaging (MRI) however, can be used to construct detailed patient-specific models[11–13]. It is recognized that these models might provide a more accurate representation of the tumour and organs at risk. However, as MRI scans are performed with the patient in prone position and PBT is performed with the patients in "seated" position, the change in gravity direction might induce a geometric mismatch in tumour and/or eye shape between both postures. We therefore, assessed the effect of body pose on the eye- and tumour- shape.

2.2 Materials and methods

This study was carried out according to the Declaration of Helsinki for experiments involving humans and in accordance with the recommendations of the local Ethic Committee (CME LUMC, Leiden University Medical Centre).

2.2.1 Subject description

We assessed the effect of body pose on ocular shape in seven eyes of healthy subjects and its effect on tumour shape in six UM patients. Eye and tumour shape were compared between sitting up, as during PBT, (flexed) and scanning (supine) position. Additionally, two healthy subjects were scanned to assess the reproducibility of the method. The six included patients represent the wide variety of tumours that can occur in UM patients. The size of tumours ranged from small (height $\leq$ 3 mm) to large (height $>$ 8 mm) at time of scanning and differed in composition from mostly melanotic, partially melanotic to amelanotic lesions (table 2.1).

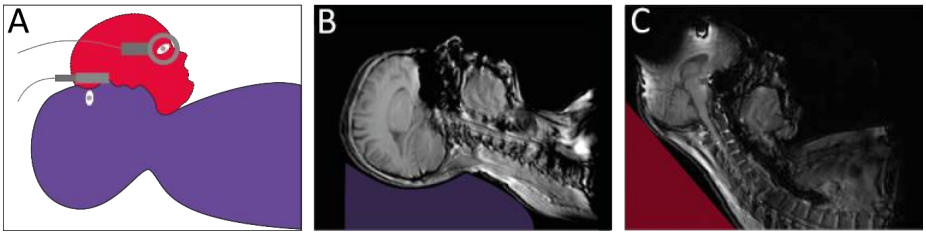

Figure 2.1: Patient and coil positioning in the scanner. (a) shows a schematic representation of the two positions in the MRI scanner with coil positions. The coil is positioned in front of the eye in supine position (purple) and to the sides in flexed position (red). (b) and (c) show a whole body, MR-images showing the subject in supine, (b), and flexed, (c), position in the MRI with a schematic representation of the head support.

Table 2.1: Tumour characteristics

	Base* (mm)	**Prominence* (mm)**	**AJCC classification#**	
Patient 1	14	7	T3a stage IIb	Melanotic
Patient 2	7	3	T1a stage I	Melanotic
Patient 3	18	12	T4b stage IIIB	Partially melanotic
Patient 4	12	13	T4b stage IIIB	Amelanotic
Patient 5	9	6	T2B stage IIb	Melanotic
Patient 6	15	4	T3a stage IIb	Partially melanotic

∗ Base and prominence (including sclera) measured on MRI. # AJCC classification at time of diagnosis.

When scanning patients we noticed a deterioration in image quality, especially for the scans acquired in flexed position. Therefore, an additional reproducibility measurement was performed by scanning a patient twice in flexed position and another patient twice in supine position to assess the effect of motion blurring on the determined shape difference.

2.2.2 MRI setup

All subjects were scanned in a wide bore 3T MRI (Ingenia, Philips Healthcare, Best, The Netherlands) with one or two 47 mm Rx-surface coils (Philips Healthcare) after giving written informed consent. These coils were mounted on to a flexible eye mask. The limited size of the magnet bore refrained from scanning subjects in sitting position, as during PBT. Therefore the subjects were scanned in a posture that mimics gravity in sitting posture.This was achieved by positioning the subjects on their backs with their chin on the chest. The head was supported to limit head motion during the scans (figure 2.1c).

For the scans in supine position, the coils were positioned in front of both eyes, which is the optimal location for ocular MRI[14,15]. For the flexed position, however, this configuration is not suitable, as the main direction of the magnetic flux of the surface coil would be parallel to main magnetic field, resulting in no MR-signal.

Table 2.2: Scanning protocol

	Healthy subjects	Patients	
Sequence	**T2 TSE**	**T1 TSE***	**T2 TSE***
TR (ms)	2500	350	2500
TE (ms)	285	9.4	293
Acquisition voxel (mm3)	0.9 isotropic	1.0 isotropic	0.8 isotropic
Field of view (mm)	80 x 102 x 40	80 x 80 x 40	50 x 81 x 40
Echo train length (n)	130	14	117
Averages (n)	2	2	2
Scan time (min)	3:13	3:23	3:35

∗ Patients were scanned in supine position and after contrast administration in flexed position.

Hence, the coils were positioned to the side of both eyes for imaging in flexed position. In healthy subjects two coils were used, one in front of each eye, in contrast to patients were only one Rx-surface coil, in front of the affected eye, was used in accordance with the current clinical protocol[16]. A schematic representation of the two positions in the MRI scanner with coil positions is shown in figure 2.1a.

Healthy subjects were scanned in a dedicated session for this study with a protocol consisting of a survey to plan the subsequent T_2-weighted scans (TR:2500 ms/TE:285 ms/Voxel size:$(0.9\ mm)^2$ Scan time:3:13 min) in both flexed and supine position. For the patients, additional scans were added at the end of the clinical protocol consisting of a survey with subsequent T_2-weighted scan (TR:2500 ms/TE:293 ms/Voxel size:$(0.8\ mm)^2$/Scan time:3:35 min) in flexed position (table 2.2).

2.2.3 Analysis

To compare the eye and tumour shape between both postures, the MR-images were registered and the anatomies segmented. First the sclera in supine position was segmented to obtain a mask for registration. Subsequently the flexed image was registered to the supine image. Finally, the sclera, lens and if appropriate tumour were segmented on both images.

Registration of the eyes was challenging as not only the complete head was in different positions between both scans, but the eyes can, additionally, rotate within the head. Hence, a masked registration, in which the anatomy outside the eye is discarded, was performed. Registration was performed using Elastix 4.9.0[17] in Mevislab 3.0.2 (MeVis Medical Solutions AG, Bremen, Germany)[18]. The eye mask used in the registration was created by segmenting the sclera in the supinely acquired scan. This segmentation was subsequently extended by 2.5 mm to include the optic nerve as an additional registration landmark. The MRIs in flexed position were registered to the supinely acquired scans using the obtained mask. If necessary, additional manual registration correction was performed in MeVisLab.

After registration, the sclera, lens and tumour were segmented using Subdivision Surfaces controlled by the maximal gradient magnitude[19]. This method is independent of signal amplitude which varied per MRI scan, especially because of the

different coil positions between supine and flexed acquisitions. When needed, manual corrections were made in the segmentation.

The difference in shape of the eye and tumour between both postures were afterwards determined by calculating the distance, i.e. for each mesh point of the supine position the closest mesh point in the flexed position, as a measure for the shape difference. For the eye-shape, points anterior from the lens were discarded as susceptibility artefacts often occur at the air-tissue interface of the cornea. The segmented mesh was subdivided into edges with a length less than 0.16 mm resulting in approximately 105 points for the healthy eyes and >104 points describing the tumour boundaries. Finally the concordance index[20] was calculated.

2.3 Results

All flexed images were successfully registered to the supine images in the seven healthy subjects and six patients, although most registrations needed additional manual (rigid) registration correction. A detailed description can be found the appendix. The average 95th percentile reproducibility in the two healthy volunteers and two patients was 0.3 mm.

In healthy subjects the median measured distances between the eye in supine and flexed position was 0.1 mm with a 95th percentile of 0.3 mm with a maximum of 0.4 mm. The concordance index for all eyes was 0.95 or higher and the volume change was less than 0.6%. A deformation map of all healthy eyes can be found in figure 2.2

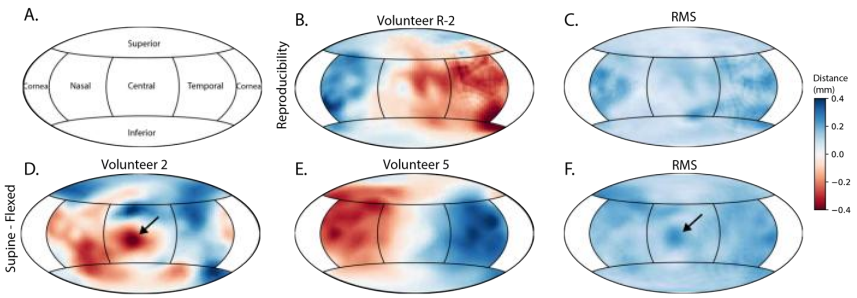

Figure 2.2: An Hammer projection of the measured distances for all eye segmentation's. Positive values indicate that the points on the supine segmentation is inside the flexed segmentation. (A) Legend to translate the position on the map to positions on the eye. (B) An representative example of a distance map of a healthy volunteer scanned in supine position twice. (C) The average distance (root means square) of all reproducibility measurements showing low values <0.3mm. (D) Example of healthy volunteer 2 scanned in supine and flexed position. An deformation of -0.4mm is visible at the location of the optic nerve (arrow). (E) Example of healthy volunteer 5 in both positions shows a more homogeneous shape change which is most likely due to an residual registration error. (F) The average distance (root means square) of all subjects scanned in supine and flexed position showing an homogeneous average distance of 0.1 mm, except around the optic nerve (arrow).

Table 2.3: Overview of the results for the healthy subjects, patients and controls.

	Volume (ml)			**Distance (mm)**		
Eyes	**Supine**	**Flexed**	**Difference (%)**	**Median**	**95th perc.**	**CI**
1	5.5	5.6	0.5	0.1	0.3	0.97
2	7.2	7.2	0.0	0.1	0.3	0.95
3	6.3	6.3	-0.1	0.1	0.2	0.97
4	6.0	5.9	-0.5	0.1	0.3	0.95
5	6.4	6.4	-0.2	0.1	0.3	0.95
6	6.1	6.1	-0.1	0.1	0.4	0.95
7	5.8	5.8	0.0	0.2	0.3	0.96
Tumours						
1	0.7	0.7	2.4	0.1	0.4	0.91
2*	n.a.	n.a.	n.a.	0.1	0.3	n.a.
3	1.2	1.2	-1.7	0.1	0.4	0.95
4	0.9	0.9	2.0	0.2	0.4	0.95
5	0.1	0.1	-11.2	0.1	0.3	0.87
6	0.1	0.1	3.7	0.1	0.3	0.85
Reproducibility						
Eye	Side	Front				
1	6.7	6.7	0.01	0.1	0.3	0.96
1 (2)	6.7		0.00	0.1	0.4	0.96
2	7.2	7.2	0.01	0.1	0.2	0.98
2 (2)	7.2		0.00	0.1	0.4	0.97
Tumours						
5 Supine - Supine	0.1	0.2	7.5	0.1	0.4	0.89
6 Flexed - Flexed	0.1	0.1	6.1	0.1	0.2	0.92

CI: Conformity index $*$ The base of the tumour was not segmented due to the small size therefore the volume and conformity index could not be calculated.

In tumours of the patients an average median distance between both postures of 0.1 mm was found with an 95th percentile of 0.3 mm with a maximum of 0.4 mm, figure 2.4. Although the distances were in generally very similar to the healthy subjects, some local regions showed distances $>$ 0.4 mm, for example in patient 3 (figure 2.3 b and c). These outlier regions were mostly caused by motion artefacts in one of the two scans. The concordance index of the tumours ranged from 0.85 to 0.95.

An overview of the results for all subjects can be found in table 2.3.

2.4 Discussion

MRI based PBT treatment planning systems rely on data obtained while the patient is in supine position whereas PBT is performed in seated position, raising the question whether the effect of gravity on the shape of the eye and tumour should be taken into account in these models. In this study we assessed the effect of body pose on ocular shape in seven healthy subjects and six UM patients using MRI. We showed that in healthy subjects the eye shape changes less than 0.4 mm which

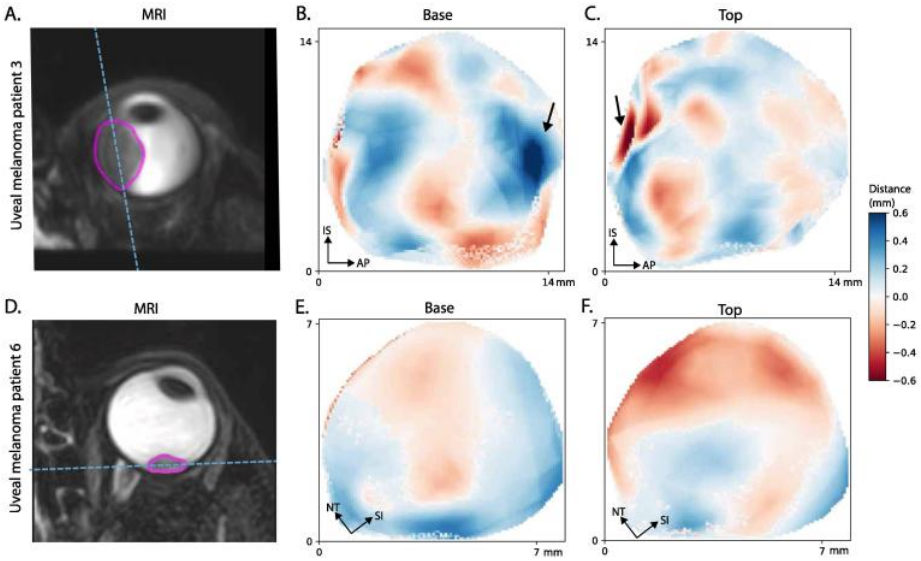

Figure 2.3: The measured distances of the tumours of patients 3 and 6. The two regions with outliers (arrow in (B) and (C)) are located near the tumour base and next to a retinal detachment or lens, making segmentation more challenging.

is close to the measured reproducibility of 0.3 mm and well within our measured isotropic voxel size of 0.9 mm. This indicates that the eyes retains its shape even when gravity works in a different direction. Similarly, the median shape change for the tumours was 0.1 mm with a maximum 95^{th} percentile of 0.4 mm which was in line with the reproducibility of 0.3 mm and well within voxel limit.

Slopsema et al.[21] showed that the shape change of the eye due to gravity is less than 0.6 ± 0.3 mm, by comparing the tantalum clip positions on supinely acquired CT images, with clip positions obtained from a geometrical eye-model based on orthogonal X-rays acquired in sitting position. As this observed difference is probably largely the result of uncertainties in the geometrical eye-model used for PT planning, such as the rotational center of the eye, the actual change in eye shape is expected to be less than the observed differences between the CT-based and X-ray based eye-model. These results are therefore in line with this study as we show that the potential shape change of the eye due to gravity is <0.4 mm.

When comparing the distance measurements of the eyes and tumours in different positions we observed some local outliers (>0.4 mm) in the tumour distance measurements. This is likely caused by the fact that tumour segmentation is more challenging than eye segmentation. For the eye segmentation the vitreous-sclera boundary has a high contrast whereas for tumour segmentation the tumour is not only located next to the vitreous but also often in close proximity of the lens or retinal detachment. These structures have a much lower contrast with the tumour. Furthermore, more motion artefacts were present in the scans of the patients as we

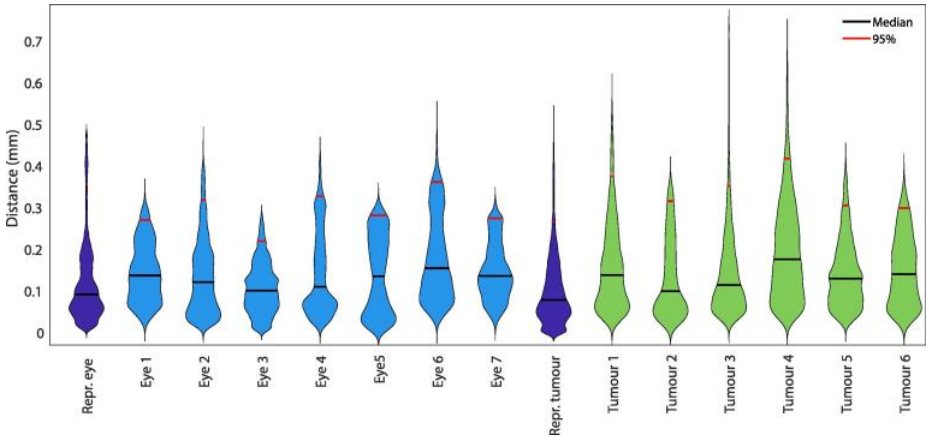

Figure 2.4: Violin plots showing the distribution of the measured distances between supine and flexed position.

scanned them in the flexed position at the end of a longer protocol. These outliers likely explain the lower concordances indexes (0.85–0.95 vs >0.95) we measured. Furthermore, the lower concordance indexes were observed in the smallest lesions, suggesting that the tumour size might be the biggest contributing factor as a small absolute change has a large effect on the concordances index of small lesions. The small distance measurements between both postures, which were less than 0.3 mm, are therefore a good confirmation that the change in tumour shape was very small.

These are important result as MRI is more and more used for diagnosis and follow up of uveal melanoma patients and more and more PT treatment centres and companies are working on improvement of treatment planning systems for uveal melanoma based on MRI, or CT which are also acquired in supine position[11,22]. The maximum eye and tumour deformation measured was lower than 0.6 mm, the interobserver variability of ultrasound in the evaluation of uveal melanoma thickness as determined in a comprehensive study by Char et al.[23]. It was also in the same order as eye movement during PT treatment (average of 0.4–0.9 mm)[24]. Furthermore, any potential effect of gravity on the shape of the eye was well within the safety margin of 2–3 mm currently used for PT planning of UM[25,26].

One of the limitations of our study was the small number of patients included in this study, which was primarily limited due to the burden of additional scanning in flexed position. Nonetheless, all different shapes (dome, mushroom), sizes (small, medium, large) and compositions (melanotic, partially melanotic and amelanotic) tumours were represented in the study population. As in none of these patients a significant tumour deformation was detected, we are confident that these findings are valid for the general population of UM patients. Furthermore, our measurement of deformation was limited by the voxel size of the 3D MRI acquisition. However, using interpolation and information of neighbouring voxels, we were able to estimate the edge location with subvoxel accuracy, as was confirmed by the reproducibility

of 0.3 mm.

In conclusion, changes in gravity direction produce no substantial changes in sclera and tumour shape. Our results indicate that supinely acquired MR images can be used to accurately plan ocular PT, which is performed in sitting position.

2.5 Acknowledgements

The authors thank Kilany Hassan and Berend Stoel (LKEB, LUMC) fort their help with image registration.

2.6 Appendix

2.6.1 Analysis

Manual editing of the registration was sometimes necessary as the mask removes all information outside of the eye, which leaves only two major locations of reference for registration for healthy subjects, the lens and the optic nerve, the rest of the eye is approximately rotationally invariant. In tumour patients additional information, the tumour, was available for registration. In half of the cases the registration was manually adjusted. In almost all of these cases motion artefacts were present in one or both scans. The automatic segmentation needed manual correction in 7/19 cases. Segmentations were generally performed on T2, in one tumour patient only a T1 scan was available. Although no severe motion artefacts were observed that impaired the analysis, a significant number of scans contained motion artefacts. These artefacts were more pronounced in patients (71% minor and 14% moderate) than in healthy subjects (30% minor). Motion artefacts mostly occurred in scans in flexed position, which is likely caused by three contributing factors. Firstly, this position is less comfortable and has less support compared to the supine position. Secondly, scans in flexed position suffer from B0 field inhomogeneities as the head is positioned higher in the magnet bore. Finally, patients were scanned in flexed position at the end of the 35-minute clinical scanning session in contrast to the healthy subjects who were scanned in flexed position first and this protocol took in total less than 15 minutes. We generally observe an increase in motion artefacts after half an hour of scanning due to fatigue and discomfort.

2.7 References

[1] M. G. Jaarsma-Coes *et al.*, "Measuring eye deformation between planning and proton beam therapy position using magnetic resonance imaging," eng, *Physics and imaging in radiation oncology*, vol. 16, pp. 33–36, Oct. 2020, ISSN: 2405-6316. DOI: 10.1016/j.phro.2020.09.010. [Online]. Available: https://pubmed.ncbi.nlm.nih.gov/33458341%20https://www.ncbi.nlm.nih.gov/pmc/articles/PMC7807689/.

[2] IKNL, *NKR cijfers*. [Online]. Available: https://iknl.nl/nkr-cijfers.

[3] A. D. Singh, M. E. Turell, and A. K. Topham, "Uveal melanoma: Trends in incidence, treatment, and survival," *Ophthalmology*, vol. 118, no. 9, pp. 1881–1885, 2011, ISSN: 01616420. DOI: 10.1016/j.ophtha.2011.01.040.

[4] B. A. Krantz, N. Dave, K. M. Komatsubara, B. P. Marr, and R. D. Carvajal, "Uveal melanoma: epidemiology, etiology, and treatment of primary disease.," *Clinical ophthalmology (Auckland, N.Z.)*, vol. 11, p. 279, 2017, ISSN: 1177-5467. DOI: 10.2147/OPTH.S89591.

[5] E. S. Blum, J. Yang, K. M. Komatsubara, and R. D. Carvajal, "Clinical Management of Uveal and Conjunctival Melanoma," *Oncology (Williston Park, N.Y.)*, vol. 30.1, pp. 29–43, 2016, ISSN: 08909091.

Table 2.4: Overview of the results for the healthy subjects, patients and controls

	Motion		**Registration**	**Segmentation**	**Scan**
	Supine	**Flexed**			
Eyes					
1	No	No	automatic	automatic	T2
2	Minimal	Minimal	edited	automatic	T2
3	Minimal	Minimal	edited	automatic	T2
4	Minimal	No	automatic	automatic	T2
5	No	No	edited	automatic	T2
6	No	No	automatic	automatic	T2
7	No	No	automatic	automatic	T2
Tumour					
1	Minimal	Moderate	edited	edited	T1
2	No	Minimal	edited	automatic*	T2
3	Minimal	Minimal	edited	edited	T2
4	No	Moderate	edited	edited	T2
5	Minimal	Minimal	edited	edited	
6	Minimal	Minimal	automatic	edited	T2
Reproducibility					
Eye					
1	No	No	automatic	automatic	T2
1 (2)	No		automatic	automatic	T2
2	No	No	automatic	automatic	T2
2 (2)	No		automatic	automatic	T2
Tumours					
5 supine – supine	Minimal	Minimal	edited	edited	T2
6 flexed - flexed	Minimal	Minimal	Automatic	edited	T2

* the tumour was segmented automatically but the additional sclera was removed manually.

[6] A. E. Koopmans, A. de Klein, N. C. Naus, and E. Kilic, "Diagnosis and Management of Uveal Melanoma," *European Ophthalmic Review*, 2013, ISSN: 1756-1795. DOI: 10.17925/eor.2013.07.01.56.

[7] M. J. Sikuade, S. Salvi, P. A. Rundle, D. G. Errington, A. Kacperek, and I. G. Rennie, "Outcomes of treatment with stereotactic radiosurgery or proton beam therapy for choroidal melanoma.," *Eye (London, England)*, vol. 29, no. 9, pp. 1194–1198, 2015, ISSN: 1476-5454 (Electronic). DOI: 10.1038/eye.2015.109. [Online]. Available: http://dx.doi.org/10.1038/eye.2015.109.

[8] E. Egger *et al.*, "Eye retention after proton beam radiotherapy for uveal melanoma," *International Journal of Radiation Oncology Biology Physics*, vol. 55, no. 4, pp. 867–880, 2003, ISSN: 03603016. DOI: 10.1016/S0360-3016(02)04200-1.

[9] V. Verma and M. P. Mehta, "Clinical Outcomes of Proton Radiotherapy for Uveal Melanoma," *Clinical Oncology*, vol. 28, no. 8, e17–e27, 2016, ISSN: 14332981. DOI: 10.1016/j.clon.2016.01.034.

[10] S. Aziz, A. Taylor, A. McConnachie, A. Kacperek, and E. Kemp, "Proton beam radiotherapy in the management of uveal melanoma: Clinical experience in Scotland," *Clin Ophthalmol*, vol. 3, pp. 49–55, 2009. [Online]. Available: http://www.ncbi.nlm.nih.gov/pubmed/19668544.

[11] H. G. Nguyen *et al.*, "Personalized Anatomic Eye Model From T1-Weighted Volume Interpolated Gradient Echo Magnetic Resonance Imaging of Patients With Uveal Melanoma," *International Journal of Radiation Oncology Biology Physics*, vol. 102, no. 4, pp. 813–820, 2018, ISSN: 1879355X. DOI: 10.1016/j.ijrobp.2018.05.004.

[12] E. Fleury *et al.*, "3D MRI-based treatment planning approach for non-invasive ocular proton therapy," *Medical Physics*, 2020, ISSN: 0094-2405.

[13] J. W. M. Beenakker *et al.*, "Automated analysis of eye tumor MR-images for an improved treatment determination," *Acta Ophthalmologica*, vol. 96, no. S261, pp. 11–12, Dec. 2018, ISSN: 1755-375X. DOI: 10.1111/aos.13972_34. [Online]. Available: https://onlinelibrary.wiley.com/doi/abs/10.1111/aos.13972_34.

[14] J. W. M. Beenakker *et al.*, "Clinical evaluation of ultra-high-field MRI for three-dimensional visualisation of tumour size in uveal melanoma patients, with direct relevance to treatment planning," *Magnetic Resonance Materials in Physics, Biology and Medicine*, vol. 29, no. 3, pp. 571–577, 2016, ISSN: 13528661. DOI: 10.1007/s10334-016-0529-4.

[15] P. de Graaf *et al.*, "Guidelines for imaging retinoblastoma: Imaging principles and mri standardization," *Pediatric radiology*, vol. 42, no. 1, pp. 2–14, 2012.

[16] T. A. Ferreira, L. G. Fonk, M. G. Jaarsma-Coes, G. G. van Haren, M. Marinkovic, and J. W. M. Beenakker, "MRI of uveal melanoma," *Cancers*, vol. 11, no. 3, pp. 1–20, 2019, ISSN: 20726694. DOI: 10.3390/cancers11030377.

[17] S. Klein, M. Staring, K. Murphy, M. A. Viergever, and J. P. Pluim, "Elastix: A toolbox for intensity-based medical image registration," *IEEE Transactions on Medical Imaging*, vol. 29, no. 1, pp. 196–205, 2010, ISSN: 02780062. DOI: 10.1109/TMI.2009.2035616.

[18] F. Ritter *et al.*, "Medical Image Analysis: A Visual Approach," *IEEE Pulse*, vol. 2, no. 6, pp. 60–70, 2011, ISSN: 2154-2287. DOI: 10.1109/MPUL.2011.942929. [Online]. Available: http://ieeexplore.ieee.org/xpls/abs_all.jsp?arnumber=6088923&tag=1.

[19] P. H. Kitslaar, R. van't Klooster, M. Staring, B. P. F. Lelieveldt, and R. J. van der Geest, "Segmentation of branching vascular structures using adaptive subdivision surface fitting," in *Medical Imaging 2015: Image Processing*, vol. 9413, International Society for Optics and Photonics, 2015, 94133Z, ISBN: 9781628415032. DOI: 10.1117/12.2082222.

[20] G. G. Hanna, A. R. Hounsell, and J. M. O'Sullivan, "Geometrical Analysis of Radiotherapy Target Volume Delineation: A Systematic Review of Reported Comparison Methods," *Clinical Oncology*, vol. 22.7, pp. 515–525, 2010, ISSN: 09366555. DOI: 10.1016/j.clon.2010.05.006.

[21] R. L. Slopsema *et al.*, "Can CT imaging improve targeting accuracy in clip-based proton therapy of ocular melanoma?" *Physics in Medicine and Biology*, vol. 64(3), p. 035 010, 2019, ISSN: 13616560. DOI: 10.1088/1361-6560/aaf9c9.

[22] J. Hrbacek *et al.*, "Practice Patterns Analysis of Ocular Proton Therapy Centers: The International OPTIC Survey," *International Journal of Radiation Oncology Biology Physics*, vol. 95, no. 1, pp. 336–343, 2016, ISSN: 1879355X. DOI: 10.1016/j.ijrobp.2016.01.040.

[23] D. H. Char, S. Kroll, R. D. Stone, R. Harrie, and B. Kerman, "Ultrasonographic measurement of uveal melanoma thickness: Interobserver variability," *British Journal of Ophthalmology*, vol. 74.3, pp. 183–185, 1990, ISSN: 00071161. DOI: 10.1136/bjo.74.3.183.

[24] D. Shin, S. H. Yoo, S. H. Moon, M. Yoon, S. B. Lee, and S. Y. Park, "Eye tracking and gating system for proton therapy of orbital tumors," *Medical Physics*, vol. 39.7Part1: pp. 4265–4273, 2012, ISSN: 00942405. DOI: 10.1118/1.4729708.

[25] R. Dendale *et al.*, "Proton beam radiotherapy for uveal melanoma: Results of Curie Institut-Orsay Proton Therapy Center (ICPO)," *International Journal of Radiation Oncology Biology Physics*, vol. 65.3, pp. 780–787, 2006, ISSN: 03603016. DOI: 10.1016/j.ijrobp.2006.01.020.

[26] B. Damato, A. Kacperek, M. Chopra, I. R. Campbell, and R. D. Errington, "Proton beam radiotherapy of choroidal melanoma: The Liverpool-Clatterbridge experience," *International Journal of Radiation Oncology Biology Physics*, vol. 62.5, pp. 1405–1411, 2005, ISSN: 03603016. DOI: 10.1016/j.ijrobp.2005.01.016.

3

Inter-Observer variability in MR-based target volume delineation of uveal melanoma

M.G. Jaarsma-Coes, L. Klaassen, B.M. Verbist, T.H.K. Vu, Y.L.B. Klaver, M.F. Rodrigues, C. Nabarro, G.P.M. Luyten, C.R.N. Rasch, M. van Herk, J.W.M. Beenakker

This chapter has been submitted to Advances in radiation oncology

Several efforts are being undertaken towards MRI-based treatment planning for ocular proton therapy for uveal melanoma (UM). The inter-observer variability of the gross target volume (GTV) on MRI is one of the important parameters to design safety margins for a reliable treatment. Therefore, this study assessed the inter-observer variation in GTV delineation of UM on MRI. Six observers delineated the GTV in ten different patients using the Big Brother contouring software. Patients were scanned at 3T MRI with a surface coil and tumours were delineated separately on contrast enhanced 3DT1 (T1gd) and 3DT2-weighted scans with an isotropic acquisition resolution of 0.8mm. Volume difference and overall local variation (median standard deviation of the distance between the delineated contours and the median contour) were analysed for each GTV. Additionally the local variation was analysed for four interfaces: sclera, vitreous, retinal detachment, and tumour-choroid interface. The average GTV was significantly larger on T1gd (0.57cm^3) compared to T2 (0.51cm^3, p=0.01). A not significant higher interobserver variation was found on T1gd (0.41mm) compared to T2 (0.35mm). The largest variations were found at the tumour-choroid interface, due to peritumoral enhancement. As a result, a larger part of this tumour-choroid interface appeared to be included on T1gd based GTVs compared to T2, explaining the smaller volumes on T2. In conclusion, the interobserver variation of 0.4mm on MRI are low with respect to the voxel size of 0.8mm. We recommend to delineate based on the T1gd-weighted scans, as choroidal tumour extensions might be missed.

3.1 Introduction

Uveal melanoma (UM) arises from melanocytes and is the most common primary intraocular tumour, occurring at a rate of approximately 14 cases per million person-years[1,2] With the increased availability of proton beam therapy (PT), the number of patients treated with ocular-PT are rising[3].

Currently, gross target volume (GTV) definition in proton therapy planning for uveal melanoma is based on a generic model of the eye and tumour, constructed using marker positions and 2D imaging such as fundus photographs and ocular ultrasound[4,5]. Although MR-imaging is increasingly being used in the ocular oncology[6,7], 3D imaging based GTV definition is currently not commonly used in ocular radiotherapy, conversely to other organs, where CT and MRI are commonly fused for target and organs at risk (OAR) delineation[8,9].

MRI-based tumour and organs at risk definition could be valuable for ocular-PT as its excellent soft tissue contrast and a 3D representation of the tumour and OAR[6,7,10] could help reduce the target volume and field size, potentially reducing toxicities[11]. Therefore, several efforts are being undertaken to enable a fully MRI-based treatment planning for ocular-PT as it would allow for a more patient-specific geometrical description of the tumour and OAR, than the currently used model-based approach[11–17].

As delineation variability is an important source of uncertainty in radiotherapy, it contributes to a significant portion of the treatment margins[18,19] For ocular MRI, however, this variation is currently unknown and due to the eye's small size and eye-specific imaging challenges, such as eye-blink artefacts[20,21], results from other anatomies cannot be translated to the eyes. Therefore the aim of this study is to assess the interobserver variation on GTV delineation of UM on MRI.

3.2 Materials and methods

To determine the interobserver variability on T2 and contrast enhanced T1 (T1gd) MR-images, six observers delineated the GTV in ten different UM patients. These patients were retrospectively selected to represent the wide spectrum of UM, in terms of lesion size, location and presence of retinal detachment. Three patients were scanned as part of a prospective study, which has been approved by the local ethics committee (METC-LDD, P16.186) and subjects were scanned after written informed consent. Seven patients received an MRI as part of clinical care, and their data was included retrospectively with approval of the local ethics committee.

3.2.1 Image acquisition and registration

All patients were scanned on a 3T MR scanner (Ingenia, Philips Healthcare, the Netherlands) using a 47 mm diameter surface coil as described by Ferreira et al[10]. In this study the 3D T2- and 3D T1- weighted scan before (T1 and T2) and a

3D T1 weighted scan after contrast administration (T1gd, 0.1 mmol/kg gadoterate megliumine, DOTAREM, Guebert, Roissy CdG Cedex, France) were used for delineation. Both T1 and T1gd scans were acquired in 2 minutes with a TE of 26 ms and TR of 400 ms. The T2 scan was acquired in 3 minutes with a TE of 305 ms and a TR of 2500 ms. Both T2 and T1gd were acquired with SPIR fat suppression. All scans were acquired with a 0.8 mm isotropic resolution and reconstructed on the MRI scanner with a resolution of 0.4 mm x 0.4 mm x 0.4 mm for T1 and 0.3 mm x 0.3 mm x 0.4 mm for T2 using zero filling.

Masked registration with Elastix 4.9.0[22] in Mevislab 3.0.2 (MeVis Medical Solutions AG, Bremen, Germany)[23] was used to register the T1 and T2 to the T1gd images. Before registration all scans were resampled using nearest neighbour interpolation to a resolution of 0.3 mm isotropic. A mask, created by segmenting the sclera on the T1gd, was used to restrict the registration region of interest to the globe.

3.2.2 Delineation of GTV

After a pilot study with four patients to get acquainted with the software and test the delineation guidelines, two radiation oncologists, two head and neck radiologists, and two ophthalmologist delineated the GTV of ten patients on T1gd and T2 after instruction on the use of the program and delineation guidelines. For contouring the Big Brother[24] training contouring software, developed at The Netherlands Cancer Institute and University of Manchester, was used. The GTV was delineated independently on the T2 and T1gd images. The other sequences (T1 and T1gd or T2) were visible in a side window as a reference to differentiate haemorrhage and tumour.

A combined evaluation of all three sequences is needed to differentiate UM from adjacent tissues. UM are hyperintense on T1 and hypointense on T2 compared to the vitreous and can be either hyperintense, isointense and hypointense compared to the choroid on T1 depending on the amount of pigmentation. Retinal detachment is hyperintense on T1 and hypo or isointense compared to the vitreous on T2, and can be distinguished from tumour due to lack of enhancement.[25] Therefore, areas with a hypointense signal compared to the vitreous on T2 and enhancing on T1gd were compatible with tumour (figure 3.1, dagger) and included in the GTV. Non enhancing regions were considered retinal detachment (RD, figure 3.1, double dagger) and not included in the GTV. The sclera, a hypointense structure adjacent to the vitreous and tumour was not included in the GTV.

3.2.3 Data analysis

To assess the delineation variation between observers, for each GTV its distances were calculated with respect to a median surface, which defined as the surface encompassing the voxels designated by at least 50% of the observers as part of the GTV (figure 3.2A). For each point of this median surface, the perpendicular distance was measured to the GTV of each observer and the standard deviation of these distances (local SD, figure 3.2B), was used as a measure of local observer

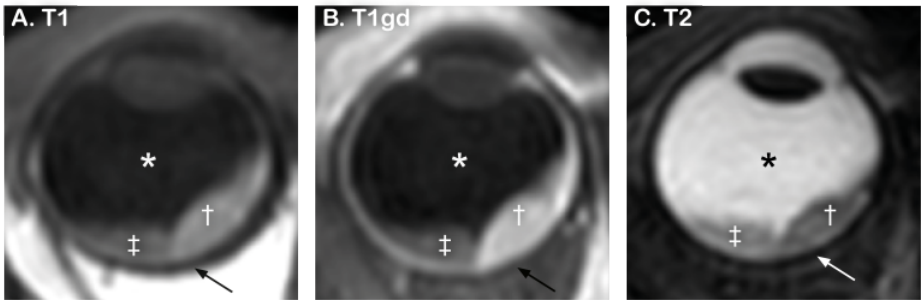

Figure 3.1: **Delineation instructions** Areas inside the sclera (arrow) with a hypointense signal compared to the vitreous (asterisk) on T2 (C) and enhancing on T1gd (B) compared to the T1w (A) were compatible with tumour and were included in the GTV (dagger). Areas with a hypointense signal compared to the vitreous on T2 but not enhancing on T1gd were considered retinal detachment and not included in the GTV (double dagger).

variation[24]. This local SD quantifies the spatial variation between contours, e.g. a larger local SD corresponds to a larger variation.

On each median contour, points adjacent to the sclera, vitreous, the tumour-choroid interface (edge), and/or retinal detachment were labelled. Areas which were adjacent to for example the lens or close to two regions remained unclassified (figure 3.2C).

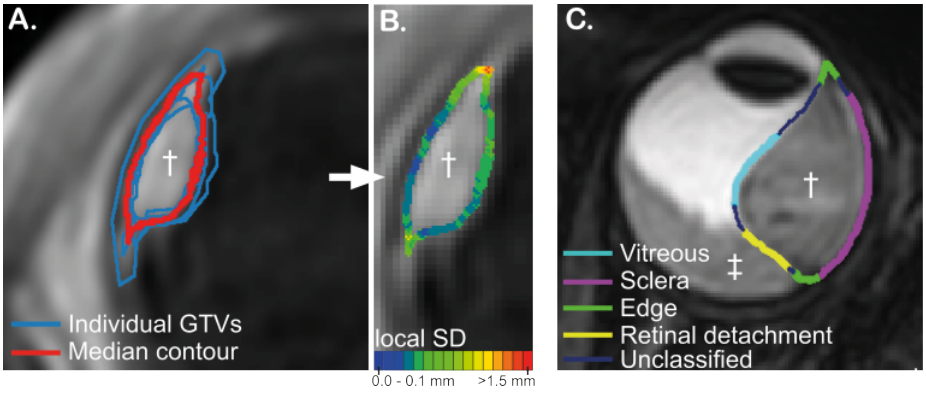

Figure 3.2: **Data analysis** For each patient, the median contour (A, red) of the delineated GTVs represents a 50% coverage of all GTVs of the individual observers (blue). For each point on this surface the local SD (variation in perpendicular distance to each individual delineation (B)) was determined. These distances were compared between patients to determine the inter-observer variability and were also analysed for different interfaces (C). Four interfaces were analysed: tumour/vitreous, tumour/sclera, tumour-choroid interface, tumour/retinal detachment. Retinal detachment (double dagger) can be isointense as the UM, however, it does not enhance as can be seen in figure 3.4Q.

Table 3.1: **Tumour characteristics**

Pt	LBD (mm)	Prominence (mm)	Treatment	SI on T1	SI on T2	RD	Remarks
1	11.7	8.0	PT	Hyperintense	Intermediate	No	
2	16.5	7.8	PT	Moderate hyperintense	Moderate hyperintense	Yes	Ciliary body involvement
3	12.4	7.3	PT	Hyperintense	Hypointense	No	Juxtapupillar
4	14.8	9.1	PT	Hyperintense	Hypointense	Yes	Ciliary body involvement
5	14.8	8.5	PT	Hyperintense	Hypointense	Yes	
6	12.4	5.5	Brachytherapy	Hyperintense	Hypointense	No	Ciliary body Involvement
7	15.0	5.1	Brachytherapy	Hyperintense	Hypointense	Yes	Juxtapupillar
8	15.6	5.9	Brachytherapy	Hyperintense	Hypointense	No	
9	18.0	13.0	Enucleation	Hyperintense	Intermediate	Yes	Ciliary body involvement
10	17.0	5.3, second lobe 3.3	Brachytherapy	Hyper- and hypointense	Hypointense	Yes*	Bilobar

Prominence and largest basal diameter (LBD) as measured on ultrasound. Signal intensity (SI) as described by the radiologist. Retinal detachment (RD) as described by the radiologist. *The RD was only adjacent to the GTV at the most inferior edge (out of plane) and therefore not included in the region analysis.

3.2.4 Statistics

The distance distributions per patient and per segment were not normally distributed, therefore the median and 75th percentile were reported. A paired-t test was performed to compare the average tumour volume and the median and 75th percentile observer variations per patient between delineations based on T1gd and T2 images. A t-test was used to compare the median observer variation between the different regions. Statistics were performed in Python version 3.6.6 using SciPy version 1.5.4.

3.3 Results

3.3.1 Patient characteristics

Five patients underwent proton beam therapy, four ruthenium brachytherapy and in one patient the affected eye was enucleated. The average tumour prominence on ultrasound was 7.6 mm (range: 5.1 – 13.0 mm) and the average largest basal diameter was 14.8 mm (range: 11.7 – 18.0 mm). In six patients retinal detachment was described by the radiologist during the pretreatment evaluation of the MR-images. Six tumours were hyperintense on T1-weighted images, two isointense and one hypointense compared to the choroid whereas one bipartite tumour consisted of both a hyper- and hypointense part. Eight tumours were hypointense compared to the eye-muscles on T2[25] whereas two were isointense. Two tumours were located juxtapupillary and in four patients the tumour involved the ciliary body. None of the patients had extrascleral extension. The tumour characteristics are described in table 3.1.

3.3.2 Volumetric analysis

A large variation in average tumour volume was observed between patients ranging from 0.16 to 1.79 cm^3 on both T1gd and T2 which was expected based on the different sizes of the lesions. The average delineated tumour volume was significantly

higher on T1gd (0.57 cm^3) compared to T2 (0.51 cm^3, p = 0.01, figure 3.3A). Generally, tumours were delineated larger on T1gd compared to T2, except for patient eight where the T2 volume was larger than the T1gd volume. Especially the posterior part of this tumour appeared to be delineated larger on T2 compared to T1gd. A visual inspection of all acquired images, especially the multi-slice images (not used for delineation), showed that this difference in tumour volume is likely caused by a small retinal detachment (figure 3.3C, arrow) incorrectly included in the GTV on T2 weighted images.

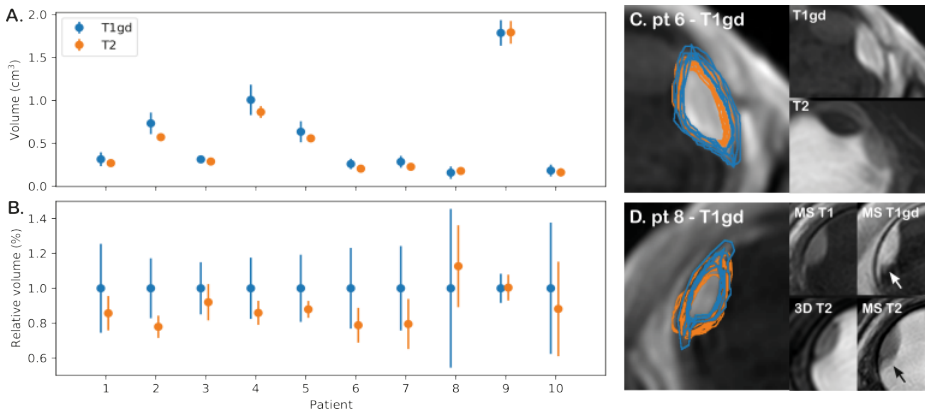

Figure 3.3: **GTV** (A) The average and standard deviation of the GTV for both T1gd (blue) and T2 (orange) based delineations. The delineated GTV was significantly larger on T1gd compared to T2 ($p < 0.01$). (B) The relative volume (mean $\pm$ std) with respect to the median volume on T1gd, shows that for the majority of the patients the tumour was delineated larger on T1gd than on T2. (C) In most patients the GTV based on T1gd (blue) is larger compared to T2 (orange). This difference seems to originate from the tumour-choroid interface. On the left all individual delineations. Upper insert, T1gd scan without delineations. Lower insert, T2. (D) Patient 8 is the only patient where a larger tumour volume was delineated on T2 compared to T1gd. Comparison with multi-slice images, which have a higher in-plane resolution than the 3D images used for contouring, show a small, non-enhancing, retinal detachment (arrow). This retinal detachment appears to be included in the T2 based GTV, explaining the larger volume.

3.3.3 Distance analysis

Combining all local SDs showed a slightly higher median SD on T1gd (0.41 mm) compared to T2 (0.35 mm), and a similar relation was observed for the 75^{th} percentile (T1gd: 0.60mm vs T2: 0.54mm). Pairwise comparison per patient showed no significant difference between median local SD and 75^{th} percentile (p=0.12 and p=0.15). Overall, observers had similar distances from the median contour, except for one of the radiologists who consistently had a lower distance from the median contour compared to the other observers (p=0.004, supplementary table 1).

Visual inspection of the local SDs for all individual patients, figure 4, showed mostly gradual changes in the local SD although hotspots with a higher observer variation were detected at the tumour-choroid interface (figure 3.4, open arrows) and in proximity of retinal detachment (figure 3.4, broad arrow).

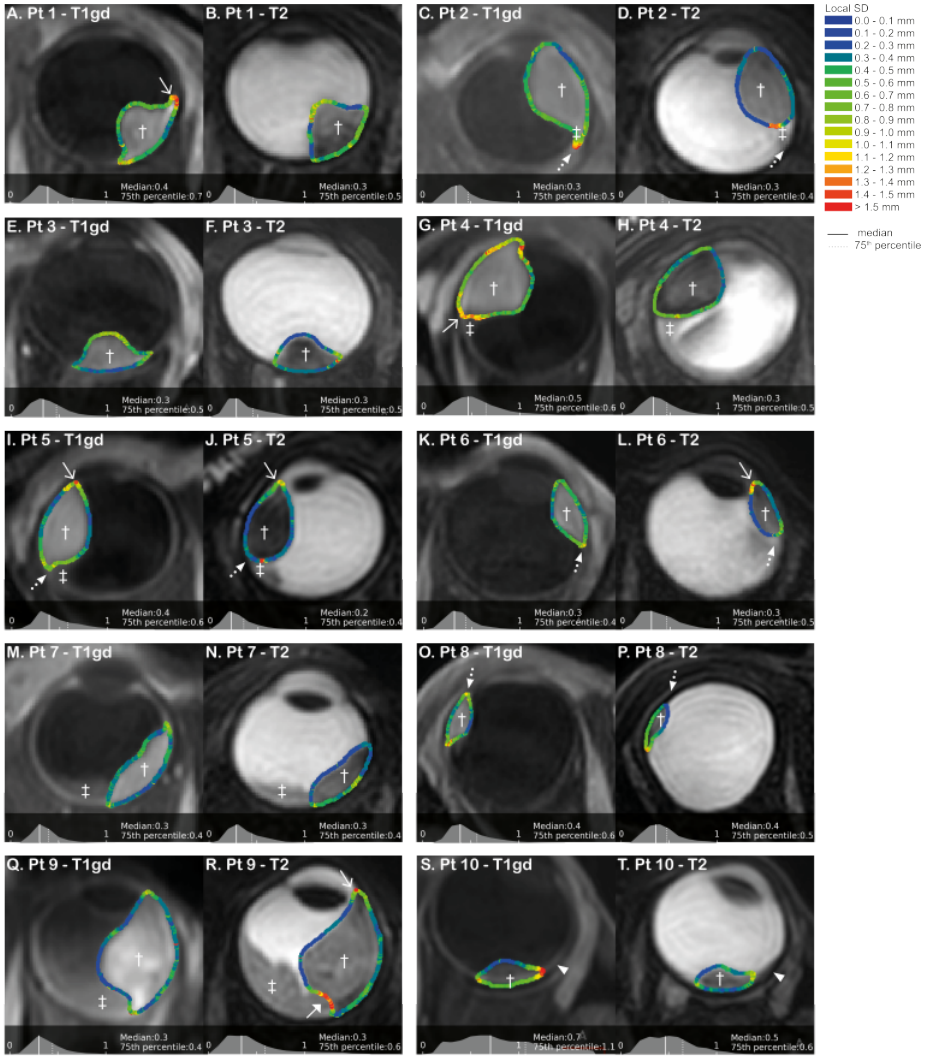

Figure 3.4: **Local SD of all patients** Representative slice showing the local SD per patient on T1gd and T2 with histogram of all local SDs at the bottom of the image (x-axis is between 0 and 2 mm). Generally the highest local SDs were located at the edge of the tumour base (open arrows; A, G, I, J, L, R) and at the tumour-retinal detachment border (broad arrow; R). The GTV on T2 at the level of the choroid tended to be more circular shaped in contrast to the GTV on T1gd which had a sharper tumour-choroid interface (dotted arrow; patients 2, 5, 6 and 8). In patient 10, the flat tumour extension was missed by most observers (arrowhead).

The individual delineations showed that higher local SDs at the tumour-choroid interface corresponded with choroidal enhancement, which was included in the GTV by some but not all observers (figure 3.5C). In patient 9 (figure 3.4R), however, the high local SD in proximity of the retinal detachment was a result of partial inclusion of retinal detachment by one observer (ophthalmologist, insert figure 3.5D). Another area with a high local SD was observed in patient four due to wide tumour margin and partial inclusion of the levator palpebrae by an observer and omission of part of the tumour base in the GTV by another observer.

A.

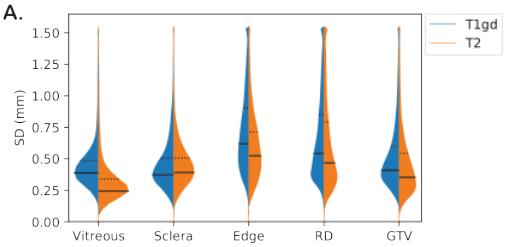

B.

Local SD	cT1	T2	
	Median; 75th perc	Median; 75th perc	p-value (n)
Vitreous	0.39 mm; 0.49 mm	0.24 mm; 0.34 mm	<0.001* (10)
Sclera	0.37 mm; 0.51 mm	0.39 mm; 0.51 mm	0.99 (10)
Edge	0.62 mm; 0.90 mm	0.52 mm; 0.71 mm	0.08 (10)
RD	0.54 mm; 0.85 mm	0.47 mm; 0.79 mm	0.35 (5)
GTV	0.41 mm; 0.60 mm	0.35 mm; 0.54 mm	0.12 (10)

perc = percentage, * significant difference

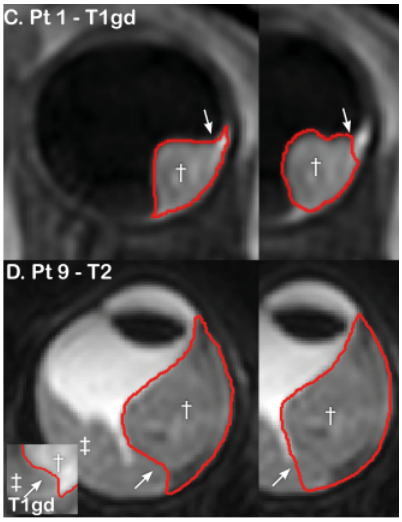

Figure 3.5: **Observer variation** (A,B) Distribution of the local observer variation per region for T1gd (left, blue) and T2 (right, orange) and entire GTV. A significant difference in the observer variation between T1gd and T2 was only found for the vitreous ($p < 0.001$). (C,D) Higher local SDs were found at the tumour-choroid interface and in proximity of retinal detachment (double dagger). Higher variation at the tumour-choroid interface was most likely a result of disagreement between observers about inclusion of (enhancing) choroid. Some observers included the enhancing choroid in the GVT (left) and others did not (right). Retinal detachment was not always clearly visible. An example of a patient where it can be challenging to differentiate retinal detachment from tumour based on T2 alone is shown in D.

As the local SD can depend on the type of tissue adjacent to the tumour, e.g. vitreous or retinal detachment, the observer variation was compared for four separate regions (figure 3.5). A paired t-test was used to compare the sequence dependent median local SD per patient for the four separate regions (figure 3.5). A significant lower local SD was found at the vitreous interface on T2 (T1gd: 0.39 mm vs T2: 0.24 mm, $p < 0.001$) and a similar trend for the tumour-choroid interface (T1gd: 0.62 mm vs T2: 0.52 mm, $p = 0.08$). This was in line with the 75th percentile of the local SD distribution for vitreous (T1gd: 0.49 mm vs T2: 0.34 mm, $p = 0.005$) and tumour-choroid interface (T1gd: 0.90 mm vs T2: 0.71 mm, $p = 0.15$). In line with the observations in figure 3.4, significant higher variations were found at the tumour-choroid interface compared to sclera, vitreous and retinal

detachment (figure 3.5 A&C, sclera- tumour - choroid interface; T1gd: p = 0.008 & T2: p=0.004, vitreous - tumour-choroid interface; T1gd: p = <0.001 & T2: p=0.002, vitreous-retinal detachment; T1gd: p = 0.03 & T2: p=0.001).

3.4 Discussion

We found in general an interobserver variation of 0.4 mm, which is essential information for the determination of the margin for MRI-based radiotherapy planning of intra-ocular tumours. This variation in significantly smaller than for other malignancies, such as pancreatic, prostate and recurrent gynaecological cancer, where observer variations in the order of 2mm-10mm are commonly found.[24,26–32]. The higher agreement between observers found in this study is likely the result of relatively high resolution of the MR-images, which is also needed for a small target organ, such as the eye[10]. The studies in the other malignancies, however, do illustrate that this variation can potentially be reduced even further, by improving the delineation instructions based on the results of this study. The observer variation of 0.4mm was approximately half of the acquisition voxel size (0.8 mm isotropic) and in line with previous eye segmentation studies showing a segmentation reproducibility of less than one voxel[33] [31,32]. It is also well within the 2.5 mm margin which is commonly used for ocular-PT planning worldwide [33–40]. This margin however also includes variation in patient set up between fractions, movement of the eye during treatment and uncertainties in the beam characteristics [34]. Assuming a margin of 2.5 times the SD of the systematic error + 0.7 times the random error [41], only a margin of 1 mm is needed for target definition.

As no prior publications were found on the observer variation of the GTV delineation in uveal melanoma on high resolution MRI scans, the observer variation was compared with uncertainties in conventional measurements for ocular-PT planning. Currently GTV definition of conventional ocular-PT planning is based on the distance between tumour and tantalum markers in combination with tumour prominence and largest basal diameter measurements on ultrasound and fundoscopy. Studies demonstrated an observer variation (standard deviation) with B-scan ultrasonography for prominence measurement of 0.6 mm [42] and 0.7 mm for the tumour base [43]. Furthermore, fundoscopic images are optically deformed and differ on average 1.2 mm from ultrasound measurements of the largest basal diameter [44]. Even though these uncertainties and variations are not directly comparable as they involve different types of measures, it indicates that the observer variation observed on MRI might be similar or smaller than the current standard. Comparison with CT, which is commonly used for ocular stereotactic radiosurgery [45], was not possible as no literature was found on the observer variation of interocular GTV delineation with CT.

We showed that the observer variation depends on the type of tissue adjacent to the tumour, with the lowest variation at the tumour-vitreous interface. The highest variation was observed at the tumour-choroid interface, especially on T1gd as there was no agreement on whether choroidal enhancement should be included in the

GTV. Although more clear instructions on whether or not to consider this choroidal enhancement as tumour will likely reduce the observer variation, it is more important to know if this enhancement contains tumour cells. Unfortunately, no histopathologic validation was found in the literature. On T2, the choroidal enhancing area is generally hyperintense compared to the tumour and isointense compared to vitreous and was therefore not included in the GTV. This is the primary source of the volume differences between T1gd and T2 segmented GTVs. Out of concern for choroidal microinvasion we recommend to include choroidal enhancement into the GTV until proven otherwise by histopathology. Clarity about the aetiology of enhancement and reduction of the observer variability around the tumour edge is most important for tumours located in close proximity of OARs such as macula and optic nerve. This is also relevant for application of MRI-based tumour models outside ocular-PT such as treatment decision making, brachytherapy planning or follow-up after treatment. Especially for brachytherapy, where the base of the tumour determines the size of the brachytherapy applicator, it is important to have an accurate and reliable determination of the tumour base.

Compared to the tumour-choroid interface and retinal detachment, the base of the tumour had a relatively low observer variation. Nonetheless, enhancing muscle insertions might result in increased variation locally when mistaken for tumour. Finally, extra care should also be taken in case of flat UM or tumours with flat extensions as these can be missed on MRI [9].

Even though T2 has a slightly, not significant, lower observer variation compared to T1gd, we recommend to delineate on T1gd as enhancement might represent tumour invasion which might be missed on T2. Moreover, differentiation between tumour and retinal detachment might be more difficult on T2. However, to achieve the most accurate GTV delineation it is important to use the multiple scan sequences for tissue differentiation and to choose the least affected sequence in case of motion artifacts. The determined observer variation aids in establishing the margin for MRI-based ocular-PT treatment planning. Furthermore, the regional SD differences might lead to different bundle design strategies by for example preferring the major axis of the tumour to be in the anterior-posterior direction. Outside proton beam therapy, MRI-based tumour models might be used for treatment decision making, brachytherapy planning and follow-up after treatment.

3.5 Conclusion

The interobserver variation of 0.4 mm on MRI is low with respect to the voxel size and currently used treatment margins in ocular-PT. Higher interobserver variation was found at the tumour-choroid interface due to unspecified enhancement. This localized increase in variation might be reduced by additional guidelines and training. We prefer to delineate based on the T1gd because of clearer tissue margins and assume peritumoral enhancement might represent tumour invasion.

3.6 References

[1] IKNL, *NKR cijfers*. [Online]. Available: https://iknl.nl/nkr-cijfers.

[2] A. D. Singh, M. E. Turell, and A. K. Topham, "Uveal melanoma: Trends in incidence, treatment, and survival," *Ophthalmology*, vol. 118, no. 9, pp. 1881–1885, 2011, ISSN: 01616420. DOI: 10.1016/j.ophtha.2011.01.040.

[3] J. Hrbacek *et al.*, "Practice Patterns Analysis of Ocular Proton Therapy Centers: The International OPTIC Survey," *International Journal of Radiation Oncology Biology Physics*, vol. 95, no. 1, pp. 336–343, 2016, ISSN: 1879355X. DOI: 10.1016/j.ijrobp.2016.01.040.

[4] S. Aziz, A. Taylor, A. McConnachie, A. Kacperek, and E. Kemp, "Proton beam radiotherapy in the management of uveal melanoma: Clinical experience in Scotland," *Clin Ophthalmol*, vol. 3, pp. 49–55, 2009. [Online]. Available: http://www.ncbi.nlm.nih.gov/pubmed/19668544.

[5] M. J. Sikuade, S. Salvi, P. A. Rundle, D. G. Errington, A. Kacperek, and I. G. Rennie, "Outcomes of treatment with stereotactic radiosurgery or proton beam therapy for choroidal melanoma.," *Eye (London, England)*, vol. 29, no. 9, pp. 1194–1198, 2015, ISSN: 1476-5454 (Electronic). DOI: 10.1038/eye.2015.109. [Online]. Available: http://dx.doi.org/10.1038/eye.2015.109.

[6] T. Niendorf *et al.*, *Ophthalmic Magnetic Resonance Imaging: Where Are We (Heading To)?* 2021. DOI: 10.1080/02713683.2021.1874021.

[7] J. W. M. Beenakker *et al.*, "MR-based clip-tumor measurements for proton beam therapy planning of uveal melanoma patients," English NR - 0 PU - WILEY PI - HOBOKEN PA - 111 RIVER ST, HOBOKEN 07030-5774, NJ USA, *ACTA OPHTHALMOLOGICA*, vol. 99, p. 26, 2021, ISSN: 1755-375X.

[8] I. J. Das, K. P. McGee, N. Tyagi, and H. Wang, "Role and future of MRI in radiation oncology," *The British Journal of Radiology*, vol. 92, no. 1094, p. 20 180 505, Nov. 2018, ISSN: 0007-1285. DOI: 10.1259/bjr.20180505. [Online]. Available: https://doi.org/10.1259/bjr.20180505.

[9] G. Yazici *et al.*, "Stereotactic Radiosurgery and Fractionated Stereotactic Radiation Therapy for the Treatment of Uveal Melanoma," *International Journal of Radiation Oncology*Biology*Physics*, vol. 98, no. 1, pp. 152–158, 2017, ISSN: 0360-3016. DOI: https://doi.org/10.1016/j.ijrobp.2017.02.017. [Online]. Available: https://www.sciencedirect.com/science/article/pii/S0360301617303954.

[10] T. A. Ferreira, L. G. Fonk, M. G. Jaarsma-Coes, G. G. van Haren, M. Marinkovic, and J. W. M. Beenakker, "MRI of uveal melanoma," *Cancers*, vol. 11, no. 3, pp. 1–20, 2019, ISSN: 20726694. DOI: 10.3390/cancers11030377.

[11] S. Marnitz *et al.*, "Proton Therapy of Uveal Melanomas," *Strahlentherapie und Onkologie*, vol. 182, no. 7, pp. 395–399, 2006, ISSN: 1439-099X. DOI: 10.1007/s00066-006-1512-1. [Online]. Available: https://doi.org/10.1007/s00066-006-1512-1.

[12] E. Fleury *et al.*, "3D MRI-based treatment planning approach for non-invasive ocular proton therapy," *Medical Physics*, 2020, ISSN: 0094-2405.

[13] M. K. Hassan *et al.*, "An automatic framework to create patient-specific eye models from 3D MR-images for treatment selection in patients with uveal melanoma," *Advances in Radiation Oncology*, p. 100 697, 2021, ISSN: 2452-1094. DOI: https://doi.org/10.1016/j.adro.2021.100697. [Online]. Available: https://www.sciencedirect.com/science/article/pii/S2452109421000555.

[14] H.-G. Nguyen *et al.*, "A novel segmentation framework for uveal melanoma in magnetic resonance imaging based on class activation maps," *Proceedings of Machine Learning Research*, 2019.

[15] H. G. Nguyen *et al.*, "Personalized Anatomic Eye Model From T1-Weighted Volume Interpolated Gradient Echo Magnetic Resonance Imaging of Patients With Uveal Melanoma," *International Journal of Radiation Oncology Biology Physics*, vol. 102, no. 4, pp. 813–820, 2018, ISSN: 1879355X. DOI: 10.1016/j.ijrobp.2018.05.004.

[16] K. Pfeiffer, B. Dobler, C. Rethfeldt, W. Schlegel, and R. Bendl, "OCTOPUS: A planning tool for proton therapy of eye tumours," in *Physica Medica*, 2001. DOI: 10.1007/978-3-642-59758-9_124.

[17] R. Via *et al.*, "Potential and pitfalls of 1.5T MRI imaging for target volume definition in ocular proton therapy," *Radiotherapy and Oncology*, vol. 154, pp. 53–59, 2021, ISSN: 0167-8140. DOI: https://doi.org/10.1016/j.radonc.2020.08.023. [Online]. Available: https://www.sciencedirect.com/science/article/pii/S0167814020307520.

[18] M. van Herk, "Errors and margins in radiotherapy," *Seminars in Radiation Oncology*, vol. 14, no. 1, pp. 52–64, 2004, ISSN: 1053-4296. DOI: https://doi.org/10.1053/j.semradonc.2003.10.003. [Online]. Available: https://www.sciencedirect.com/science/article/pii/S1053429603000845.

[19] C. Rasch, R. Steenbakkers, and M. van Herk, "Target Definition in Prostate, Head, and Neck," *Seminars in Radiation Oncology*, vol. 15, no. 3, pp. 136–145, 2005, ISSN: 1053-4296. DOI: https://doi.org/10.1016/j.semradonc.2005.01.005. [Online]. Available: https://www.sciencedirect.com/science/article/pii/S105342960500007X.

[20] B. A. Berkowitz, C. McDonald, Y. Ito, P. S. Tofts, Z. Latif, and J. Gross, "Measuring the human retinal oxygenation response to a hyperoxic challenge using MRI: Eliminating blinking artifacts and demonstrating proof of concept," *Magnetic Resonance in Medicine*, vol. 46, no. 2, pp. 412–416, 2001, ISSN: 07403194. DOI: 10.1002/mrm.1206.

[21] J. Wezel, A. Garpebring, A. G. Webb, M. J. P. van Osch, and J.-W. M. Beenakker, "Automated eye blink detection and correction method for clinical mr eye imaging," *Magnetic Resonance in Medicine*, vol. 78, 2017.

[22] S. Klein, M. Staring, K. Murphy, M. A. Viergever, and J. P. Pluim, "Elastix: A toolbox for intensity-based medical image registration," *IEEE Transactions on Medical Imaging*, vol. 29, no. 1, pp. 196–205, 2010, ISSN: 02780062. DOI: 10.1109/TMI.2009.2035616.

[23] F. Ritter *et al.*, "Medical Image Analysis: A Visual Approach," *IEEE Pulse*, vol. 2, no. 6, pp. 60–70, 2011, ISSN: 2154-2287. DOI: 10.1109/MPUL.2011.942929. [Online]. Available: http://ieeexplore.ieee.org/xpls/abs_all.jsp?arnumber=6088923&tag=1.

[24] R. J. H. M. Steenbakkers *et al.*, "Observer variation in target volume delineation of lung cancer related to radiation oncologist–computer interaction: A 'Big Brother' evaluation," *Radiotherapy and Oncology*, vol. 77, no. 2, pp. 182–190, Nov. 2005, ISSN: 0167-8140. DOI: 10.1016/j.radonc.2005.09.017. [Online]. Available: https://doi.org/10.1016/j.radonc.2005.09.017.

[25] T. A. Ferreira *et al.*, "MR imaging characteristics of uveal melanoma with histopathological validation," *Neuroradiology*, vol. epub, 2021. DOI: https://doi.org/10.1007/s00234-021-02825-5.

[26] O. J. Gurney-Champion *et al.*, "Addition of MRI for CT-based pancreatic tumor delineation: a feasibility study," *Acta Oncologica*, vol. 56, no. 7, pp. 923–930, Jul. 2017, ISSN: 0284-186X. DOI: 10.1080/0284186X.2017.1304654. [Online]. Available: https://doi.org/10.1080/0284186X.2017.1304654.

[27] E. Versteijne *et al.*, "Considerable interobserver variation in delineation of pancreatic cancer on 3DCT and 4DCT: a multi-institutional study," *Radiation Oncology*, vol. 12, no. 1, p. 58, 2017, ISSN: 1748-717X. DOI: 10.1186/s13014-017-0777-0. [Online]. Available: https://doi.org/10.1186/s13014-017-0777-0.

[28] M. Machiels *et al.*, "Reduced inter-observer and intra-observer delineation variation in esophageal cancer radiotherapy by use of fiducial markers," *Acta Oncologica*, vol. 58, no. 6, pp. 943–950, Jun. 2019, ISSN: 0284-186X. DOI: 10.1080/0284186X.2019.1588991. [Online]. Available: https://doi.org/10.1080/0284186X.2019.1588991.

[29] P. Steenbergen *et al.*, "Prostate tumor delineation using multiparametric magnetic resonance imaging: Inter-observer variability and pathology validation," *Radiotherapy and Oncology*, vol. 115, no. 2, pp. 186–190, May 2015, ISSN: 0167-8140. DOI: 10.1016/j.radonc.2015.04.012. [Online]. Available: https://doi.org/10.1016/j.radonc.2015.04.012.

[30] C. R. N. Rasch *et al.*, "Decreased 3D observer variation with matched CT-MRI, for target delineation in Nasopharynx cancer," eng, *Radiation oncology (London, England)*, vol. 5, p. 21, Mar. 2010, ISSN: 1748-717X. DOI: 10.1186/1748-717X-5-21. [Online]. Available: https://pubmed.ncbi.nlm.nih.gov/20230613%20https://www.ncbi.nlm.nih.gov/pmc/articles/PMC2842278/.

[31] D. Bernstein *et al.*, "An Inter-observer Study to Determine Radiotherapy Planning Target Volumes for Recurrent Gynaecological Cancer Comparing Magnetic Resonance Imaging Only With Computed Tomography-Magnetic Resonance Imaging," *Clinical Oncology*, vol. 33, no. 5, pp. 307–313, 2021, ISSN: 0936-6555. DOI: https://doi.org/10.1016/j.clon.2021.02.003. [Online]. Available: https://www.sciencedirect.com/science/article/pii/S0936655521000467.

[32] R. Steenbakkers *et al.*, "A 3D analysis and reduction of observer variation in delineation of lung cancer for radiotherapy," *International Journal of Radiation Oncology, Biology, Physics*, vol. 60, no. 1, S531–S532, Sep. 2004, ISSN: 0360-3016. DOI: 10.1016/j.ijrobp.2004.07.490. [Online]. Available: https://doi.org/10.1016/j.ijrobp.2004.07.490.

[33] M. G. Jaarsma-Coes *et al.*, "Measuring eye deformation between planning and proton beam therapy position using magnetic resonance imaging," eng, *Physics and imaging in radiation oncology*, vol. 16, pp. 33–36, Oct. 2020, ISSN: 2405-6316. DOI: 10.1016/j.phro.2020.09.010. [Online]. Available: https://pubmed.ncbi.nlm.nih.gov/33458341%20https://www.ncbi.nlm.nih.gov/pmc/articles/PMC7807689/.

4

Comparison of MRI-based and conventional measurements for proton beam therapy of uveal melanoma

M.G. Jaarsma-Coes, T.A. Ferreira, M. Marinkovic, T.H.K. Vu, L. van Vught, G.R. van Haren, M.F. Rodrigues, Y.L.B. Klaver, B.M. Verbist, G.P.M. Luyten, C.R.N. Rasch, J.W.M. Beenakker

This chapter has been published in Ophthalmology Retina[1]

Conventionally, ocular proton beam therapy (PT) is planned using measurements obtained by an ophthalmologist using ultrasound, fundoscopy, biometry and intraoperative assessments. Due to recent advances in magnetic resonance imaging (MRI) of uveal melanoma (UM), it is possible to acquire high resolution three-dimensional images of the eye providing the opportunity to incorporate MRI in ocular PT planning. In this study we describe how these measurements can be obtained with MRI, compare the MR-based measurements with conventional ophthalmic measurements and identify potential pitfalls for both modalities. Data from twenty-three consecutive UM patients treated with PT were retrospectively evaluated. MRI-based measurements of axial length, tumor height and basal diameter, and marker-tumor distances were compared to the conventional ophthalmic measurements and discrepancies were evaluated in a multi-disciplinary setting. The mean absolute difference of the tumor height and basal diameter measurements between ultrasound and MRI were 0.57mm and 1.44mm respectively. Larger absolute differences in height and basal diameter were observed when the full tumor extend was not visible on ultrasound (0.57mm and 1.67mm respectively) compared to when the full tumor visible (0.44mm and 1.15mm). When the full tumor was not visible on ultrasound MRI was considered more reliable. MRI and intraoperative measured tumor-marker distances differed <1mm in 55% of the markers. For anterior located and mushroom shaped tumors (25% of the markers) MRI provided more accurate measurements. In flat UM (15% of the markers) however, it was difficult to delineate the tumor on MRI. The mean absolute difference in axial length between optical biometry and MRI was 0.50mm. The tumor presence was found to influence optical biometry in 15/22 patients, the remaining patients showed a better agreement (0.30mm). MRI-based biometry were considered more reliable in UM patients. MRI allowed for 3D assessment of the tumor and surrounding tissue. In specific patients it provided a more reliable measurement of axial length, tumor dimensions and/or marker-tumor distances, and could contribute to a more accurate treatment planning. Nevertheless, a combined evaluation remains advised, especially for flat UM.

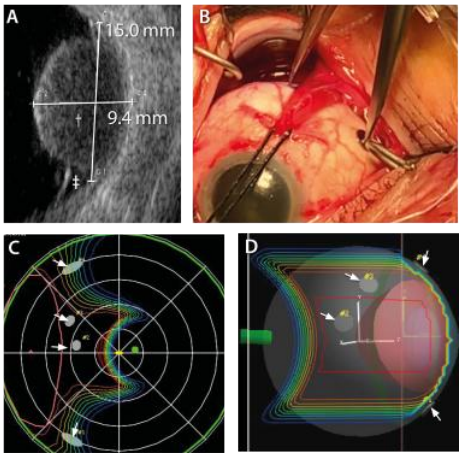

Figure 4.1: Ophthalmic measurements. (A) Ultrasound measurements of tumor (dagger) prominence and basal diameter. Note the associated retinal detachment (double dagger). (B) Peroperatively, the distance between tumor and marker and distance between markers is measured using a capilar. (C,D) ocular-PT plan with the planned dose distribution. In the fundus view (C), the peroperative and ultrasound measurements are used to define the tumor base, from which a geometric 3D model (D) of the eye including the tumor (red) and markers (arrows) is constructed.

4.1 Introduction

Uveal melanoma (UM) is the most common primary intraocular malignancy in adults, with an incidence up to 14 cases per million person-years[2,3]. Proton beam radiation therapy (PT), when available, is often the preferred treatment for larger UM and tumors that encircle the optic nerve. In the preparation for ocular-PT, radiopaque (tantalum) markers are sutured to the sclera near the tumor border by an ophthalmologist for treatment planning and position verification during treatment[4].

Currently, ocular-PT is planned using a geometrical tumor and eye-model, based on data from different, mostly ophthalmic, sources such as ultrasound and fundoscopy[5] (figure 4.1). In this model, the eye is scaled to the patient's axial length, as obtained by biometry. Additionally, the transversal diameter of the eye, combined thickness of the retina, choroid and sclera, lens position and thickness and limbus diameter can be personalized. The tumor geometry is primarily based on its height and basal diameters, as obtained from ocular ultrasound (figure 4.1A), while intraoperatively obtained marker-tumor distances and fundus photographs are used to define the tumor base (figure 4.1B).

Although this approach results in high rates of over 95% of local control,[4,6] this comes at the cost of a significant reduction of visual acuity, approximately 45% of the eyes losing over 3 snellen lines in 10 years.[7–9] Part of this vision loss can be attributed to the relatively large safety margins, of up to 3mm[6], which are required to mitigate different uncertainties in treatment planning and delivery, including uncertainties in tumor geometry and location.

Ocular MRI has become a valuable tool in the diagnosis, therapy selection and follow-up of UM-patients.[10–13] Similarly to malignancies in other body parts, MRI has the potential to reduce uncertainties in ocular-PT, and thereby contribute to strategies to reduce the radiation induced side-effects[14]. In particular, MRI could potentially provide valuable information for current treatment, model-based, planning as it provides (I) 3D visualization of the tumor and its surrounding structures[4,15,16], (II) tumor and globe dimensions including transversal diameter which cannot be measured using ophthalmic imaging techniques[16–19] and (III) depiction of the surgical markers in relation to tumor and eye[20].

In this study we describe and evaluate a dedicated MRI protocol to obtain the geometrical measurements that can be used to complement conventional measurements for ocular-PT planning. We compared MRI-based measurements with conventional opthalmic measurements of the axial eye length, height and largest basal diameter of the tumor and marker-tumor distances and identify potential pitfalls for both conventional and MRI based measurements.

4.2 Materials and Methods

Clinical data of twenty-three consecutive patients with UM, diagnosed by an ocular oncologist, between December 2019 and October 2020 and treated with ocular-PT, were evaluated retrospectively. Patients were referred to HollandPTC (Delft, The Netherlands) for ocular-PT if the UM was located juxtapapillary (26%) or when the tumor dimensions exceeded the local criteria for ruthenium plaque brachytherapy (height including sclera $>$7mm and/or basal diameter $>$16mm)[21,22] (74%). Patients underwent a diagnostic MRI-protocol on a 3T MRI scanner (Ingenia Elition, Philips Healthcare, Best, The Netherlands), as part of clinical care, to confirm eligibility and localize the tumor in 3D (a detailed description is provided in section 2.2). Additionally, a second, shorter, MRI-protocol is performed 7-14 days after the markers placement to determine the tumor-marker distances. The study was conducted according to the guidelines of the Declaration of Helsinki, and approved by the Ethics Committee METC Leiden Den Haag Delft (G20.16, January 4th 2021). Informed consent for retrospective use of their clinical data was obtained from all participants.

4.2.1 Conventional measurements for treatment planning

The axial length of the affected eye in millimeters was obtained using optical biometry (Lenstar LS900, Eyesuite biometry V2.7.1, Haag-Streit diagnostics, Koeniz, Bern) performed by an optometrist. Three aspects were evaluated for the affected eye: (I) the extended outputs of the biometer for signs of an unreliable measurement[23], (II) the iris decentration, as an objective test of whether the measurement was performed along the visual axis[24] and (III) presence of tumor or retinal detachment in the posterior pole. Further details are described in figure 4.4 and supplement 4.6.

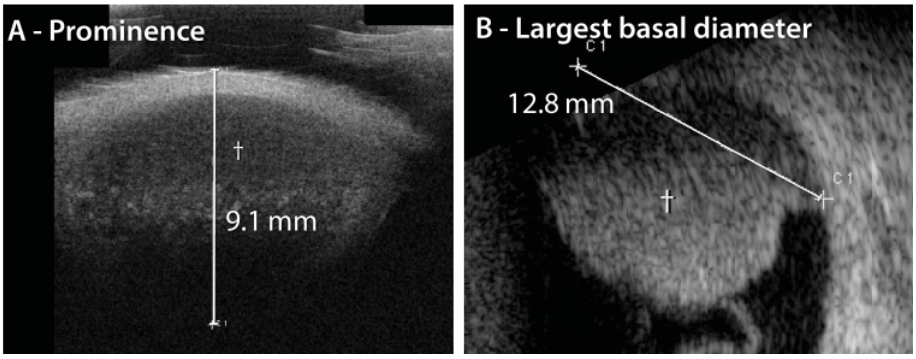

Figure 4.2: On ocular ultrasound, the full extent of the tumor (dagger) cannot always be visualized due to its limited penetration depth (A) or field of view (B). These measurements were marked as unreliable and analysed separately.

Tumor size was measured using ocular B-mode ultrasound (Aviso, Quantel medical, Cournon d'Auvergne, France) as part of clinical care by their ophthalmologist. For patients with an anteriorly located tumor, additional images were acquired using an ultrasound biomicroscopy (UBM) probe. To obtain tumor height, the distance of the highest point of the tumor to sclera was measured perpendicular to the scleral surface. The sclera was included for reliable, consistent measurements. The largest basal tumor diameter (LBD) was then obtained and the second diameter (SBD) was defined as the largest diameter perpendicular to this measurement. All ultrasound images were retrospectively evaluated by an ocular oncologists and a physicist to assess if the complete tumor base and apex were visible (figure 4.2). Final scores were based on consensus.

After markers placement, the distance between the centre of the markers and the edge of the tumor (marker-tumor distances) were measured intraoperatively for each marker using a calliper. Simulations of transpupillary illumination measurements were performed using ray-tracing, as developed by van Vught et al[25], for one representative patient (details can be found in supplement 4.7) to assess how the tumor blocks part of the light rays, introducing a penumbra.

4.2.2 MRI

MRI's were performed as described by Ferreira et al[11]. In short, a 4.7 cm surface receive coil (Philips Healthcare) was used to image the affected eye. A radiotherapy head support was used for patient fixation. The MRI protocols are summarized below and in table 4.1. A more detailed description, including planning of the scans can be found in supplement 4.8.

The MRI before marker surgery was used for baseline evaluation of the UM and measurements of the tumor and eye geometry. The protocol included 3D isotropic volumetric scans to assess the tumor and eye geometry, 2D scans to evaluate tu-

Table 4.1: **Scan parameters**

Purpose	Scan name	Voxel Size (mm^3)	TE(ms)/TR(ms) /Flip or ref. angle (deg)	Scan time (mm:ss)	Additional parameters
Pre-operative scan					
3D measurements	3DT1 TSE	0.8x0.8x0.8	26/400/90	02:07	
	3DT1 TSE SPIR	0.8x0.8x0.8	26/400/90	02:07	
	3DT1 TSE SPIR gd	0.8x0.8x0.8	26/400/90	02:07	
	3DT2 TSE SPIR	0.8x0.8x0.8	305/2500/35	02:58	
Tumor origin & extension	MST1 TSE	0.5x0.5x2	8.0/400/90	00:43	
	MST1 TSE SPIR gd	0.5x0.5x2	8.0/400/90	00:43	
	MST2 TSE	0.4x0.4x2	90/2256/90	01:08	
Functional scans	DWI (TSE)	1.3×1.4×2.4	50/1555/50	1:33	B = 0, 800 s/mm^2
	DCE	1.3×1.5×1.5	2.3/4.5/13	4:00	2 s/dynamic
Post-operative scan					
Marker localization	3DT1 GE	0.9x0.9x0.9	2.0/7.0/9	00:43	BW = 812 Hz
	3DT1 TSE	0.8x0.8x0.8	27/400/90	02:07	BW = 758 Hz
	3DT2 TSE	0.8x0.8x0.8	294/2300/35	02:43	BW = 943 Hz
Tumor base localization	MST1 GE gd†	0.6x0.6x2	2.8/7.0/9	00:33	BW = 532 Hz
	3DT1 TSE gd∗	0.8x0.8x0.8	25/400/90	02:07	BW = 758 Hz
	MST2 TSE gd†	0.4x0.4x2	90/943/90	01:04	BW = 354 Hz
Marker-tumor distance	MST1 GE gd†	0.6x0.6x2	2.8/7/9	00:25	BW = 532 Hz
	MST1 TSE gd∗	0.5x0.5x2	6.0/718/90	00:43	BW = 658 Hz
Check for motion	MST1 GE gd†	0.6x0.6x2	2.8/7.0/9	00:33	BW = 532 Hz
Screen for inflammation	3DT2 TSE SPIR gd†	0.8x0.8x0.8	297/2300/35	02:43	BW = 943 Hz

Although the patients in this study did not receive a contrast agent for the post-operative MRI, we advise to perform the post-operative scans with contrast to aid in the differentiation between tumor and retinal detachment. As such, the scans with an asterisk (∗) were not performed in this study and the scans with a dagger (†) were scanned without contrast agent. FOV: Field-of-View, TE: echo time, TR: repletion time, TSE: turbo spin echo, SPIR: Spectral Presaturation with Inversion Recovery, gd: gadolinium, GE: gradient echo, MS: multi-slice, DWI: Diffusion Weighted Imaging, DCE: Dynamic contrast enhanced scan, BW: bandwidth

mor origin and extension and functional scans to assess the tumor diffusivity and perfusion[11,16].

After surgery, a second MRI was performed to assess the markers-tumor relation. These scans were acquired with stronger gradients and localized shimming to limit the signal voids caused by the susceptibility artefacts of the tantalum markers. 3D isotropic volumetric scans were acquired for marker localization and comparison with preoperative MRI. Additionally, for each marker a gradient echo T1- and a spin echo T2-weighted 2D scan, perpendicular to the tumor base, were acquired, figure 4.3D.

4.2.3 Evaluation of the pre-surgery MR-images

All MR images were evaluated by one of the neuroradiologists specialized in the eye at our center using Sectra IDS7 (v21.1, Sectra AB, Linköping, Sweden). In case of doubt, a second reader evaluated the scans and final measurements were based on consensus. First, an evaluation of the tumor was performed, including screening for extra-scleral extension and invasion of the ciliary body or optic nerve.[16] Additionally, both functional scans were assessed to confirm that the lesion matched the general characteristics of UM, and to provide a baseline for the follow-up after PT[16].

Subsequently, PT specific measurements were obtained. The axial length of the eye, measured from the anterior wall of the cornea until the posterior wall of the retina, was preferably obtained from the 3D-T2 scans, as on T2-weighed sequences the

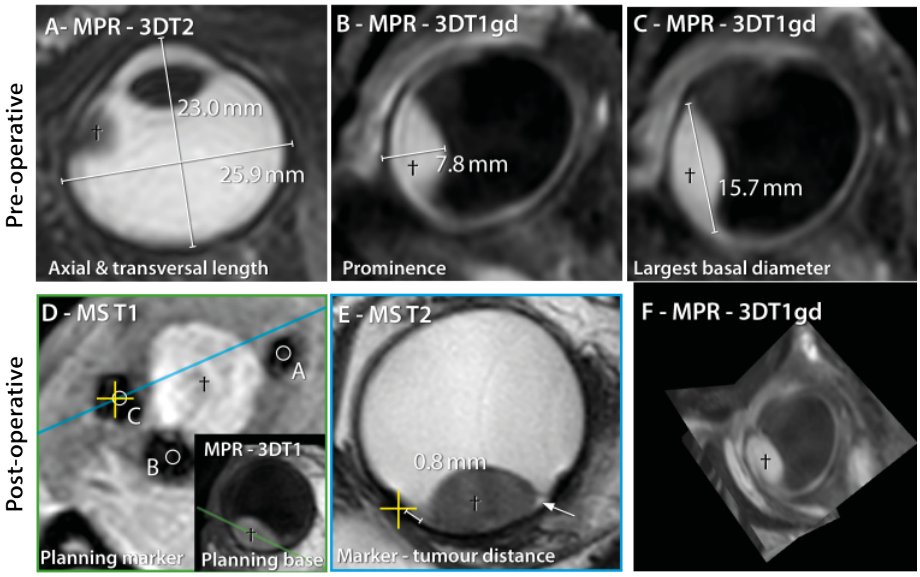

Figure 4.3: Primary pre- and post-operative MRI based measurements. (A) The axial length and transversal length were measured on a multi planar reconstruction (MPR) of the 3DT2. (B,C) The prominence, including sclera, and largest basal diameter were measured on a MPR of the 3DT1gd. (D) A multislice T1 scan was acquired through the base of the tumor (dagger). Subsequent scans per marker (T2 (E) and T1) were acquired perpendicular to this plane through the center of the tumor and marker. (E) Multislice T2 used to measure the distance between tumor and marker. Note the small retinal detachment adjacent to the UM (arrow) (F) 3D volumes as acquired with MRI allow for multi planar reconstructions (MPR) in all directions providing the opportunity to accurately determine the largest basal diameter, prominence and visualize the relation between tumor and surrounding tissue.

cornea is generally better depicted than on T1. As the optical or visual axis cannot be directly obtained from an MRI scans[26], the axial length was measured perpendicular to the lens plane and through the center of the lens or pupil (figure 4.3A). The transversal diameter of the eye was obtained in the same plane perpendicular to the eye length and it includes the sclera thickness bilaterally. The combined thickness of the sclera, choroid and retina was measured on the contrast enhanced MS-T1, as it provides a high in-plane resolution and good contrast between the sclera, choroid/retina and vitreous body.

Tumor height, largest and second basal diameter were primarily measured on contrast enhanced 3D-T1 images (figure 4.3B,C), as its isotropic resolution allowed for multiplanar reconstructions (figure 4.3F), enabling measurements of the tumor dimensions in every possible direction, and because on these images the tumor is well differentiated from the retinal detachment. Moreover, the outer limit of the sclera can clearly be identified on these images[11]. When severe motion artefacts were present or in case of retinal detachment obscuring delineation between tumor and retinal detachment, the 3D-T2- or the contrast-enhanced 2D-T1-weighted images were used. To allow comparison between ultrasound and MRI measurements, tumor height was measured including the sclera. For the PT planning, the sclera thickness was later subtracted.

4.2.4 Evaluation of the post-surgery MR-images

Tumor dimensions and retinal detachment were compared to the pre-surgery images to assure no significant tumor growth or increase of the retinal detachment had occurred. Additionally, fat-suppressed T2-weighted images were evaluated for presence of substantial inflammatory reactions that could have been induced by the surgery.

For each marker, the shortest distance between tumor base and marker edge (MT-distance) was measured (figure 4.3E). For some mushroom shaped tumors, an additional measurement was obtained from the marker to the projection of the overhanging intra-ocular tumor component on the sclera. This measurement was used to ensure the entire tumor was incorporated in the radiation field, because the treatment planning system used, Eclipse Ocular Proton Planning (EOPP, Varian Medical Systems, Palo Alto, CA, USA), cannot incorporate a mushroom geometry.

4.2.5 Comparison between the ophthalmic and MRI-derived measurements

Conventional biometry, ultrasound and interoperative measurements were compared with MRI based measurements. Differences exceeding 0.5 for prominence and 1.0mm for the other measurements were evaluated in a multidisciplinary setting. A paired t-test was used to test for systematic differences between ophthalmic and MRI-derived measurements. Additionally, the inter quartile range (IQR, 25^{th} and 75^{th} percentile)were determined.

4.3 Results

In 48% of the 23 cases, the UM was in the right eye. According to the American Joint Committee on Cancer (AJCC, 8th edition)[27], tumor classes ranged from T1 to T4, although the majority (65%) of the tumors were stage T3. Five lesions were characterized as (partly) flat by the ophthalmologist based on fundoscopy and ultrasound. In the majority of the patients, four tantalum markers (Altomed, Boldon, United Kingdom) were sutured on the outside of the sclera. In one patient, however, only three markers were used, and in another patient five markers were used. The time between the two MRI scans was on average 19 days (range: 7- 49). No change in tumor geometry had been observed, only an increase in retinal detachment.The differences and potential source of the discrepancies between conventional and MRI measurements are reported below. A detailed description per patient can be found in supplement 4.9.

4.3.1 Eye geometry

MRI reported on average a longer axial length compared to biometry, IQR -1.10- -0.19mm ($p<0.001$) and a mean absolute difference of 0.66mm, figure 4.4A. In 8 patients the difference between MRI and biometry exceeded 1.0 mm. In the majority of these patients (75%, n=6) the tumor or retinal detachment was present in the posterior pole, and/or the biometry showed signs of an unreliable measurement (50%,n=4). In one patient the MRI measurement was found to be incorrect as the sclera was included in the measurement (supplementary figure 4.7D). However, in 15 out of 22 eyes, the extended evaluation of the biometry output, showed signs of a potential inaccurate measurement, such as a large iris decentration. In these patients, a larger mean absolute difference 0.8 (IQR of the difference: -1.1- -0.4) was observed than in the remaining seven patients with unaffected measurement: 0.3mm (IQR of the difference:-0.34- -0.06mm) (figure 4.4A,B and supplement 4.6).

4.3.2 Tumor geometry

There was no overall significant difference between MRI and ultrasound based tumor height measurements (IQR:-0.4-0.5mm, p=0.75, figure 4.5A,C). The measurements had a mean absolute difference of 0.57mm. In 6 patients the tumor apex was not visible on the ultrasound images, figure 4.2A. These patients showed a larger absolute difference between MRI and ultrasound than the remaining patients where the tumor apex was visible, 0.92mm vs 0.44mm respectively. In 10 patients the difference between ultrasound an MRI exceeded 0.5mm. In 50% of these patients the tumor apex was not visible on ultrasound and the multidisciplinary tumor board considered MRI more reliable for these patients. Remaining differences exceeding 0.5mm were found in flat melanomas or oblique oriented tumors with a complex shape (figure 4.5C). A more extensive description of the individual cases can be found in supplement 4.9.

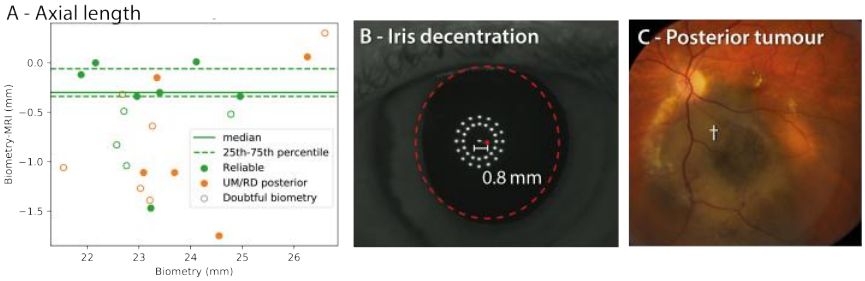

Figure 4.4: (A) Difference between MRI-based and biometry-based eye length measurements. For all patients including doubtful biometry (open dots) and patients with a UM or retinal detachment (RD) in the posterior pole (orange dots) on average 0.6 mm shorter measurements were found. For the remaining patients (filled green dots), there was generally a good agreement between both techniques, except for one patient where part of the sclera was included in the MRI measurement. (B,C) Two examples of doubtful biometry measures: (B) a large iris decentration is a sign the measurement was not obtained along the optical axis. (C) As the UM is covering the macula, the biometer reports a too short axial length.

There was no significant difference between the average of all 23 MRI and ultrasound based largest basal diameter measurements (IQR:-0.95-1.35mm, p=0.39, figure 4.5B,D). The measurements had a mean absolute difference of 1.44mm. In 14 patients the difference between ultrasound an MRI exceeded 1mm. In 57% of these patients (n=8) the full extent of the tumor base was not visible on ultrasound and as a result the MRI was considered more reliable. In three patients with a flat melanoma there was uncertainty about the accuracy of the MRI measurement. In one patient a hyperintense enhancing region adjacent to the tumor was included on ultrasound but not included in the basal diameter on MRI (figure 4.5D). Similarly, in one patient choroidal thickening adjacent to the tumor was not included in the MRI measurement whereas it was included in the ultrasound measurement. For the nine patients where the complete tumor base was visible on ultrasound (figure 4.2), the mean absolute difference was 1.15mm (IQR of the difference:0.70-1.40mm), compared to 1.67 (IQR: -1.80-1.30) when the tumor base was not completely visualized. Similar results were found for the second basal diameter measurements with a median absolute difference of 0.7mm (IQR of the difference:-0.43-1.33mm) for 13 patients with the entire tumor in the field of view.

4.3.3 Marker-tumor distances

In one patient one of the marker-tumor (MT)-distances could not be measured intraoperatively. MRI reported on average larger MT-distances compared to the intraoperative measurements (figure 4.6, mean difference:1.2mm, $p<0.01$). For 39 of the 87 (45%) evaluated markers, the difference between both measurements exceeded 1mm. MRI showed a larger MT-distance for the majority of these markers (n=30). The multidisciplinary evaluation of markers with a difference exceeding 1mm revealed four primary reasons for these differences. First, differences were found in 13 of the 18 markers in patients with flat melanomas. For these tumors

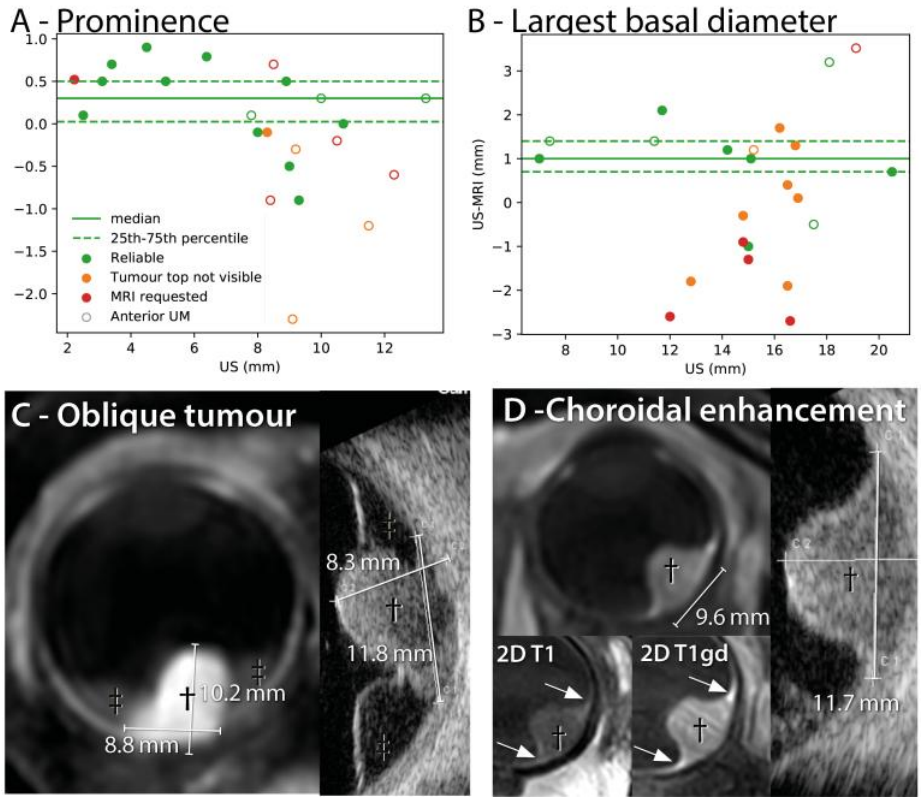

Figure 4.5: Comparison between ultrasound and MRI measurements of the tumor geometry (A) For 5 patients (red), an MRI was requested due to doubts on the accuracy of the ultrasound measurements. Additionally, 7 ultrasound measurements were scored as potentially inaccurate (orange), as they did not show the complete tumor in the FOV. Notably, for 10 of these 12 patients the tumor was located anteriorly (open markers). Overall, the largest differences were observed in anterior UM. (B) For the patients with an reliable ultrasound measurement, an average absolute difference between both techniques of 1.2 mm for the largest and 1.6 mm for the second basal diameter was found. Overall, the largest differences were observed in unreliable ultrasound measurements. (C) Prominence measurements for oblique oriented tumors are not well defined and can differ between observers on both ultrasound and MRI. (D) On MRI, choroidal enhancement was not included in the basal diameter measurements. On ultrasound however, this appears to be included.

A	Markers	OR – MRI (mm)	
	N (%)	Mean (abs)	Largest
All markers	87 (100%)	-1.2 (2.0)	-13.9
<1 mm diff	48 (55%)		
>1 mm diff	39 (45%)		
Flat tumours	13 (15%)	-1.6 (5.2)	-13.9
Complex MT relation	13 (15%)	-3.0 (3.2)	-7.9
Shadow	9 (10%)	-3.7 (3.7)	-8.0
Interchanged annotation	4 (5%)	-0.6 (2.3)	-2.9

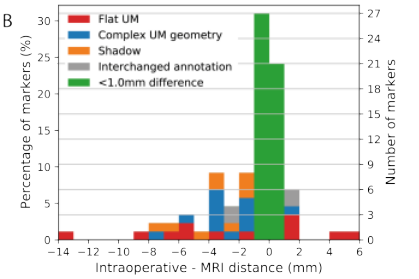

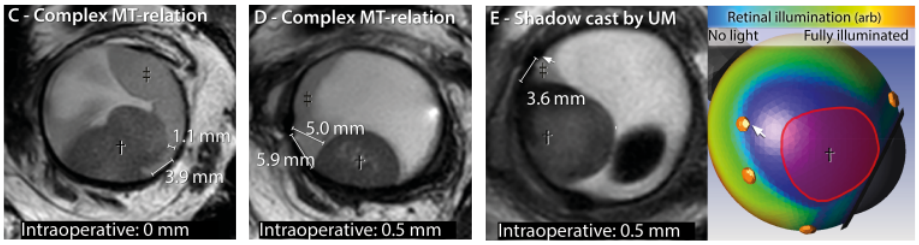

Figure 4.6: Intraoperative marker-tumor distances measurement compared with MRI based measurements. A negative value means that the MRI distance was larger than the interoprative measurement. (A,B) In 55% of the markers a difference of less than 1 mm was observed (green). The largest differences, up to 14 mm, were observed in flat melanoma (red). For 25% markers the difference was attributed to a complex tumor geometry (blue) or shadow cast by the tumor (orange). (C,D) For tumors with a complex marker-tumor relation one length might not be sufficient to describe the marker tumor relation. (E) For anterior located tumors the distance between posterior markers and tumor can be underestimated interoperatively due to a shadow that is cast by the tumor

the extent was difficult to assess on MRI, and the intraoperative measurements were generally considered more reliable. Secondly, differences were found in 13 markers with a complex marker-tumor relation (figure 4.6A-D). For markers located far from the tumor and in case of mushroom shaped tumors, the MT-distance could not easily be captured in a simple one-dimensional distance measurement, which likely accounts for the observed differences between both modalities. Thirdly, for anteriorly located tumors the shadow cast during transillumination could cause an overestimation of the tumor extent for a posteriorly located marker (9 markers, figure 4.6E). Personalized optical ray-tracing simulations confirmed this shadow and showed that for this specific patient the shadow extended until the location of the markers, matching the intraoperative marker-tumor measurements. Finally, in two patients the intraoperative annotation of two markers appeared to have been interchanged.

4.4 Discussion

In ocular-PT, geometrical information from different, mostly ophthalmic, sources are combined to construct a model of the tumor and eye for treatment planning4,12. In this study, we compared MRI-based and conventional measurements used to

construct such a model, and showed that in specific conditions MRI can improve the accuracy of this model. In line with earlier studies by Daftari[28], Marnitz[29] and Via[30], this improved accuracy can contribute to strategies to reduce the irradiated volume, and thereby reduce the radiation induced side-effects.

A general benefit of MRI was that 3D information of tumor, markers and surrounding anatomy are available to all specialists involved in the treatment, and can be used to evaluate the full 3D tumor geometry. For example, with MRI the relation between tumor and markers can be visualized in 3D, whereas conventionally only a 2D projection is available, figure 6E and supplement B. In this context, the multiplanar reconstructions proved to be beneficial to translate the clinical observations of the ocular oncologist to the treatment planning.

Overall, small differences were observed between MRI- and ultrasound-based height and LBD measurements, which in line with an earlier study[16]. However, we observed larger differences when the full tumor extent was not visible on ultrasound, which in some of the patients was attributed to the lower penetration depth of the UBM-probe (mean absolute difference reliable height measurements: 0.44mm vs unreliable: 0.76mm and LBD: 1.15mm vs 1.67mm). As MRI could visualize the complete extent of the tumor and 3D reconstructions could be made regardless of the location of the tumor, MRI was considered more reliable for these tumors. Interestingly, the majority (14/20) of these unreliable measurements concerned anteriorly located tumors and in 43% of these patients, the ophthalmologist had already doubts on the accuracy of the measurements during the ultrasound exam and had therefore requested an MRI to confirm the measurements. Although in general the reproducibility of MRI measurements can be hampered by differences in window level settings between observers, we recently reported a 0.4mm observer variation in MRI-based tumor delineation[31], which is slightly better than the 0.6-0.7mm variation reported for B-scan ultrasound[32,33]. Fundoscopic images can be used for measurement of the LBD and gross tumor volume (GTV) definition4, but the optical aberrations present in these images can result in large, 1.2mm, differences compared to ultrasound,[34] making this technique less desirable to assess tumor dimensions. Nevertheless, a combined evaluation is certainly advised, especially for flat UM.

It should be noted that this cohort predominantly contained larger tumors, which often have a complex geometry, as the majority of smaller UM are treated with brachytherapy at our center. The results from this study can therefore not be generalized to complete population of UM patients, as the full extent of smaller tumors, for example, can generally be accurately visualized on ultrasound. In this context, ultrasound remains one of the principal modalities for the diagnosis for intraocular masses, as it is a less expensive, faster and, for ophthalmologists, a more accessible imaging modality than MRI.

In the majority (55%) of the patients, the MRI and intraoperative MT-distances differed less than 1.0mm. For flat melanomas, the intraoperative MT-distances were generally considered more reliable, as the edge of the flat parts of the tumor are difficult to determine with MRI, while they can be accurately be determined

through transillumination in combination with fundoscopy. It is recognized in the field that, especially for more prominent anterior tumors, a surgeon can be misled by a penumbra during transpupillary transillumination[35]. Our results show that the posterior extent of anteriorly located tumors can indeed be overestimated intraoperatively up to 8mm, even when a combination of trans-pupillary transillumination and trans-ocular transillumination is used. The amount of overestimation depends on multiple factors, including pupil diameter, tumor height and presence of retinal detachment or hemorrhage. Therefore, for anteriorly located tumors, MRI can be considered a more reliable technique to determine the posterior extension of the tumor than the conventional optical techniques.

For both tumor height and MT-distance measurements, differences between conventional and MRI based measurements were in some patients attributed to a complex 3D tumor geometry, where, a different interpretation of the height and basal diameter was found between the radiologists and ophthalmologists. A more precise definition, incorporating how to evaluate complexly shaped tumors on 3D imaging, will likely aid in more uniform measurements and subsequent PT planning. However, these tumors clearly show that the conventional one-dimensional measurements poorly describe the tumor geometry and relation to the markers. The different efforts working towards MRI-based ocular-PT planning[36–38] will therefore likely enable a more precise incorporation of the tumor and marker relation[15,29,30,36–39].

In 15 out of 22 patients the biometry showed signs of a potentially erroneous measurement due to the UM, explaining the large differences of up to 1.8mm compared to MRI. For the patients with a reliable optical biometry measurement, however, a good agreement ($<$0.4mm difference) was found between MRI and biometry. This is similar to the 0.1mm difference found in earlier studies with healthy eyes using automatic analysis of the MRI scans[18,26]. Moreover, MRI measurements of the axial length were found to be reproducible and a good alternative when biometry cannot be obtained reliably[19]. In the past, ultrasonic biometry has been used[5], however, optical biometry has become the gold standard in ophthalmology due to its higher accuracy and reproducibility, except for patients where optical evaluations are not possible, for example in case of a dense cataract or vitreous hemmorage.[40] Alternatively, using data from the contralateral eye has been proposed, as it is unaffected by intra-ocular pathologies. However, as eye lengths can differ between both eyes,[41] this can be less accurate than MRI-based measures of the affected eye, as is further assessed in supplement 4.7.

This study also showed some limitations in the used MRI methods. Similar to ultrasound, the extension of the (partially) flat UM could not always be determined reliably. Although MRI has a superior soft tissue contrast compared to ultrasound[17,42], these flat UMs could not always be differentiated from the choroid. Secondly, in two patients, on MRI a hemorrhagic or thickened and more enhancing choroid was observed directly adjacent to the tumor. Although this was not included as part of the tumor in both the basal diameter and marker-tumor measurements, histopathological confirmation is needed for this interpretation. Finally, to improve the differentiation between tumor and retinal detachment we started administering a contrast

agent for the post-operative scans. It is therefore important to acknowledge these limitations of MRI and combine information from the different available sources to determine which measurement is the most reliable.

In the majority (20/23) of the studied patients at least one of the measurements used for treatment planning of ocular-PT was considered to be more reliable on MRI. Although the clinical implications of the inclusion of these MRI-based measurements on the final treatment plan need further evaluation, it is likely that MRI can reduce the uncertainties in ocular-PT. Such a clinical evaluation should also consider the added costs of the MRI. Although healthcare costs vary greatly between countries, MRI is generally more expensive than ultrasound (e.g. 300€ and 100€ respectively in the Netherlands),[43] However, the increased cost of including MRI is relative small compared to the costs of proton beam therapy or costs associated to vision loss (10.000€-30.000€).[44,45] As a result, including MRI in the preparation for ocular-PT is likely cost effective, as has been shown earlier in the context of treatment decision making[46].

Although this study shows the benefit of including MRI in the planning for ocular PT, the importance of the ophthalmic evaluations should not be underestimated. As ophthalmic imaging data can contain information that is missed on the MRI, such as the presence of a flat tumor extension, a combined evaluation of all available imaging data remains advised.

4.5 Conclusions

MRI provides valuable information for the planning of ocular-PT as it allows for a three-dimensional assessment of the tumor and surrounding tissue. In specific cases, it provided more reliable measurements of axial length, tumor dimensions and/or marker-tumor distances. Nevertheless, a combined evaluation, including ultrasound and optical imaging, remains advised, especially for flat UM.

4.6 Appendix - Optical biometry in uveal melanoma

4.6.1 Introduction

As ocular biometers are designed to obtain ocular geometric measurements to assist in IOL power calculations for cataract surgery[23], it might provide erroneous results when it is used in a different context such the scaling of an eye-model for radiotherapy planning for patients with an intraocular mass. The biometer, for example, assumes that the laser is reflected at the inner limiting membrane of the retina. For patients with an intraocular mass, however, the mass or associated retinal detachment, could also reflect the light, resulting an apparent shorter eye. Moreover, instructing the subject to stare at a fixation light normally guarantees that the eye length is measured from the cornea to the fovea. However, when the central vision is affected by the tumor patients tends to focus with their peripheral retina. As a result, the obtained axial length measurement does not correspond to the eye length.

Furthermore, in clinical practice it is recognized that for UM patients axial length measures can be inaccurate due to tumor presence, in which cases often the axial length of the contralateral eye is used. However, in 24% of the general population there is a more than 0.3mm difference in axial length between both eyes.[41] The asymmetry between eyes increases with an increase in axial length. The 95th centile of the axial length difference was 0.5 mm when the longer eye was $\leq$ 22.0 mm and 4.0 mm when it was $\geq$ 28 mm.[41]. We therefore compared the axial length measurement on MRI with the optical biometry measurement of the affected and contralateral eye.

4.6.2 Methods

On MRI, the axial length of the eye was preferably obtained from the 3D-T2 MR-images, as on T2 the cornea is generally better depicted than on the T1-weighed sequences. As the optical or visual axis cannot be obtained from an MR-image[26], it was defined as the line perpendicular to the iris plane and through the center of the lens or pupil (figure 4.7 A).

For the biometry, the axial length of the eye was obtained using the Lenstar LS900 (eyesuite biometry V2.7.1, Haag-Streit diagnostics, Koeniz, Bern). The measurement was performed by an optometrist. To determine the validity of the ocular biometry measurements for patients with UM, three different aspects were evaluated. During these evalua-tions, the observer with 9 years' experience in ocular modeling was blinded for the MR-based eye length measurement. Firstly, the extended outputs of the Lenstar were assessed for signs of an unreliable measurement, including a larger than 0.3mm axial length difference between both eyes[23] or multiple retinal reflections in the original interferometry data. Secondly, the iris decentration, in both the horizontal and vertical direction, was compared to a group of 24 pseu-dophakic controls[25], as an objective test of whether the measurement was per-

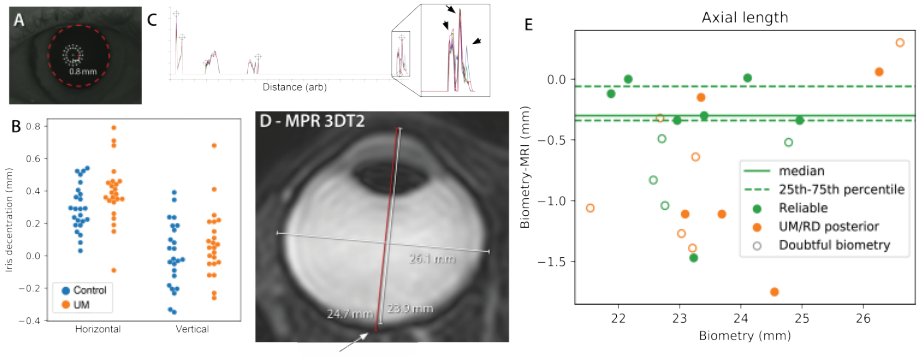

Figure 4.7: Evaluation of the optical biometry and MR-based axial length determination. (A) Pupillometric image of an UM patient, showing a relatively large decentration of 0.8 mm between the iris center (red dashed line) and the line of sight (middle bright spot) along which the axial measurement was performed. (B) Horizontal and vertical decentration of the pseudophakic controls (blue) and UM patients (orange). Five UM patients had a larger decentration than all control subjects, suggesting they did not use the fovea for fixation. (C) Partial Coherence Interferometry data of one of the UM patients, used by the biometer to obtain the axial length. On the posterior side multiple reflections of the laser were detected (arrows), resulting in an inaccurate length measurement. (D) The original MRI-based eye length measurement of the patient that showed a 0.8 mm larger eye length than on biometry. A re-evaluation of the MRI showed that part of the sclera was erroneously included in the MR-measurement, causing the overesti-mation of the eye length with 0.8 mm. (E) Difference between MRI-based and biometry-based eye length measurements. In patients with a doubtful biometry data an average 0.7mm shorter eye was measured with the biometry, while in patients with a UM or retinal detachment (RD) in the posterior pole on average 0.8mm shorter eyes were found. For the remaining patients, there was generally a good agreement between both techniques, except for one patient where part of the sclera was included in the MRI measurement (D).

formed along the visual axis. Finally, the presence of tumor or retinal detachment in the posterior pole was scored on MRI and fundoscopy.

The difference between the MRI and biometry based axial length was calculated for all patients. Patients with a difference larger than 0.5mm without one of the signs of a potentially invalid biometry measurement were evaluated in a multidisciplinary setting. Finally, the axial length on MRI was compared with the biometry results of the affected and contralateral eye.

4.6.3 Results

In one of the PT patients an intraocular haemorrhage prevented the optical biometry measurement and was there-fore excluded from this analysis. For the control group, the horizontal iris decentration, figure 4.7 A, was between 0.03 mm and 0.54 mm in the temporal direction, while the vertical decentration was between 0.35 mm in the inferior and 0.39 mm in the superior direction. 5 UM patients had larger iris decentration than the control group, suggesting that they stared at the fixation target with their peripheral retina instead of the macula. For five patients, a larger than 0.3 mm difference in axial length between both eyes was observed, while in two additional patients the original interferometry data was scored as unreliable, figure 4.7 C. Combining these three separate evaluations of the biometric data marked 10 of the 22 performed biometry measurements doubtful. When the presence of the RD or tumor in the posterior pole was added as a sign of a potential erroneous optical axial length measurement, an additional 5 biometry measurements were marked as potentially erroneous. As a result, in 68% of the UM patients there were signs that the optical biometry could have resulted in an erroneous axial length measurement.

For almost all patients the MRI reported a longer axial length than the biometry, with a mean difference of -0.63 mm (SD:0.56 mm), figure 4.7 E. When the doubtful biometry measures were excluded from the analysis, six of the seven pa-tients show a difference of less than 0.4mm compared to the MR measurement (mean difference: -0.37 mm). In one of these patients, however, a larger discrepancy of 1.5 mm was found. A re-evaluation of the MR-images of this patient showed that a part of sclera was included in the axial length measurement, figure 4.7 D, resulting in a 0.8 mm overesti-mation of the axial length. For the patients where the biometry data shows signs of a doubtful measurement, on average a 0.73 mm shorter axial length was measured compared to MRI (range -0.30 mm, 1.39 mm), while for the patients with RD or tumor in the posterior pole on average a 0.82 mm difference was found (range -0.30 mm to 1.75 mm). In all five patients with a difference $>$0.3 mm between the affected and the contralateral eye the difference between MRI and biom-etry was reduced when the axial length of the contralateral eye was used (average absolute difference affected eye 0.8 mm and contralateral 0.4 mm). In 2/5 cases the difference between MRI and biometry of the contralateral eye was $>$ 0.5 mm.

After re-evaluation of one incorrect MRI measurement (figure 4.7 D) the axial length between the affected and contrala-teral eye showed an average absolute difference

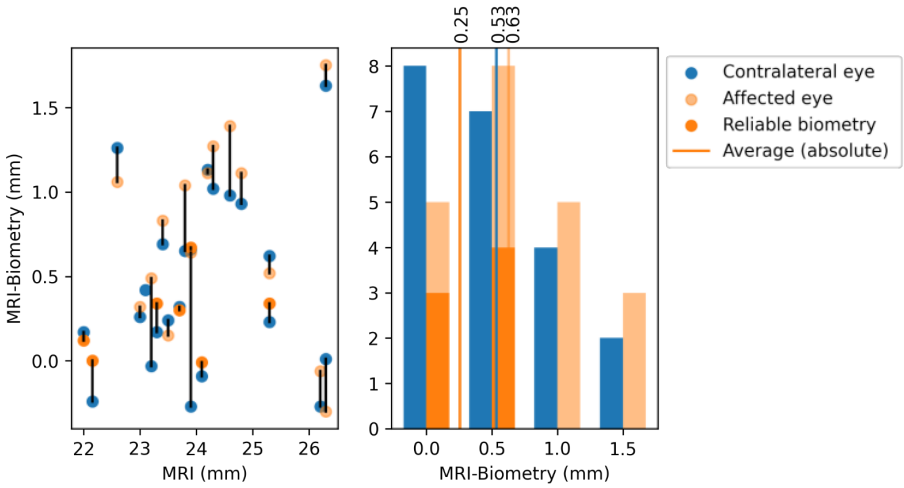

Figure 4.8: Comparison of the optical biometry of the affected and contralateral eye with the MR-based axial length of the affected eye. The difference between MRI and biometry of the affected eye was higher than the contralateral eye (average absolute difference of 0.63 (light orange) vs 0.53 mm (blue)) with less outliers (B). However, for reliable biometry of the affected eye the average absolute difference was much lower (0.25 mm, dark orange).

between MRI of 0.63 mm and was reduced to 0.25 mm for only the reli-able biometry. The average absolute difference between MRI and the contralateral eye was 0.53 mm (figure 4.8).

4.6.4 Discussion

In the current TPS for ocular-PT, a generic eye model is scaled to the patients' eye size using the axial length. Optical biometry is currently the most commonly used method to determine the axial length. Optical biometry appeared to be less reliable in the majority of the UM patients. The biometer, for example, assumes that the laser is reflected at the inner limiting membrane of the retina. For patients with an intraocular mass, however, the mass or associated retinal detach-ment, could also reflect the light, resulting an apparent shorter eye. Moreover, instructing the subject to stare at a fixation light normally guarantees that the eye length is measured from the cornea to the fovea. However, when the central vision is affected by the tumor patients tends to focus with their peripheral retina. As a result, the obtained axial length meas-urement does not correspond to the eye length. In almost half of the patients the UM or associated retinal detachment was present in the posterior pole, which could result in an apparent shorter eye on biometry.

In 22% of the patients a relatively large iris decentration was found, suggesting that these patients focus with their peripheral retina instead of the fovea, resulting in an erroneous measurement. Although these large percentages of po-tentially erroneous eye length measurements are not completely unexpected given the method in which

the eye length was obtained, the overall 0.7mm too short eye for these patients, could result in a considerable geometrical mismatch in the location of the organs at risk, such as the macula. In clinical practice it is recognized that axial length measures can be inaccurate due to tumor presence therefore often the axial length of the contralateral eye is used. In our cohort of patients, use of the contralateral eye would result in an average absolute difference of 0.5 mm compared to the MRI measurement which is less than 0.6 mm in all affected eyes. However, the average absolute difference in the affected eye when there is reliable biometry is 0.3 mm. Although the axial length of the contralateral eye could serve as an alternative when no MR-data is available, we consider the MR-based axial length measurement more accurate, especially as more than 0.3 mm differences in axial length between both eyes was reported in 24% of the general population[41].

Although smaller differences, generally below 0.4 mm, were found in the patients with a reliable biometry, the optical measurements of these patients was still affected by an inherent bias of the current PCI methods. The eye length is measured as an optical path length which is converted to millimeters assuming a refractive index of 1.35[47]. Howev-er, as the different elements of the eye have a different refractive index[48], this average refractive index should be eye length dependent. However, since the current biometers do not correct for this effect, the used measures have an eye length dependent systematic bias of up to 0.4 mm[49]. In cataract surgery, these factors are corrected for within the IOL formulas[49], but this is currently not done in PT planning.

Although optical biometry is currently the most used technique to measure the axial length[50,51], ultrasonic biom-etry is also used in some PT-centers. Although ultrasonic biometry, which was in the past only technique clinically available to measure axial length, is not influenced by differences in refractive index, it would still be susceptible the presences of ocular pathology in the posterior pole. Moreover, ultrasonic biometry is highly dependent on the position-ing of the ultrasound transducer, making it less accurate than optical biometry[52,53].

Considering these limitations of optical biometry, we conclude MRI results in a more accurate axial length meas-urement in UM patients, although the precision of the performed MRI-measurements was limited by absence of a visible macula and the voxel-size. This last limitation could however be improved by an automatic method, which in healthy eyes showed a good reproducibility of 0.1 mm[26].

4.7 Appendix - Ray tracing simulations

4.7.1 Introduction and methods

To assess the size and localization of the shadow which an anterior tumor could create during transillumination, op-tical ray-tracing simulations were performed, in OpticStudio (version 20.3.2, Zemax LCC), using a personalized eye model The optical parameters of this model were based on the Escudero-Sanz eye model,[48]but the retinal shape was based on the MR-images and biometric data. Additionally, intra- and periocular structures representing the tumor, tantalum markers and optic nerve were added. The axial length was obtained from a biometry measurement (Lenstar LS900, Haag-Streit), and the shape and location of the retina, tumor, tantalum markers and optic nerve were obtained from 3DT1 weighted MRI-scan using MevisLab (version 3.0.2, MeVis Medical Solutions AG, Bremen, Germany). The retinal shape was determined by manually defining an ellipsoid in three orthogonal planes (figure 4.9 A). The position of the tantalum markers was obtained by manually annotating their centers within a 3D viewer (figure 4.9 B). For the tumor, an initial estimation of its boundary was created manually and subsequently used as input for an in-house developed subdivision fitting algorithm to accurately determine the tumor boundary (figure 4.9 C). The shape of the optic nerve was manually delineated. All MR-derived shapes were saved as STL-files and loaded in OpticStudio.

Within OpticStudio, a non-sequential ray-tracing model of the eye, tumor, tantalum markers and optic nerve, was created. The cornea was defined as 2 standard surfaces combined into a compound lens. For the anterior corneal surface, the radius was set to 7.72 mm and the conic constant to -0.26, equal to the model of by Escudero-Sanz et al.[48] Similarly, the radius of the posterior corneal surface was defined to be 6.50 mm with a corneal thickness of 0.55 mm. The anterior chamber was modelled as a standard lens with a thickness of 3.55 mm and an anterior surface that matched the posterior corneal surface. The iris was defined by the combination of an annulus and an annular volume, where the annular volume ensured blockage of peripheral light and the annulus provided a method to vary pupil size. The vitre-ous body was modelled to be slightly larger than the retina, to prevent any refraction at the vitreous-retina interface. The crystalline lens was defined as compound lens with an anterior radius and conic of respectively 10.20 mm and -3.13, posterior radius of -6.00 mm and a central thickness of 4.00 mm.[1] The MR-derived shapes of the retina, tumor, tantalum markers and optic nerve were saved as STL-files and subsequently loaded into OpticStudio. Within OpticStudio, they were set to absorb light. A cross-section of the complete model is shown in figure 4.9 D.

All simulations were performed with a wavelength of 543 nm and the corresponding refractive indices as defined by Escudero-Sanz et al[48]. Two different sets of optical simulations were performed, with each set consisting of simulations with actual pupil diameters of 8.0 and 10.0 mm. The first set of simulations used an elliptical light source, emitting a parallel beam of 107 light rays towards the pupil center. This source was positioned at different locations around the eye, simulation a transillu-

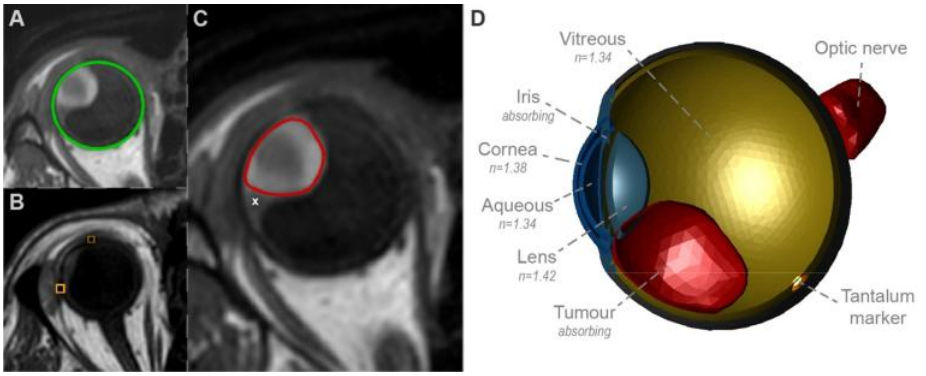

Figure 4.9: Overview of eye model design. (A) Manual segmentation of the retina-sclera (green). (B) Manual annotation of tantalum markers (orange). (C) Automated segmentation of tumor boundary (red). Note that the small, non-enhancing, retinal detachment adjacent to the UM (white x) is not included. (D) Overview of the personalized eye model including all used refractive indices at a wavelength of 543 nm. Structures based on the Escudero-Sanz eye model are shown in blue, structures of which the location and dimensions have personalized in orange and structures that where fully segmented in 3D in red.

mination measurement, and was used to assess under which conditions the tumor would create a shadow. The second set of simulations used a spherically shaped source that encapsulated the complete anteri-or segment of the eye. This source emitted 4*109 rays of light in a Lambertian distribution, ensuring illumination from every angle. This simulation show the part of the sclera which cannot be illuminated and is therefore considered tumor during transpupillary illumination. The complete process of building analyzing the model in OpticStudio was auto-mated using in-house developed software as described previously and the resulting OpticStudio files can be found in the supplementary information.[25]

4.7.2 Results

The simulations of transpupillary illumination measurements show that the tumor blocks part of the light rays, inducing a shadow at the posterior end of the tumor. The smallest incident angle at which all light is blocked by the tumor depends strongly on the pupil size. Increasing the pupil size results in an increase in the maximal incident angle at which light still reaches the retina, which causes a decrease in the size of the casted shadow (figure 4.10 A).

The second set of simulations, in which the part of the retina cannot be illuminated is determined, shows that this part of the retina is substantially larger than the tumor base (figure 4.10 B). Furthermore, these simulations show that, for a pupil of 10 mm, the two posterior tantalum markers where located at the edge of the shadow casted by the tumor instead of at the tumor base.

These optical ray-tracing analyses show the posterior extend of an anterior tumor can be overestimated using transpupillary transillumination and that the amount of over-

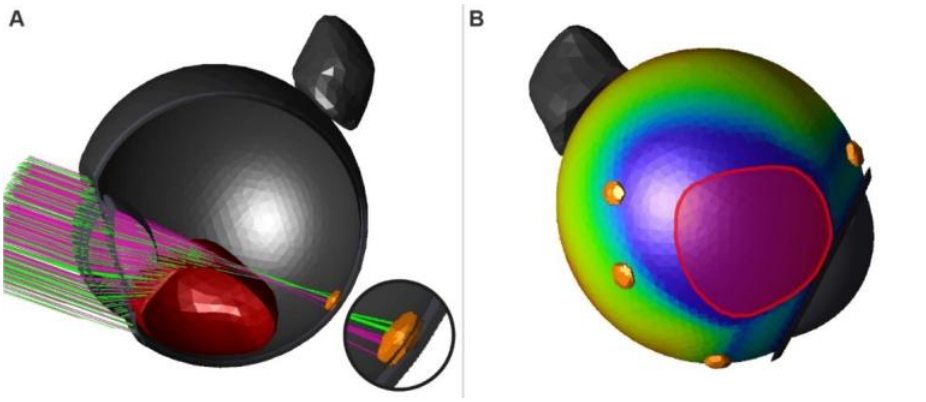

Figure 4.10: Ray tracing simulations of an eye with an intraocular tumor. (A) Ray tracing simulation of a transpupilar illumination with a 8.0 mm pupil (green rays) and 10.0 mm pupil (pink rays) showing that part of the retina cannot be illuminated as the tumor blocks these light rays. The location of the tantalum marker coincides with the location where these rays can reach the retina.. Note that the increase of 2 mm in pupil diameter results in a 1 mm shift of the most anterior limiting rays, decreasing the size of the observed shadow. (B) Ray tracing simulation of the total retinal illumination with the tumor present for a 10.0 mm pupil diameter. The illumination is displayed with a gradient from blue (no illumination) to red (maximum illumination). The tumor (red overlay) obfuscates a large part of the retina. Note that the tantalum markers (orange) are located on the edge of the unilluminated retina rather than at the tumor border.

estimation depends the tumor size and pupil diameter. Although only transpupilar illumination has been simulated, a similar overestimation is expected for transocular illumination as the posterior end of the tumor base cannot be seen through the pupil.

4.8 Appendix - MRI protocols for ocular-PT planning

4.8.1 Diagnostic protocol

The UM protocol used for baseline evaluation and measurements of the tumor and eye geometry was similar to the optimized MRI protocol for UM as described by Ferreira et al.[11] The protocol includes 3D isotropic volumetric scans to assess the tumor and eye geometry, 2D scans to evaluate tumor origin and extension and functional scans to assess the tumor microstructure (Diffusion Weighted Imaging) and perfusion (Dynamic Contrast Enhanced imaging). Com-pared to the protocol of Ferreira, an improved version of the 3D-T1 scans was used with a more efficient k-space sampling (BrainVIEW, Philips Healthcare) to allow for a 66 seconds shorter scan with an increased isotropic resolution of 0.8 mm.

4.8.2 Marker protocol

A dedicated MRI protocol was developed to assess the marker-tumor relation. In order to limit the susceptibility artefacts of the tantalum marker these scans were modified compared to the original diagnostic protocol. As tantalum is paramagnetic, it locally disturbs the homogeneity of the magnetic (B0) field, resulting in a local signal-void and potentially geometric distortions[20]. These effects were minimized through localized shimming and an increased gradient strength of at least 22mT/m. The spatial extend of the resulting signal voids was assessed for the different sequences in a subset of 3 patients.

The protocol started with 3D isotropic T1- and T2-weighted spin echo (SE) scans to allow comparison with the preoperative MRI-images. Additionally, a 3D T1-weighted gradient echo (GE) sequence was performed, as blooming artefact around the markers on these sequences enable a clear localization of the tantalum markers. Subsequently, a multi-slice T1-weighted GE image was acquired through the tumor base (e.g. base scan, main text figure 3D), aiding the correlation between the 3D marker localization on the MRI and the surgical view. Finally, a GE T1-, SE T1- and SE T2-weighted multi slice scan was acquired for each marker (e.g. marker scans) which were planned perpendicular to the base scan to yield the optimal depiction of the marker-tumor relation (figure C1 and main text figure 3D). These GE T1 scans were acquired to aid in the localisation of the marker, while the SE T1 and T2 sequences where acquired to have a minimal susceptibility artefact for the marker-tumor distance measurements. To have an optimal localisation of the hypointense marker, all these sequences were acquired without fat suppression. At the end of the protocol a fat-suppressed T2 was acquired, to screen for post-surgical inflammatory processes behind the globe.

The GE sequences showed significantly larger signal-voids at the location of the markers (3DT1: 5.1$\pm$0.4 mm, 2DT1: 5.3$\pm$0.4 mm) compared to the SE sequences (3DT2: 3.0$\pm$0.4 mm, 2DT2: 3.0$\pm$0.6 mm, $p<0.01$). The 2DT2 scan, used to deter-

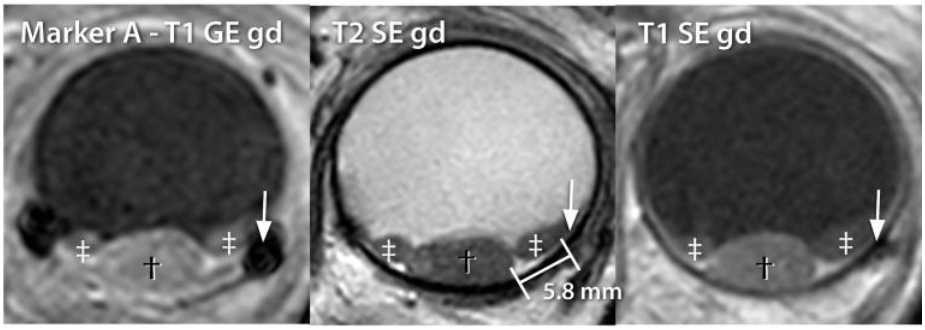

Figure 4.11: Scans to visualize the marker-tumor relation of a UM patient after contrast administration. Retinal detachment (double dagger) can be differentiated from the tumor (dagger) as it does not enhance after contrast administration. For each marker a T1-weighted GE, T2- and T1-weighted SE were acquired. Note that on the T1-weighted gradient echo scan the marker (arrow) appears bigger and is therefore easier localized compared the both spin echo sequences.

mine the marker-tumor distance, showed an overestimation of the marker diameter of approximately 0.5 mm

4.8.3 Improved marker protocol

The marker protocol for the patients included in this study did not include the administration of a contrast agent. In some patients the T2- and T1-weigthed multi slice images alone did not provide sufficient information to differentiate the tumor from retinal detachment. For these patients, the presurgical MRIs, which included contrast enhanced T1-weighted images, were included in the evaluation. The combing of the MR-images of both examinations, however, proved to be time consuming and could potentially introduce uncertainties when the retinal detachment changed between the pre-operative and marker scan. We therefore recently started to perform the marker-tumor scans after ad-ministration of a contrast agent (gd-DOTA, DOTAREM, Guerbet, Roissy CdG Cedex, France) which helped in the differentiation between tumor and retinal detachment[11], figure 4.11. Furthermore, we started to measure the MT-distance to the centre of the marker instead of the marker edge to avoid underestimation of the distance due to blooming as on the SE-sequences this signal void was exceeding the actual marker by approximately 0.3 mm.

4.9 Appendix - Detailed comparison results

In this supplement the differences and potential source of the discrepancies between conventional and MRI measurements are reported on a patient level.

4.9.1 Eye geometry

For almost all patients MRI reported a longer axial length than biometry, with a mean difference of -0.63 mm (SD: 0.56 mm), figure 4.12 B. In one of the UM patients a vitreous haemorrhage prevented optical biometry measurement. This patient was therefore excluded from this analysis. In five patients a large iris decentration was observed and in five patients a larger than 0.3mm difference in axial length between both eyes was observed and in two multiple reflections were present in the biometry data. As in some patients multiple of these observations were present, in total ten out of 22 performed biometry measurements were marked as unreliable (figure 4.12 and supplement A). Five additional measurements were marked as potentially unreliable as patients had UM or RD in the posterior pole. Six out of seven remaining patients show a difference of less than 0.4 mm compared to the MR measurement (mean difference: 0.18 mm). In one of these patients, however, a discrepancy exceeding 1.5 mm was found. A re-evaluation of the MR-images of this patient showed that part of sclera was included in the axial length measurement, figure 4.12 C, resulting in a 1.1 mm overestimation of the axial length. For patients in whom biometry data showed signs of a doubtful measurement, the measured axial length was on average 0.73 mm shorter measured compared to MRI (range -0.30 mm, 1.39 mm). Additionally, for patients with RD or a tumor localised at the posterior pole, this measured axial length was on average a 0.82 mm shorter compared to MRI (range -0.30 mm to 1.75 mm)

4.9.2 Tumor geometry

The average prominence on MRI was 8.0 mm and on US 7.9 mm; for UM with a prominence below 7 mm the US measurements were generally larger compared to MRI, figure 4.13. In UM with a prominence exceeding 7 mm US measurements were smaller in most cases. The difference between all 23 MRI and US based tumor prominence measurements ranged from -2.3 mm to 0.9 mm with an average absolute difference of 0.6 mm, figure 4.13 A. When potentially inaccurate US measurements were excluded, a smaller range of differences was found (from -0.9 mm to 0.9 mm) although, the absolute mean distance of 0.5 mm remained similar.

For 14 patients with reliable US, 4 prominence measurements differed more than 0.5 mm between both imaging modalities and were evaluated separately. One of these tumors was oriented obliquely in the eye, resulting in a different direction of the prominence measurement between both modalities, figure 4.14 A. In one patient, tumor prominence was measured on T2, instead of contrast enhanced T1. A retrospective evaluation of post-contrast 3D T1 showed a slightly more prominent tumor of 4.7 mm which was comparable to the US-based measurement of 4.5 mm.

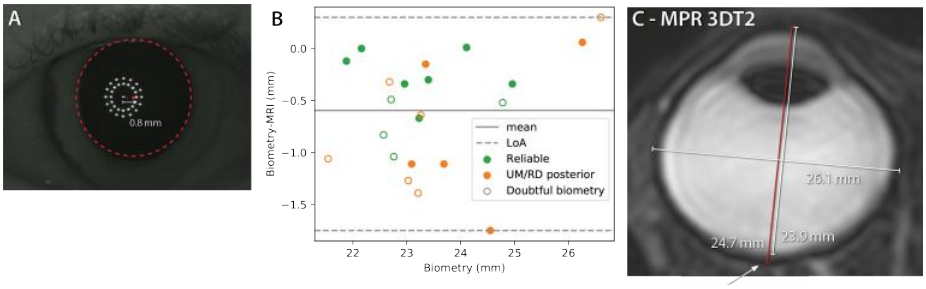

Figure 4.12: Evaluation of the optical biometry and MR-based axial length determination. (A) Pupillometric image of a UM patient, showing a relatively large decentration of 0.8 mm between the iris centre (red dashed line) and the line of sight (middle bright spot) along which the axial measurement was performed. (B) Difference between MRI-based and biometry-based eye length measurements. In patients with a doubtful biometry (open dots) an average 0.7 mm shorter eye was measured with the biometry, while in patients with a UM or retinal detachment (RD) in the posterior pole (orange dots) on average 0.8 mm shorter measurements were found. For the remaining patients (filled green dots), there was generally a good agreement between both techniques, except for one patient where part of the sclera was included in the MRI measurement (C). (C) The original MRI-based eye length measurement (red) of the patient that showed a 1.4 mm larger eye length than on biometry. A re-evaluation of the MRI showed that part of the sclera (arrow) was erroneously included in the MR-measurement, causing the overestimation of the eye length with 0.8 mm.

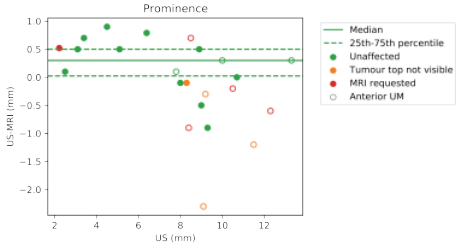

Figure 4.13: Comparison between the US-based and MR-based prominence measurement. Anterior tumors are depicted with open markers. The colours indicate possible inaccuracies in the ultrasound measurement. For 5 patients (red), an MRI was requested clinically due to doubts on the accuracy of the US measurements. Additionally, 7 US measurements were scored as potentially inaccurate (orange), as they did not show the complete tumor in the FOV. Notably, for 10 of these 12 patients the tumor was located anteriorly (open markers). For patients with reliable US measurements, a mean absolute difference of 0.5 mm was found between the MRI-based and US-based prominence measurement (range -0.9 mm to 0.9 mm). Overall, the largest differences were observed in anterior UM.

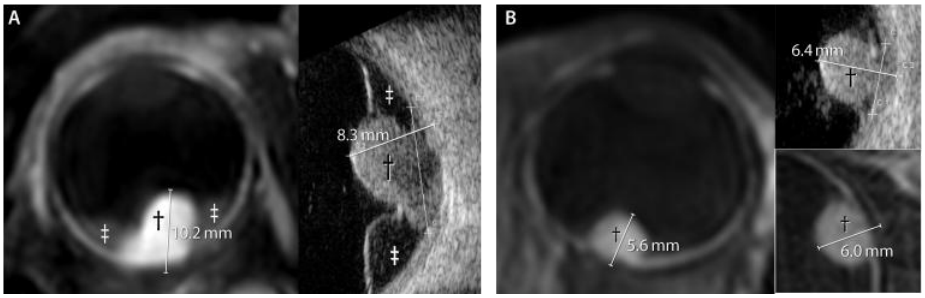

Figure 4.14: Examples of differences between US and MRI measurements The tumor is marked with a dagger and the retinal detachment with a double dagger. (A) Example patient where the 2 mm difference prominence between both imaging modalities was attributed to an asymmetric tumor geometry. This shape caused a difference in axis along which the measurement was performed between the MRI (left) and US (right). This also resulted in a 3 mm difference in basal diameter measurement. (B) Papillary located UM, in which the sclera could not accurately be included in the measurement on the 3D contrast enhanced T1 MR-images (left). Retrospectively, for this specific patient a more accurate measurement could have been obtained on the MS T1 (lower right), showing a slightly more prominent tumor.

In the third patient with a relatively large difference in tumor prominence between both modalities, the tumor was located on the papilla, figure D3 B. For this patient, the US showed a prominence of 6.5 mm, while on the MR-images 5.6 mm was measured, with the note that the sclera could not well be discriminated due to the papillary localisation. A retrospective evaluation of the 2D contrast enhanced T1 images, which have a higher in-plane resolution and therefore allowed for a better discrimination of the sclera, showed a tumor prominence of 6.0 mm for this patient. Finally, the fourth patient had a flat UM of which the radiological report noted that its extension could not clearly be visualized on the MR-images.

The largest basal diameter was in most cases smaller on MRI compared to US with an average absolute difference of 1.4mm. Compared to the prominence measurements, larger differences were found in basal diameters ranging from -2.7 mm to 3.5 mm , figure 4.15 A. The largest differences were found in the five patients where the ophthalmologist requested an MRI due to doubts on accuracy of the US-based measurements. In four of the five patients the MRI measurement was larger. In these 5 patients an average absolute difference of 2.2 mm was found. Additionally, for four of the seven patients where the complete tumor base was not visualized in the US field of view differences exceeding 1 mm were ob-served, with a maximum of 1.9 mm. The basal diameter of one flat UM could not accurately be determined on the MR-images.

For the 10 patients with both reliable MRI and US LBD measurements, an average absolute difference of 1.2 mm was found, with the difference exceeding 1 mm in 5 patients. Three of these patients had a flat UM, and here MRI re-ported a 1.2 mm to 1.4 mm larger basal diameter. In one patient the MRI showed a hyperintense region adjacent to the tumor on T1, figure 4.16. This region showed strong enhancement

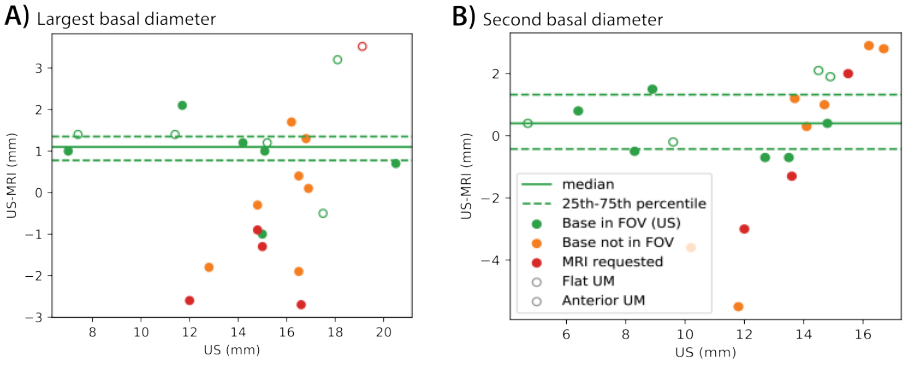

Figure 4.15: Comparison between the US-based and MR-based tumor size measurements in terms of largest and second basal diameter. (A,B) For the patients with an reliable US measurement, an average absolute difference between both techniques of 1.2 mm for the largest and 1.6 mm for the second basal diameter was found. The majority of the unreliable US measurements were for UM basal diameters exceeding 14 mm.

after contrast administration, it was considered choroid and therefore not included in the basal diameter, resulting in a 2.1 mm smaller measurement on MRI. Finally, in one patient a thickened choroid directly adjacent to the tumor was not included in the basal diameter, while it appeared to be included on the US-measurement.

The comparison of measurement of the second basal diameter showed similar results as the largest basal diameter with an average absolute difference of 1.6 mm with a larger range of differences from -5.5 mm to 2.9 mm, figure D4 B.

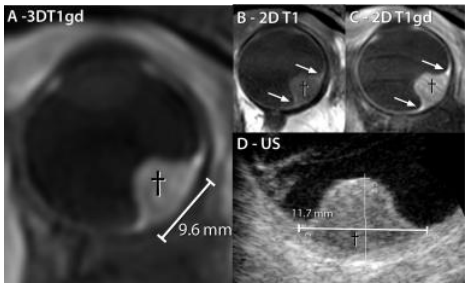

Figure 4.16: Patient with 2 mm difference in largest basal diameter. On the contrast enhanced 3D T1 (A) a more hyperintense region adjacent to the tumor base was seen, which was more clearly visible on the pre- and postcontrast MS T1 (B,C, arrows). This was considered enhancing choroid and not included in the tumor base for the MRI measurement. This part was, however, included in base for the US measurement (D), resulting in the larger basal diameters.

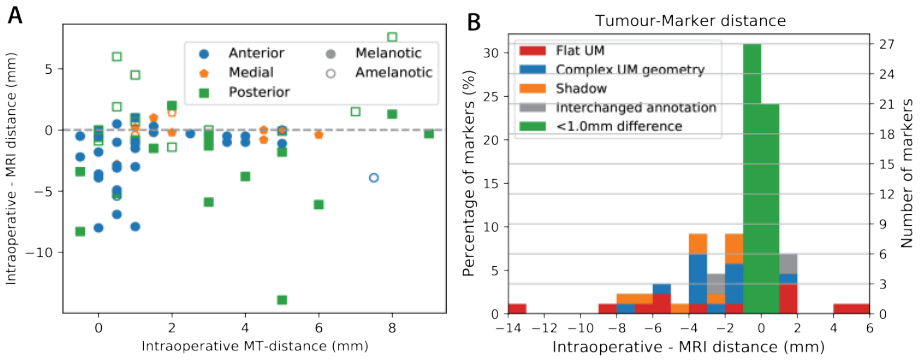

Figure 4.17: Comparison between the intraoperative and MR-based marker-tumor distance measurements. In 55% of the markers a difference of less than 1 mm was observed (B, green). The largest differences, up to 14 mm, were observed in flat melanoma (red). For 25% markers the difference was attributed to a complex tumor geometry (blue) or shadow cast by the tumor (orange).

4.9.3 Marker-tumor distances

In the majority of the patients four markers were used. In one patient the post-operative MRI was not performed because the flat tumor could not accurately be delineated on the pre-operative MR-images. Finally, in one patient 1 of the MT-distances could not be measured intraoperatively.

On average the MRI reported 1.2 mm larger MT-distances compared to the intra-operative measurements, figure D6 A. For 39 of the 87 (45%) evaluated markers, the difference between both measurements was exceeding 1 mm (figure 4.17 B). MRI showed a larger MT-distance for the majority of these markers (n=30). The multidisciplinary evaluation of markers with a difference exceeding 1 mm revealed four reasons for these differences.

First, largest differences were observed in flat UM where 13 of the 18 markers showed difference exceeding 1 mm (figure 4.17 B, 4.18 AB). Since the extend of a flat melanoma was difficult to assess on MRI the intraoperative measurements were considered more reliable. A notable exception was an unpigmented flat UM, where the intraoperative measurement indicated that three markers were located on the border of the tumor. The MR-images, however, convincingly showed the tumor extended further than these markers, figure 4.18 B.

Additionally, in 13 markers the difference was attributed to a complex marker-tumor relation (figure 4.19, 4.20A-C). Eleven markers involved tumors that did not have a classical dome shape. In these more complex shaped tumors, which for example are oriented obliquely to the sclera, the MT-distance could not easily be captured in a simple one-dimensional distance measurement, figure 4.20 A-C. The MT-distance defined as the distance from the marker to the tumor base (figure 4.20 B, 3.9 mm) is not the smallest distance between the marker and tumor (figure 4.20 B, 1.1 mm). Alternatively the tumor can also be projected onto the sclera and the distance

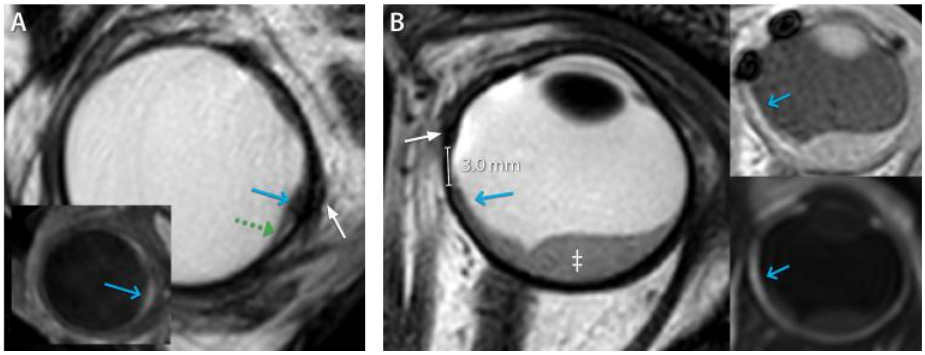

Figure 4.18: Comparison between the intraoperative and MR-based marker-tumor distance measurements. In 55% of the markers a difference of less than 1 mm was observed (B, green). The largest differences, up to 14 mm, were observed in flat melanoma (red). For 25% markers the difference was attributed to a complex tumor geometry (blue) or shadow cast by the tumor (orange).

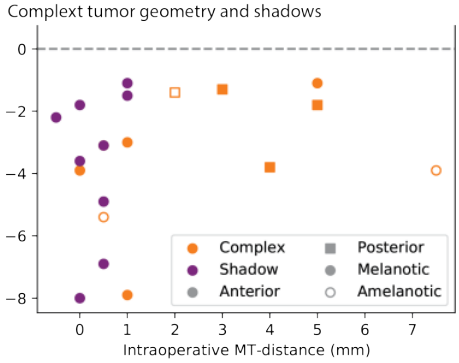

Figure 4.19: Overview of the 13 markers where the difference between the MRI and intraoperative marker-tumor distance measurement was attributed to a complex tumor geometry (orange) and 9 markers where the difference was attributed to the shadow cast by the tumor (purple).

between this projection and the marker can be measured (figure 4.20 B, 0 mm). The other two markers were positioned relatively far from the tumor, exceeding 7 mm on the intraoperative measurement. With such large distances, the intraoperative measurement is less accurate as the surrounding anatomy, such as the insertion of the muscle, interferes with the measurement. Moreover, the MT-distance defined as the distance from the marker to the tumor base (figure 4.20 C, 5.9 mm) is not always the smallest distance between the marker and tumor (figure 4.20 C, 5.0 mm). For distant markers and mushroom shaped tumors the MT-distance could not easily be captured in a simple one-dimensional distance measurement which possibly accounts for the observed differences between both measurements.

Furthermore, a shadow cast by an anterior tumor during transillumination caused an overestimation of the tumor extent. This resulted in an average difference of 3.7 mm for nine posteriorly located markers (max 8.0 mm) in six patients, figure

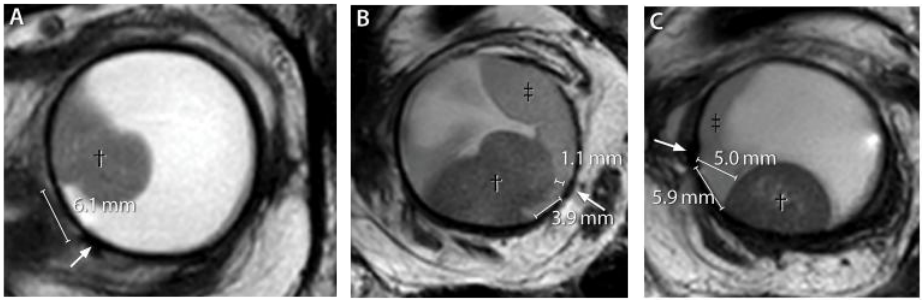

Figure 4.20: (A,B) The MRI shows a 6.1 mm (A) and 3.9 mm (B) distance between the marker (arrow) and the tumor base for these mushroom shaped UM. These complex tumor-retina relations, can however not easily be captured in a single distance measurement. (C) When a marker was positioned relatively distant from the tumor, the shortest distance to the tumor might not be to the tumor base, which was measured intraoperatively. In this figure the tumor was marked with a dagger and the retinal detachment with a double dagger.

4.19. Personalized optical ray-tracing simulations, figure 4.21 C&D, confirmed this shadow and showed that for this specific patient the shadow extended until the location of the markers for this specific patient matching the intraoperative marker-tumor measurements.

Finally, in two patients the intraoperative annotation of two markers appeared to have been interchanged. In both cases, one of the anteriorly located markers was located directly adjacent to the tumor, while the marker on the opposite side was located 2 mm from the tumor. The MR-images showed a similar but mirrored configuration of the anterior markers.

4.10 References

[1] M. G. Jaarsma-Coes *et al.*, "Comparison of mri-based and conventional measurements for proton beam therapy of uveal melanoma," *Ophthalmology Retina*, 2022, ISSN: 2468-6530. DOI: https://doi.org/10.1016/j.oret.2022.06.019. [Online]. Available: https://www.sciencedirect.com/science/article/pii/S2468653022003396.

[2] M. E. Aronow, A. K. Topham, and A. D. Singh, "Uveal melanoma: 5-year update on incidence, treatment, and survival (seer 1973-2013)," *Ocular oncology and pathology*, vol. 4, no. 3, pp. 145–151, Apr. 2018, ISSN: 2296-4681. DOI: 10.1159/000480640. [Online]. Available: https://pubmed.ncbi.nlm.nih.gov/29765944.

[3] IKNL, *NKR cijfers*. [Online]. Available: https://iknl.nl/nkr-cijfers.

[4] K. K. Mishra and I. K. Daftari, "Proton therapy for the management of uveal melanoma and other ocular tumors," *Chinese Clinical Oncology*, 2016, ISSN: 23043873. DOI: 10.21037/cco.2016.07.06.

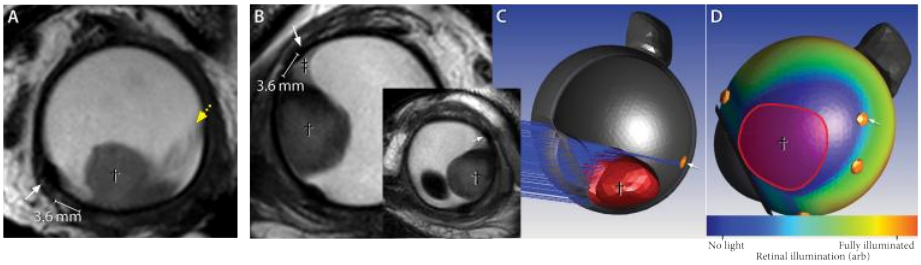

Figure 4.21: The shadow cast by the tumor, can result in an overestimation of the tumor dimensions during transillumination. (A) Example of one of the patients where both the marker and the iris (yellow arrow) are visualized. (B-D) For one of these patients, the tumor shadow during transillumination was simulated using optical ray-tracing. (B) On MRI a marker-tumor distance of 3.6 mm was measured. The inset, showing the marker and eye in a different plane, shows that the top of the tumor obstructs an optical assessment of the posterior tumor base. The optical simulations (C,D) show that for a light beam reaching the posterior side of the tumor, almost all light rays were absorbed by either the pupil or tumor, creating a shadow which extends to the marker (arrow). When light rays from all possible directions were combined, the outside view of the eye shows how the unilluminated retina extends to both markers, resulting in an overestimation of the tumor base.

[5] J. Hrbacek *et al.*, "Practice Patterns Analysis of Ocular Proton Therapy Centers: The International OPTIC Survey," *International Journal of Radiation Oncology Biology Physics*, vol. 95, no. 1, pp. 336–343, 2016, ISSN: 1879355X. DOI: 10.1016/j.ijrobp.2016.01.040.

[6] E. Egger *et al.*, "Maximizing local tumor control and survival after proton beam radiotherapy of uveal melanoma.," *International journal of radiation oncology, biology, physics*, vol. 51, no. 1, pp. 138–47, 2001, ISSN: 0360-3016. DOI: 10.1016/S0360-3016(01)01560-7. [Online]. Available: http://www.ncbi.nlm.nih.gov/pubmed/11516863.

[7] B. Damato, A. Kacperek, M. Chopra, I. R. Campbell, and R. D. Errington, "Proton beam radiotherapy of choroidal melanoma: The Liverpool-Clatterbridge experience," *International Journal of Radiation Oncology Biology Physics*, vol. 62.5, pp. 1405–1411, 2005, ISSN: 03603016. DOI: 10.1016/j.ijrobp.2005.01.016.

[8] T. D. Papakostas, A. M. Lane, M. Morrison, E. S. Gragoudas, and I. K. Kim, "Long-term Outcomes After Proton Beam Irradiation in Patients With Large Choroidal Melanomas," *JAMA Ophthalmology*, vol. 135, no. 11, pp. 1191–1196, Nov. 2017, ISSN: 2168-6165. DOI: 10.1001/jamaophthalmol.2017.3805. [Online]. Available: https://doi.org/10.1001/jamaophthalmol.2017.3805.

[9] M. J. Sikuade, S. Salvi, P. A. Rundle, D. G. Errington, A. Kacperek, and I. G. Rennie, "Outcomes of treatment with stereotactic radiosurgery or proton beam therapy for choroidal melanoma.," *Eye (London, England)*, vol. 29, no. 9, pp. 1194–1198, 2015, ISSN: 1476-5454 (Electronic). DOI: 10.1038/ey

e.2015.109. [Online]. Available: http://dx.doi.org/10.1038/eye.2015.109.

[10] A. Russo *et al.*, "Diffusion-weighted magnetic resonance imaging and ultrasound evaluation of choroidal melanomas after proton-beam therapy," *Radiol Med*, vol. 120, no. 7, pp. 634–40, 2015, ISSN: 0033-8362. DOI: 10.1007/s11547-015-0509-1.

[11] T. A. Ferreira, L. G. Fonk, M. G. Jaarsma-Coes, G. G. van Haren, M. Marinkovic, and J. W. M. Beenakker, "MRI of uveal melanoma," *Cancers*, vol. 11, no. 3, pp. 1–20, 2019, ISSN: 20726694. DOI: 10.3390/cancers11030377.

[12] T. Niendorf *et al.*, *Ophthalmic Magnetic Resonance Imaging: Where Are We (Heading To)?* 2021. DOI: 10.1080/02713683.2021.1874021.

[13] J.-W. M. Beenakker *et al.*, "Outcome measures of new technologies in uveal melanoma: Review from the european vision institute special interest focus group meeting," *Ophthalmic Research*, 2022.

[14] E. Fleury *et al.*, "Improving organs-at-risk sparing for choroidal melanoma patients: A ct-based two-beam strategy in ocular proton therapy with a dedicated eyeline," *Radiotherapy and Oncology*, vol. 171, pp. 173–181, Jun. 2022, ISSN: 0167-8140. DOI: 10.1016/j.radonc.2022.04.021. [Online]. Available: https://doi.org/10.1016/j.radonc.2022.04.021.

[15] M. K. Hassan *et al.*, "An automatic framework to create patient-specific eye models from 3D MR-images for treatment selection in patients with uveal melanoma," *Advances in Radiation Oncology*, p. 100 697, 2021, ISSN: 2452-1094. DOI: https://doi.org/10.1016/j.adro.2021.100697. [Online]. Available: https://www.sciencedirect.com/science/article/pii/S2452109421000555.

[16] T. A. Ferreira *et al.*, "MR imaging characteristics of uveal melanoma with histopathological validation," *Neuroradiology*, vol. epub, 2021. DOI: https://doi.org/10.1007/s00234-021-02825-5.

[17] J. W. M. Beenakker *et al.*, "Clinical evaluation of ultra-high-field MRI for three-dimensional visualisation of tumour size in uveal melanoma patients, with direct relevance to treatment planning," *Magnetic Resonance Materials in Physics, Biology and Medicine*, vol. 29, no. 3, pp. 571–577, 2016, ISSN: 13528661. DOI: 10.1007/s10334-016-0529-4.

[18] L. van Vught, D. P. Shamonin, G. P. M. Luyten, B. C. Stoel, and J.-W. M. Beenakker, "MRI-based 3D retinal shape determination," eng, *BMJ open ophthalmology*, vol. 6, no. 1, e000855–e000855, Nov. 2021, ISSN: 2397-3269. DOI: 10.1136/bmjophth-2021-000855. [Online]. Available: https://pubmed.ncbi.nlm.nih.gov/34901465%20https://www.ncbi.nlm.nih.gov/pmc/articles/PMC8611437/.

[19] S. J. Wiseman *et al.*, "Measuring axial length of the eye from magnetic resonance brain imaging," *BMC Ophthalmology*, vol. 22, no. 1, p. 54, 2022, ISSN: 1471-2415. DOI: 10.1186/s12886-022-02289-y. [Online]. Available: https://doi.org/10.1186/s12886-022-02289-y.

[20] E. Oberacker *et al.*, "Magnetic resonance safety and compatibility of tantalum markers used in proton beam therapy for intraocular tumors: A 7.0 Tesla study," *Magnetic Resonance in Medicine*, vol. 78, no. 4, pp. 1533–1546, 2017, ISSN: 15222594. DOI: 10.1002/mrm.26534.

[21] L. Bergman, B. Nilsson, G. Lundell, M. Lundell, and S. Seregard, "Ruthenium Brachytherapy for Uveal Melanoma, 1979–2003: Survival and Functional Outcomes in the Swedish Population," *Ophthalmology*, vol. 112, no. 5, pp. 834–840, 2005, ISSN: 0161-6420. DOI: https://doi.org/10.1016/j.ophtha.2004.11.038. [Online]. Available: https://www.sciencedirect.com/science/article/pii/S0161642004019001.

[22] M. Marinkovic *et al.*, "Ruthenium-106 brachytherapy for choroidal melanoma without transpupillary thermotherapy: Similar efficacy with improved visual outcome," *European Journal of Cancer*, vol. 68, pp. 106–113, Nov. 2016, ISSN: 0959-8049. DOI: 10.1016/j.ejca.2016.09.009. [Online]. Available: https://doi.org/10.1016/j.ejca.2016.09.009.

[23] Haag-Streit Diagnostics, *Instructions for use Biometer Lenstar LS 900*, 2014. [Online]. Available: https://www.doctor-hill.com/physicians/docs/Lenstar-User-Manual.pdf (visited on 02/26/2021).

[24] L. van Vught, C. E. Dekker, B. C. Stoel, G. P. M. Luyten, and J.-W. M. Beenakker, "Evaluation of intraocular lens position and retinal shape in negative dysphotopsia using high-resolution magnetic resonance imaging," *Journal of Cataract & Refractive Surgery*, vol. 47, no. 8, 2021, ISSN: 0886-3350. [Online]. Available: https://journals.lww.com/jcrs/Fulltext/2021/08000/Evaluation_of_intraocular_lens_position_and.10.aspx.

[25] L. van Vught, G. P. M. Luyten, and J.-W. M. Beenakker, "Distinct differences in anterior chamber configuration and peripheral aberrations in negative dysphotopsia," *Journal of Cataract & Refractive Surgery*, vol. 46, no. 7, 2020, ISSN: 0886-3350. [Online]. Available: https://journals.lww.com/jcrs/Fulltext/2020/07000/Distinct_differences_in_anterior_chamber.13.aspx.

[26] J.-W. M. Beenakker, D. P. Shamonin, A. G. Webb, G. P. M. Luyten, and B. C. Stoel, "Automated Retinal Topographic Maps Measured With Magnetic Resonance Imaging," *Investigative Ophthalmology & Visual Science*, vol. 56, no. 2, pp. 1033–1039, Feb. 2015, ISSN: 1552-5783. DOI: 10.1167/iovs.14-15161. [Online]. Available: https://doi.org/10.1167/iovs.14-15161.

[27] E. D. Baron, M. Di Nicola, and C. L. Shields, *Updated ajcc classification for posterior uveal melanoma: A case example of a patient with choroidal melanoma is discussed in light of the latest edition of this cancer staging manual*, 2018.

[28] I. k. Daftari, E. Aghaian, J. M. O'Brien, W. Dillon, and T. L. Phillips, "3D MRI-based tumor delineation of ocular melanoma and its comparison with conventional techniques," *Medical Physics*, vol. 32, no. 11, pp. 3355–3362,

Nov. 2005, ISSN: 0094-2405. DOI: https://doi.org/10.1118/1.2068927. [Online]. Available: https://doi.org/10.1118/1.2068927.

[29] S. Marnitz *et al.*, "Proton Therapy of Uveal Melanomas," *Strahlentherapie und Onkologie*, vol. 182, no. 7, pp. 395–399, 2006, ISSN: 1439-099X. DOI: 10.1007/s00066-006-1512-1. [Online]. Available: https://doi.org/10.1007/s00066-006-1512-1.

[30] R. Via *et al.*, "Potential and pitfalls of 1.5T MRI imaging for target volume definition in ocular proton therapy," *Radiotherapy and Oncology*, vol. 154, pp. 53–59, 2021, ISSN: 0167-8140. DOI: https://doi.org/10.1016/j.radonc.2020.08.023. [Online]. Available: https://www.sciencedirect.com/science/article/pii/S0167814020307520.

[31] M. G. Jaarsma-Coes *et al.*, "Inter-Observer variability in MR-based target volume delineation of uveal melanoma," *[submitted]*,

[32] D. H. Char, S. Kroll, R. D. Stone, R. Harrie, and B. Kerman, "Ultrasonographic measurement of uveal melanoma thickness: Interobserver variability," *British Journal of Ophthalmology*, vol. 74.3, pp. 183–185, 1990, ISSN: 00071161. DOI: 10.1136/bjo.74.3.183.

[33] C. Haritoglou, A. S. Neubauer, H. Herzum, W. R. Freeman, and A. J. Mueller, "Interobserver and intraobserver variability of measurements of uveal melanomas using standardised echography," *British Journal of Ophthalmology*, vol. 86, no. 12, 1390 LP –1394, Dec. 2002. DOI: 10.1136/bjo.86.12.1390. [Online]. Available: http://bjo.bmj.com/content/86/12/1390.abstract.

[34] J. J. Pe'er *et al.*, "Measuring choroidal melanoma basal diameter: using ultrasound vs. a new wide–angle fundus camera," *Investigative Ophthalmology & Visual Science*, vol. 45, no. 13, p. 1223, May 2004, ISSN: 1552-5783.

[35] B. Damato, A. Kacperek, D. Errington, and H. Heimann, "Proton beam radiotherapy of uveal melanoma," *Saudi Journal of Ophthalmology*, vol. 27, no. 3, pp. 151–157, 2013, ISSN: 13194534. DOI: 10.1016/j.sjopt.2013.06.014.

[36] E. Fleury *et al.*, "3D MRI-based treatment planning approach for non-invasive ocular proton therapy," *Medical Physics*, 2020, ISSN: 0094-2405.

[37] K. Pfeiffer, B. Dobler, C. Rethfeldt, W. Schlegel, and R. Bendl, "OCTOPUS: A planning tool for proton therapy of eye tumours," in *Physica Medica*, 2001. DOI: 10.1007/978-3-642-59758-9_124.

[38] H.-G. Nguyen *et al.*, "A novel segmentation framework for uveal melanoma in magnetic resonance imaging based on class activation maps," *Proceedings of Machine Learning Research*, 2019.

[39] H. G. Nguyen *et al.*, "Personalized Anatomic Eye Model From T1-Weighted Volume Interpolated Gradient Echo Magnetic Resonance Imaging of Patients With Uveal Melanoma," *International Journal of Radiation Oncology Biology Physics*, vol. 102, no. 4, pp. 813–820, 2018, ISSN: 1879355X. DOI: 10.1016/j.ijrobp.2018.05.004.

[40] J. X. Kane and D. F. Chang, "Intraocular Lens Power Formulas, Biometry, and Intraoperative Aberrometry: A Review," *Ophthalmology*, vol. 128, no. 11, e94–e114, Nov. 2021, ISSN: 0161-6420. DOI: 10.1016/j.ophtha.2020.08.010. [Online]. Available: https://doi.org/10.1016/j.ophtha.2020.08.010.

[41] M. S. Rajan, C. Bunce, and S. Tuft, "Interocular axial length difference and age-related cataract.," eng, *Journal of cataract and refractive surgery*, vol. 34, no. 1, pp. 76–79, Jan. 2008, ISSN: 0886-3350 (Print). DOI: 10.1016/j.jcrs.2007.08.023.

[42] P. Afonso and V. Mascarenhas, "Imaging techniques for the diagnosis of soft tissue tumors," *Reports in Medical Imaging*, vol. Volume 201, pp. 63–70, Apr. 2015. DOI: 10.2147/RMI.S54490.

[43] N. Zorgautoriteit, *Tarieventabel dbc-zorgproducten en overige-zorgproducten per 1 januari 2019*, 2019. [Online]. Available: https://puc.overheid.nl/nza/doc/PUC_236092_22/1/.

[44] J. P. Moriarty, B. J. Borah, R. L. Foote, J. S. Pulido, and N. D. Shah, "Cost-effectiveness of proton beam therapy for intraocular melanoma," *PloS one*, vol. 10, no. 5, e0127814–e0127814, May 2015, ISSN: 1932-6203. DOI: 10.1371/journal.pone.0127814. [Online]. Available: https://pubmed.ncbi.nlm.nih.gov/25993284.

[45] J. Köberlein, K. Beifus, C. Schaffert, and R. P. Finger, "The economic burden of visual impairment and blindness: A systematic review.," *BMJ open*, vol. 3, no. 11, e003471, Nov. 2013, ISSN: 2044-6055 (Electronic). DOI: 10.1136/bmjopen-2013-003471.

[46] L. G. Fonk, T. A. Ferreira, A. G. Webb, G. P. Luyten, and J. W. M. Beenakker, "The economic value of mr-imaging for uveal melanoma," *Clinical Ophthalmology*, 2020, ISSN: 11775483. DOI: 10.2147/OPTH.S238405.

[47] M. Suheimat, P. K. Verkicharla, E. A. Mallen, J. J. Rozema, and D. A. Atchison, "Refractive indices used by the Haag-Streit Lenstar to calculate axial biometric dimensions," *Ophthalmic and Physiological Optics*, 2015, ISSN: 14751313. DOI: 10.1111/opo.12182.

[48] I. Escudero-Sanz and R. Navarro, "Off-axis aberrations of a wide-angle schematic eye model," *Journal of the Optical Society of America A*, vol. 16, no. 8, pp. 1881–1891, 1999. DOI: 10.1364/JOSAA.16.001881. [Online]. Available: http://josaa.osa.org/abstract.cfm?URI=josaa-16-8-1881.

[49] D. L. Cooke, T. L. Cooke, M. Suheimat, and D. A. Atchison, "Standardizing sum-of-segments axial length using refractive index models," *Biomedical Optics Express*, 2020, ISSN: 2156-7085. DOI: 10.1364/boe.400471.

[50] C. E. UK, "Cataracts in Adults: Management," 2017.

[51] R. Sheard, "Optimising biometry for best outcomes in cataract surgery," *Eye*, vol. 28, no. 2, pp. 118–125, 2014, ISSN: 1476-5454. DOI: 10.1038/eye.2013.248. [Online]. Available: https://doi.org/10.1038/eye.2013.248.

[52] A. B. Bhatt, A. C. Schefler, W. J. Feuer, S. H. Yoo, and T. G. Murray, "Comparison of predictions made by the intraocular lens master and ultrasound biometry.," eng, *Archives of ophthalmology (Chicago, Ill. : 1960)*, vol. 126, no. 7, pp. 929–933, Jul. 2008, ISSN: 1538-3601 (Electronic). DOI: 10.1001/archopht.126.7.929.

[53] A. Roy, S. Das, S. K. Sahu, and S. Rath, "Ultrasound Biometry vs. IOL Master," *Ophthalmology*, vol. 119, no. 9, 1937–1937.e2, Sep. 2012, ISSN: 0161-6420. DOI: 10.1016/j.ophtha.2012.06.006. [Online]. Available: https://doi.org/10.1016/j.ophtha.2012.06.006.

5

MRI enables accurate diagnosis and follow-up in UM patients after vitrectomy

M.G. Jaarsma-Coes, T.A. Goncalves Ferreira, G.R. van Haren, M. Marinkovic, J.W.M. Beenakker

This chapter has been published in Melanoma Research **29.6**, 655-659 (2019) [1]

Uveal melanoma (UM), the most common primary intraocular tumour, is often complicated by exudative retinal detachment (RD). Sometimes, this exudative RD is mistaken for a rhegmatogenous detachment and is subsequently treated with vitrectomy with silicone oil (SiOil) tamponade. As SiOil prevents ultrasound imaging, the diagnosis, treatment planning and/or follow-up of UM underlying the detachment are often severely hindered by the SiOil. We aim to develop and evaluate new MRI methods to image UM patients with a SiOil tamponade and evaluate this in vivo. A dedicated MRI protocol for 3 and 7T was developed and subsequently evaluated in three patients. The MRI protocol developed was evaluated in three patients. In the first patient, SiOil hindered follow-up and therefore MRI was indicated. No tumour recurrence was found after two follow-up scans. The second and third patient underwent vitrectomy with SiOil for assumed rhegmatogenous RD in another hospital, during which a mass was found. In these cases, MRI was used to determine whether the lesion was UM and perform measurements to plan brachytherapy treatment. In general, the proposed workflow is more complicated on 7T than on 3T as the off-resonance effects scale linearly with field strength. For example, the shimming procedure needed modifications at 7T, whereas at 3T, the automatic shimming sufficed. However, at 7T, higher resolution images were obtained compared with 3T (0.6 vs. 0.8 mm^3). A dedicated MRI protocol enables high-resolution imaging of vitrectomized eyes with SiOil tamponade, enabling treatment planning or follow-up in UM patients.

5.1 Introduction

Uveal melanoma (UM) is the most common primary intraocular tumour [2, 3]. Exudative retinal detachment (RD) is a common complication of UM, possibly the result of a reduced venous return, caused by the tumour, leading to diffuse choroidal leakage [4]. Exudative RD can be mistaken for a rhegmatogenous RD, in which case the RD is treated by vitrectomy, that is, the vitreous body may be replaced with a silicone oil (SiOil) tamponade. Ultrasound (US), an important imaging modality in the diagnosis, treatment planning and follow-up of UM (figure 5.1a), is severely hindered by the SiOil as the sound waves reflect at the SiOil–water interface ((figure 5.1c). As the lack of an accurate imaging modality makes treatment planning or adequate follow-up impossible, alternative imaging options need to be developed to save the eye and vision of these patients. MRI, shown in (figure 5.1b), is, in principle, not hindered by the presence of SiOil, and could potentially provide the imaging data for these patients [5–8]. However, the strong off-resonance effects of SiOil prevent clinical interpretation of MRI acquired with conventional protocols (figure 5.1d). We therefore developed and evaluated a dedicated protocol to image UM patients with SiOil.

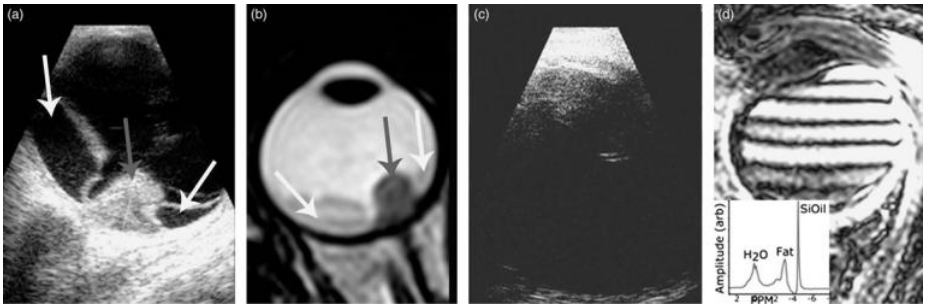

Figure 5.1: (a) Imaging using US reveals UM (grey arrow) and RD (white arrows). (b) MRI allows for a 3D evaluation of the tumour and surrounding structures. A T2-weighted image on which the tumour appears as a hypointense mass (grey arrow) with adjacent less hypointense RD (white arrows). (c) As US waves are reflected at the SiOil–water interface, US imaging is not possible in UM patients after vitrectomy, preventing accurate diagnosis or follow-up. (d) Although MRI should be possible in eyes with a SiOil tamponade, the off-resonance of the SiOil causes the conventional protocols to fail, resulting in strong artefacts. The MR spectrum of an UM patient with SiOil tamponade, showing the strong 4.5 ppm off-resonance of SiOil compared with water. The peak at 3.2 ppm is the fat signal from the orbital fat. RD, retinal detachment; SiOil, silicone oil; UM, uveal melanoma; US, ultrasound.

5.2 Methods

An MRI protocol was developed at 7T (Achieva; Philips Healthcare, Best, The Netherlands) and subsequently translated to 3T (Ingenia; Philips Healthcare). Preliminary experiments on the MR characteristics of the SiOil (RS-OIL ECS 1000cS, AL.CHI.MI.A. SRL, Ponte S. Nicolo, Italy) showed a T1 relaxation time of 0.9 and

1.3 s at 3 and 7T, respectively, with a 4.5 parts-per-million (ppm) frequency offset from water.

For optimal image quality, a surface coil should be used for MRI of the orbit [6, 7, 9]. On 7T, a house build dedicated eye coil [6] was used in combination with the Nova Medical transmit coil (Nova Medical Inc., Wilmington, Massachusetts, USA), whereas at 3T, a 47 mm surface receive coil (Philips Healthcare) in combination with the body transmit coil was used. As these surface coils have a very local sensitivity, they mainly receive a signal from the SiOil, which has a 4.5 ppm offset compared with water.

This off-resonance of the SiOil severely hinders the automatic calibration procedure of the MRI; thus, a manual calibration strategy was developed. First, a fast, low resolution, scan of the complete head was performed with the automatic calibration for an initial determination of the water resonance frequency, F_0, and RF-power settings. Subsequently, the correct settings for imaging the eye are determined by performing single voxel MR-spectroscopy (MRS) on the eye as MRS allows for a direct inspection of the resulting calibration (Fig. 1d). These parameters are then fixed and used for subsequent scans.

The clinical, 7T, imaging protocol consisted of T_1-weighted scans with and without SPIR SiOil suppression. As some residual liquid remains in the vitreous, an inversion-recovery MPRAGE scan (T-inv: 1280 ms) with SPIR SiOil suppression was used to supress both the remaining vitreous liquid and SiOil. The protocol furthermore included a T_2-weighted scan with SPIR SiOil suppression. During contrast administration of 0.1 mmol/kg gadoterate meglumine (gd-DOTA, DOTAREM; Guerbet, Roissy CdG Cedex, France), a dynamic contrast enhancement scan was performed. Finally, the T_1-weighted scans with SiOil suppression with and without water suppression were performed after gadolinium.

On 3T, the imaging protocol consisted of T_1-weighted and T_2-weighted scans without any suppression and with SPIR fat suppression. During contrast administration of 0.1 mmol/kg gd-DOTA, a dynamic contrast enhancement scan was performed. Finally, after contrast, the T_1-weighted scans with fat suppression were performed again.

The total MRI protocol took less than 50 min. An overview of the scan parameters can be found in table 5.1. This protocol was evaluated at 7T in one patient after informed consent. Later, two additional patients were referred from Ophthalmology and scanned on clinical indication. Ethical approval was obtained to access the data of these patients. All procedures performed in studies involving human participants were in accordance with the ethical standards of the institutional and/or the national research committee and with the 1964 Helsinki Declaration and its later amendments or comparable ethical standards.

	TR (ms)	TE (ms)	FA (deg)	NSA (n)	ETL (n)	Resolution (mm)	Scan time (min)	Additional information
3T								
T1 3D GE	5.2	2.2	10	1	88	0.8/0.8/0.8	3:27	
T2 3D GE	2500	311	90	2	117	0.8/0.8/0.8	3:35	
T2 MS fSE	1774	90	90	2	117	0.4/0.4/2.0	1:47	
T1 MS fSE SPIR	636	8	90	1	6	0.9/0.9/1.0	2:17	
Dynamic T1 3D GE SPIR	3.4	1.7	10	1	20	1.3/2.0/2.0	4:39	90 dynamics 3.1s/dynamic
T1 3D fSE SPIR	350	9.3	90	1	14	1.0/1.0/1.0	3:11	Post contrast
T1 MS fSE SPIR	764	8	90	1	6	0.5/0.5/2.0	1:16	Post contrast
7T								
3D T1 GE	4.9	2.5	10	4	500	0.5/0.5/0.5	2:39	
3D T1 GE SPIR	6	2.5	10	4	100	0.5/0.5/0.9	3:36	
3D T2 fSE SPIR	2500	254	90	1	120	0.6/0.6/0.6	2:55	
Dynamic 3D T1 GE SPIR	4	2	10	1	101	0.6/0.6/2.0	2:01	20 dynamics 6s/dynamic
3D T1 GE SPIR	6	2.5	10	4	100	0.5/0.5/0.9	3:36	Post contrast
3D T1 MPRAGE SPIR	5.6	2.9	9	1	92	0.5/0.5/1.0	2:53	Post contrast with additional H_2O suppression

Table 5.1: Scanning parameters of the 3T and 7T protocols.
ETL: echo train length, fSE: fast spin echo, GE: Gradient echo, MPRAGE: magnetization-prepared 180° radio frequency pulse and rapid gradient-echo, MS: multi slice, SPIR: spectral presaturation with inversion recovery.

5.3 Results

Determination of the correct MR settings did not always succeed after the first MRS scan. Often, there was still too large an F_0 offset to produce good shimming. This was, however, easily recognized in the resulting spectrum, and after manually correcting the initial F_0, on the basis of the offset of the first MRS-spectrum, a second MRS scan produced the correct settings (figure 5.1d inset).

The first patient received a SiOil tamponade after developing RD after UM resection and brachytherapy and was scanned at 7T. As the SiOil prevented US-based measurements needed for adequate screening for tumour recurrence, an MRI was requested. The MRI showed multiple lesions in the eye with a maximum basal diameter of 3 mm (figure 5.2a–c). The lesions located near the RD did not enhance after contrast administration, whereas the lesion located at the position of the original tumour did enhance. As this enhancement could be the result of either new tumour activity or radiotherapeutic damage, the patient received a second MRI 6 months later. As the enhancing lesion did not show any significant changes or growth compared with the first scan, it was classified as scarred residue or damage after radiotherapy treatment and thus enucleation could be avoided.

The second patient was referred after UM was suspected during vitrectomy for RD. On fundoscopy, the diagnosis of UM was confirmed and ruthenium plaque brachytherapy was considered optimal treatment. MRI obtained at 3T showed a slight residual RD and a lesion with a maximum prominence of 1.5 mm (without choroid) and a basal diameter of 6 mm (figure 5.2e). On the basis of these measurements, the optimal ruthenium brachytherapy applicator was selected and dose calculations for further treatment planning were performed.

In the third patient, a small mass was discovered during vitrectomy. On fundoscopy, a UM was suspected. As US imaging was not possible because of the SiOil, an MRI was requested to confirm diagnosis and to assess the tumour dimensions. The images, acquired at 3T, showed a slight focal thickening of the inner aspect of

the choroid located superior and medial to the optic nerve, which appears slightly hyperintense (figure 5.2f): because of the small size of the lesion, it was difficult to differentiate between physiologic enhancement, caused by the high vascularity of the uvea, and pathologic enhancement of the tumour. Overall, the MRI showed a lesion with characteristics corresponding with UM, which was later confirmed by a biopsy.

5.4 Discussion

In 1998, Herrick et al. [10] showed that 1.5T MRI can be used to image the eye after vitrectomy, but at that time, MRI had insufficient resolution to evaluate UM characteristics and size. Currently, surface coils [9] and higher field strengths enable high-resolution imaging, but both these advances make the MRI more susceptible to the off-resonance effects of SiOil. We have shown that through a modified set-up of the MRI, the eyes of vitrectomized patients can be evaluated successfully, which opens the route to eye-preserving therapy.

In general, the proposed workflow is more complicated at 7T than at 3T as the off-resonance effects scale linearly with field strength. As a result, at 3T, these patients can be scanned without major modifications to the scanner software. Some off-resonance effects are present in the images, but these do not limit clinical evaluation as at 7T, some minor adjustments to the scanner software were needed to scan these patients. However, at 7T, higher resolution images were obtained compared with 3T (0.6 vs. 0.8 mm3). At both field strengths, eye motion is a problem, but several techniques have been proposed, such as cued blinking [6, 11], that can limit these effects.

As the appearance of UM on MRI is significantly different from that on US, it is often difficult to relate the US images to the MRI. We therefore recommend that if a known UM patient develops RD, both an MRI and US are performed before the vitrectomy to correlate the MRI after vitrectomy to the US images taken before vitrectomy.

5.5 Conclusion

Although RD is a common complication of UM, the UM is often missed when these patients present in a peripheral hospital. If UM is discovered during the vitrectomy, the patient is referred to a specialized centre, but the SiOil tamponade hinders subsequent diagnosis and therapy. We have shown that a dedicated MRI protocol enables high-resolution imaging of vitrectomized eyes with UM, enabling eye-preserving treatment and follow-up of these patients.

5.6 Acknowledgements

The authors thank Maarten Versluis (Philips Healtcare, Best, The Netherlands) for stimulating discussion of the design of the MRI protocol and Berit Verbist (Radiology, LUMC) for assistance with the interpretation of the MR images.

5.7 References

[1] M. G. Jaarsma-Coes, T. A. Goncalves Ferreira, G. R. van Haren, M. Marinkovic, and J.-W. M. Beenakker, "MRI enables accurate diagnosis and follow-up in uveal melanoma patients after vitrectomy," *Melanoma Research*, vol. 29, no. 6, 2019, ISSN: 0960-8931.

[2] A. D. Singh, M. E. Turell, and A. K. Topham, "Uveal melanoma: Trends in incidence, treatment, and survival," *Ophthalmology*, vol. 118, no. 9, pp. 1881–1885, 2011, ISSN: 01616420. DOI: 10.1016/j.ophtha.2011.01.040.

[3] A. E. Chang, L. H. Karnell, and H. R. Menck, "The national cancer data base report on cutaneous and noncutaneous melanoma: A summary of 84,836 cases from the past decade," *Cancer*, vol. 83, no. 8, pp. 1664–1678, 1998, ISSN: 0008543X. DOI: 10.1002/(SICI)1097-0142(19981015)83:8<1664::AID-CNCR23>3.0.CO;2-G.

[4] T. Kivelä, S. Eskelin, T. Mäkitie, and P. Summanen, "Exudative retinal detachment from malignant uveal melanoma: Predictors and prognostic significance," *Investigative Ophthalmology and Visual Science*, vol. 42, no. 9, pp. 2085–2093, 2001, ISSN: 01460404.

[5] T. Wong *et al.*, "Magnetic resonance imaging of breast augmentation: a pictorial review," *Insights Imaging*, vol. 7, no. 3, pp. 399–410, 2016, ISSN: 18694101. DOI: 10.1007/s13244-016-0482-9. [Online]. Available: http://dx.doi.org/10.1007/s13244-016-0482-9.

[6] J. W. M. Beenakker *et al.*, "Clinical evaluation of ultra-high-field MRI for three-dimensional visualisation of tumour size in uveal melanoma patients, with direct relevance to treatment planning," *Magnetic Resonance Materials in Physics, Biology and Medicine*, vol. 29, no. 3, pp. 571–577, 2016, ISSN: 13528661. DOI: 10.1007/s10334-016-0529-4.

[7] P. de Graaf *et al.*, "Guidelines for imaging retinoblastoma: Imaging principles and mri standardization," *Pediatric radiology*, vol. 42, no. 1, pp. 2–14, 2012.

[8] M. Kamrava *et al.*, "Quantitative multiparametric MRI in uveal melanoma: increased tumor permeability may predict monosomy 3," *Neuroradiology*, vol. 57, no. 8, pp. 833–840, 2015, ISSN: 14321920. DOI: 10.1007/s00234-015-1546-0.

[9] E. A. Vokurka, N. A. Watson, Y. Watson, N. A. Thacker, and A. Jackson, "Improved high resolution MR imaging for surface coils using automated intensity non-uniformity correction: Feasibility study in the orbit," *Journal of Magnetic Resonance Imaging*, 2001, ISSN: 10531807. DOI: 10.1002/jmri.1217.

[10] R. C. Herrick, L. A. Hayman, R. K. Maturi, P. J. Diaz-Marchan, R. A. Tang, and H. M. Lambert, "Optimal imaging protocol after intraocular silicone oil tamponade," *American Journal of Neuroradiology*, vol. 19, no. 1, pp. 101–108, 1998, ISSN: 01956108.

[11] B. A. Berkowitz, C. McDonald, Y. Ito, P. S. Tofts, Z. Latif, and J. Gross, "Measuring the human retinal oxygenation response to a hyperoxic challenge using MRI: Eliminating blinking artifacts and demonstrating proof of concept," *Magnetic Resonance in Medicine*, vol. 46, no. 2, pp. 412–416, 2001, ISSN: 07403194. DOI: 10.1002/mrm.1206.

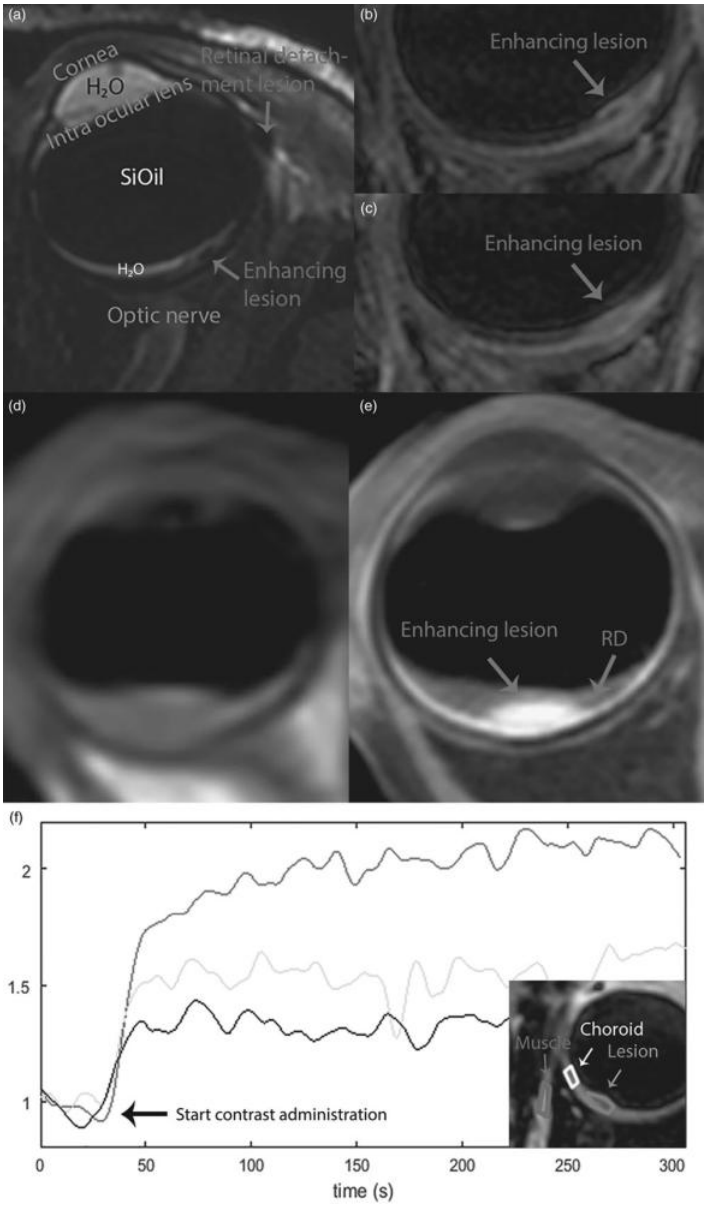

Figure 5.2: (a–c) 7T MRI of the first patient. (a) Annotated T2 image with spectral presaturation with inversion recovery silicone oil (SiOil). (b) The T1-weighted image after contrast with SiOil and free-water suppression showed an enhancing lesion (arrow), which did not significantly change after a rescan 6 months later (c). (d) Precontrast and (e) postcontrast T1-weighted image of the second patient, scanned at 3T. (f) Dynamic imaging during the contrast administration allows for an analysis of the perfusion of the different anatomies of the eye. The enhancement curves of muscle, lesion and choroid show that the lesion enhances, but only slightly more than the normal retinal tissue. RD, retinal detachment.

6

Eye specific quantitative dynamic contrast enhanced MRI analysis for patients with intraocular masses

M.G. Jaarsma-Coes, T.A. Ferreira, P.J. van Houdt, U.A. van der Heide, G.P.M. Luyten, J.W.M. Beenakker

This chapter has been published in Magnetic Resonance Materials in Physics, Biology and Medicine, 1-13 (2021)[1]

Dynamic contrast enhanced (DCE)-MRI is currently not generally used for intraocular masses as lesions are small, have an inhomogeneous T_1 and the eye is prone to motion. The aim of this paper is to address these eye specific challenges, enabling accurate ocular DCE-MRI. DCE-MRI of 19 uveal melanoma (UM) patients was acquired using a fat-suppressed 3D spoiled gradient echo sequence with TWIST (time-resolved angiography with stochastic trajectories sequence). The analysis consisted of a two-step registration method to correct for both head and eye motion. A T_1-map was calculated to convert signal intensities to concentrations. Subsequently the Tofts model was fitted voxel wise to obtain K^{trans} and v_e. Registration significantly improved the concentration curve quality ($p < 0.001$). The T_1 of melanotic lesions was significantly lower than amelanotic lesions (888 ms vs 1350 ms, $p = 0.03$). The average achieved B_1^+ in the lesions was 91%. The average K^{trans} was 0.46 min^{-1} (range: 0.13-1.0) and the average v_e was 0.22 (range: 0.10-0.51). Using this eye-specific analysis, DCE of intraocular masses is possible which might aid in the diagnosis, prognosis and follow-up of UM.

6.1 Introduction

Most intraocular lesions are benign, such as choroidal neavi, haemangiomas and leiomyomas, but also various malignant intraocular masses exist. Although uveal melanoma (UM) is relatively rare, with an incidence of 14 per million in the Netherlands[2], it is the most common primary intraocular tumour. It mostly originates from the choroid (90%), but can also originate from the iris or ciliary body[3,4]. Other malignant ocular lesions include mainly metastases from other tumour sites or even more rare lesions such as retinoblastoma[5,6]. As the prognosis and treatment of benign lesions, UM and other malignant ocular lesions differ, it is important to have an accurate diagnosis[3,6]. For the differentiation between these different lesions the ophthalmologist primarily relies on fundoscopic, fluorescent angiography and ultrasound imaging (figure 6.1a-d)[7]. However, in some patients this differentiation is quite challenging, especially for amelanotic melanomas, or lesions behind the iris.

In the last decade, advances in ocular MRI, such as dedicated receive coils[8] and dedicated acquisition strategies[9] have resulted in different new clinical applications of MRI for ocular conditions[10]. MRI offers a superior evaluation of the extend of eye lid tumours[11], can be instrumental in the diagnosis and assessment of disease progression in orbital disease involving extra-ocular muscles[12], provide insight into ocular complaints such as negative dysphotopsia[13] and allows for a more accurate assessment of tumour dimensions for radiotherapy therapy planning[14,15]. Furthermore, diffusion weighted imaging is emerging as a promising early marker of therapy response after ocular proton beam therapy[16], while quantitative dynamic contrast enhanced MRI (DCE-MRI) could assist in the differential diagnosis of intraocular masses and monitoring of treatment response of UM[17]. The use of DCE-MRI of ocular masses is often limited to the evaluation of the time intensity curve (TIC, figure 6.1f-h)[17–20]. However, Wei et al.[18] and Kamrava et al.[21] have shown contradicting results on the relation between tumour permeability and metastatic risk. Kamrava et al.[21] found a higher K^{trans} in UM patients with monosomy 3, a subset of UM patients who have a strong increased risk of developing metastatic disease[22]. Conversely Wei et al.[18] showed a decreased K^{trans} (a lower peak signal intensity) in patients with metastatic disease. Although these papers are an improvement compared to the current clinical practice and other research where some eye-related challenges were not addressed such as small lesion size, eye motion and difference in melanin content.

The limited use of quantitative DCE-MRI might be due to the eye-specific challenges of MR-imaging in general. One of the main challenges of DCE-MRI of intraocular masses is the small size of the eye, containing even smaller lesions, generally with a thickness of less than 5 mm. Furthermore, the eye is prone to movement, which in combination with the small lesion size leads to a mismatch of the tumour location between timepoints[19]. Finally, intraocular lesions can be pigmented (large amount of melanin), unpigmented (no melanin) or partially pigmented[23]. This varying degree of pigmentation results in a large variability in pre-contrast longitudinal relaxation time (T_1)[24], which directly affects the quantification of concentration of

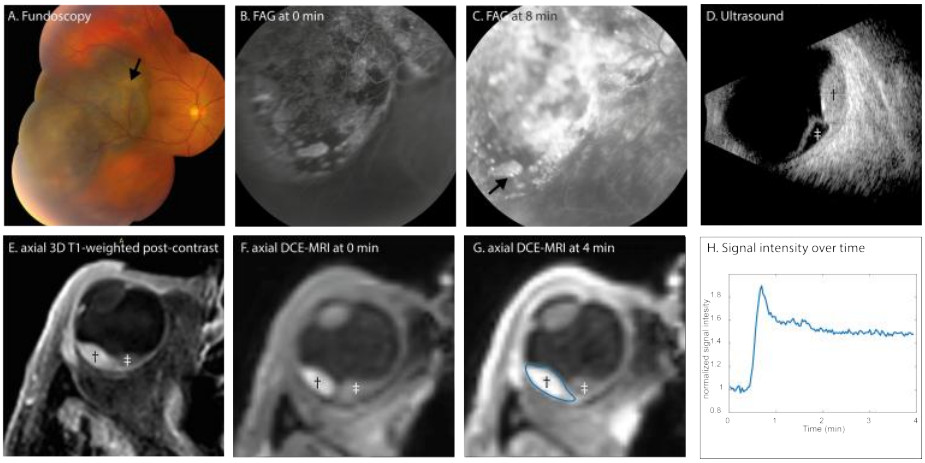

Figure 6.1: Conventional ophthalmic imaging and MRI of patient 13. (A–D) Conventional ophthalmic imaging of an UM. The fundus photo (A) shows a pigmented lesion with lipofuscin (arrow). The lesion is enhancing with pinpoints (C, arrow) on the fluorescent angiography (FAG, B, C). On ultrasound (US, D), the lesion (dagger) has an intermediate reflectivity, while the retinal detachment (double dagger) has a low reflectivity and the dimensions of the lesion are measured. On MRI, an enhancing lesion (dagger) with associated retinal detachment (double dagger) is visible (E–G). In contrast to the FAG, the change of the signal intensity after contrast administration can be visualized in DCE-MRI (H)

the, generally T_1-based, contrast agent. However, recent improvements in ocular MR-imaging protocols such as the use of a surface coil for receiving the signal and implementation of time-resolved angiography with stochastic trajectories sequence[25] allow for the acquisition of DCE-MRI with sufficient temporal and spatial resolution to perform DCE-MRI[19]. The aim of this paper is to overcome eye specific challenges in the DCE-MRI analysis of intraocular masses.

6.2 Methods

6.2.1 Study population

Nineteen patients diagnosed with UM were included for this study. Nine patients were scanned as part of a prospective study and were recruited randomly. This study has been approved by the local ethics committee and subjects were scanned after written informed consent. The data from the remaining 10 patients were selected from UM patients with a tumour prominence >3 mm who received an MRI as part of clinical care. This retrospective inclusion of data was approved by the local ethics committee. The patients were on average 63 years old (range 30 to 82 years), 68% (n=13) were male and had a BMI of 26.6±4.5. The lesions had an average prominence of 7.8 mm and an average largest basal diameter of 14.5 mm on ultrasound. The American Joint Committee on Cancer staging[26] ranged from T1 to T4 with most patients in the T3 (n = 8) and T4 (n = 6) stage. Most were primary

tumours (18/19) but in one case (UM15) the patient had a large reoccurrence. The primary tumour was treated with ruthenium plaque therapy and was located at the other side of the eye. A detailed description of the cohort of patients can be found in table 6.1.

Patient no.	Tumour stage	Age at diagnosis (years)	BMI	Prominence on US (mm)	LBD on US (mm)
UM 1	T3a	71	20	3.3	14.9
UM 2	T3a	61	30	12.3	14.4
UM 3	T2c	82	Missing	4	10.5
UM 4	T2b	68	22	5	11
UM 5	T4a	71	29	7.3	15.7
UM 6	T2a	73	32	2.8	9.5
UM 7	T3b	30	22	6.1	14.9
UM 8	T3a	37	35	6	14.6
UM 9	T2a	50	29	2.5	10
UM 10	T4a	80	27	12.1	15.5
UM 11	T1c	73	28	5.8	6.6
UM 12	T4a	62	19	11	22.6
UM 13	T4a	59	31	5.7	17.4
UM 14	T4b	75	26	13.9	18.8
UM 15	T3b	83	26	9.5	15
UM 16	T3b	64	21	8.4	15.6
UM 17	T4b	45	27	13	18
UM 18	T3b	65	29	9.1	14.8
UM 19	T3a	53	29	9	15.1

Table 6.1: Patient characteristics
LBD: Largest basal diameter, US: Ultrasound

6.2.2 MRI protocol

All patients were scanned before treatment on a 3T MR scanner (Ingenia, Philips Healthcare, the Netherlands) using the protocol described by Ferreira et al[19] and a 47 mm diameter surface receive coil covering the affected eye (figure 6.2). The scan parameters of the relevant sequences are listed in table 6.2. Patients were instructed not to wear eye makeup and the affected eye was taped shut. In the last 6 patients a wet gauze was placed on top of the eye to minimize susceptibility artefacts. Patients were immobilized as much as possible using a radiotherapy head support (MaxSupportTM wide shaped, red variant, 117000 HSSETW, Medeo, Schöftland, Switzerland) (figure 6.2). The dynamic time series were acquired using a fat-suppressed 3D spoiled gradient echo sequence with a spatial resolution of 1.25x1.5x1.5 mm^3. A bolus of 0.1 mmol/kg gadolinium (DOTAREM; Guerbet, Roissy CdG Cedex, France) was administered 6 s after the start of the scan followed by a 20 ml injection of isotonic saline, using a power injector with an injection rate of 2 ml/sec. The first eight patients were scanned with a flip angle of 5 degrees to match the then used 7 Tesla protocol, where the flip angle was limited to 5 degrees due to SAR restrictions. The flip angle was increased to 13 degrees for subsequent patients as this provided a more optimal contrast for the contrast agent concentrations in our patients as theoretically the optimal flip angle for our spoiled gradient echo sequence is between 13 and 16 degrees assuming a T_1 between 600 and 1500 ms[27]. Time-resolved angiography with stochastic trajectories sequence (TWIST)[25], with a central size of 25% and a peripheral density of 20%, was implemented to

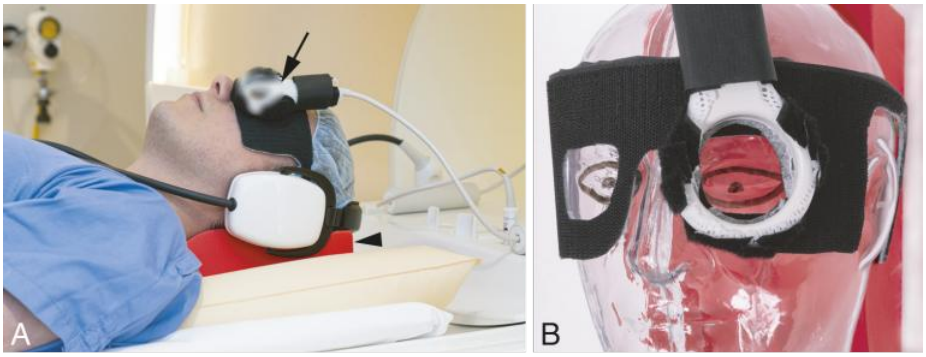

Figure 6.2: (A) The patient was scanned using a 47mm surface receive coil (arrow). This coil was positioned over the affected eye. The head was supported by a radiotherapy head support (arrowhead). (B) Clarification of the positioning of the eye coil on a phantom.

increase the temporal resolution to 2 s per dynamic scan to reduce motion artefacts per dynamic image. To determine the baseline lesion T_1, a 3D spoiled gradient echo flip angle series, with flip angles of 2, 5, 9 and 15 degrees, was acquired before the dynamic scan with the same field of view (FOV). Additionally, a $B_1{}^+$-map was acquired using the DREAM sequence[28]. Finally a post-contrast $3DT_1$-weighted scan ($3DT_1$gd) was acquired for anatomical reference.

	T_1-mapping	$B_1{}^+$-mapping	DCE-MRI	$3DT_1$-weighted
Voxel size (mm^3)	1.25x1.5x1.5	2.0x2.0x2.0	1.25x1.5x1.5	1.0x1.1x1.0
FOV (mm^3)	80x80x32	160x120x33	80x80x32	80x80x40
TR (ms)	7	7.1	4.5	350
TE(1) (ms) / TE(2) (ms)	3.1	4.6/6.9	2.3	9.4
FA (deg)	2/5/9/15	10	5 or 13	90
Fat. sup.	Proset 11	SPIR	Proset 11	SPIR
Averages	1	2	1	1
Scantime (mm:ss)	4 x 00:09	00:21	04:20	03:23
Remarks		0.2 mm gap	2 s/dynamic; TWIST	Post contrast administration

Table 6.2: Scan parameters
FOV: Field of view, TR: repetition time, TE: echo time, FA: flip angle, Fat.Sup: fat suppression, SPIR: Spectral Presaturation with Inversion Recovery, TWIST[25]: time-resolved angiography with stochastic trajectories sequence, a dynamic scan technique where the a semi-randomly part of the 20% of outer k-space is acquired per dynamic.

6.2.3 DCE analysis

The analysis of the DCE data consisted of four steps. First, the images of the dynamic scan, flip angle series, $B_1{}^+$-map and $3DT_1$gd scan were registered to the dynamic dataset and the lesion was segmented on the $3DT_1$gd image. Second, a T_1-map was calculated using the flip angle series and $B_1{}^+$-map, which was subsequently used to calculate the gadolinium concentration for each lesion voxel in the dynamic scan. Finally, pharmacokinetic modelling was applied using the Tofts model[29].

6.2.4 Registration

All timepoints of the dynamic scan were rigidly registered to the 50th of the 125 timepoints in two steps using Elastix 4.9.0 [29]. The 50th timepoint was chosen as it had an intensity comparable to most timepoints, which was beneficial for automatic image registration. The first step consisted of registration of the full FOV to correct for head motion. Subsequently an eye-mask was created using an in-house build Mevislab network (3.0.2, MeVis Medical Solutions AG, Bremen, Germany[30]). The eye-mask was used for a masked registration to reduce eye motion between timepoints. Additionally, the variable flip angle series, $B_1{}^+$-map and $3DT_1$gd scan were rigidly registered to the 50th timepoint using masked registration.

6.2.5 Segmentation

A lesion mask was created by manually segmenting the UM on the $3DT_1$gd images using ITK-SNAP[31]. Elastix was used to translate this mask to the registered dynamic scan, using the earlier obtained transformation matrix. Subsequently the voxels within this mask were selected for the pharmacokinetic analysis .

6.2.6 T_1-mapping

The pre-contrast T_1 value of each voxel was obtained from the flip angle series in Matlab (version R2019b, MathWorks, Natick, Massachusetts, USA) as described by Fram et al.[32] and Gupta et al.[33]. The flip angles were corrected according to the median achieved $B_1{}^+$ of the lesion. Subsequently, a masked 3D median filter with 26-connected components was applied to the T_1-map to remove potential outliers within the lesion. Voxels outside the lesion were excluded from the filter, as the vitreous has significantly higher T_1 values than the lesion[34]. The UM were classified as melanotic, amelanotic or mixed based on description of the tumour in the medical status by an ophthalmologist.

6.2.7 Pharmacokinetic modelling

The signal intensities from the DCE-images were converted to concentration time profiles, using the relations described by Tofts[29], assuming a gadolinium relaxivity of 3.4 L mmol^{-1} s^{-1} [35]. For each voxel the peak concentration was defined as the 95th percentile of the concentration over time. Voxel-by-voxel pharmacokinetic modelling (PKM) was performed using nonlinear least squares fitting of the standard Tofts model using in house build scripts in Matlab. First, the bolus arrival time (BAT) was determined for each patient by fitting the PKM for the first 40 time points of the median lesion concentration curve for 25 different BATs. The BAT with the lowest residuals was selected. The automatic determined BAT was visually correct in 50% of the patients. In the remaining patients the BAT was shifted with one timepoint in 8 cases and two timepoints in 3 cases. Subsequently the PKM was fitted to the full dynamic concentration curve (C(t)) for each voxel within the lesion to obtain the K^{trans} (vascular permeability [min^{-1}]) and v_e (extravascular extracellular space per

volume of tissue [unitless]). As no major feeding arteries were in the field-of-view of the DCE scan, an earlier derived population arterial input function (AIF) was used, which was derived from the carotid arteries in ten brain cancer patients. The fit of the Parker AIF to the average AIF resulted in the following parameters: A1 = 46.7 mM· s, $\sigma 1$ = 3.5 s, T1 = 12.5 s, A2 = -4.7 mM·s , $\sigma 2$ = 5.2 s, T2 = 26.9 s, α = 1.4 mM, β = 0.003 s^{-1}, s = 8.3 s^{-1}, τ = 17.5 s.

6.2.8 Evaluation of the registration

The effect of the registration was evaluated by comparing the concentration curves before and after registration of fifteen randomly selected lesion voxels for all patients. The curves from all patients were randomized and presented unannotated to prevent a potential bias. The observer scored each curve as being sufficient or insufficient for automatic fitting and scored which of the two curves had the best quality or whether the quality was the same based on the amount of visual variance/spikes and motion artefacts in the concentration curve. Observer 1 (MJ) scored all 285 curves and observer 2 (JWB) scored a random subset of 50 to validate the scores. The scores were evaluated using a two-sided Wilcoxon signed rank test.

6.2.9 Evaluation of the error propagation

The effect of the precision error of the $B_1{}^+$, T_1 and registration on the pharmacokinetic analysis were assessed. First, in two additional UM patients, the flip angle series and $B_1{}^+$ map were acquired twice to determine the repeatability of the $B_1{}^+$ and T_1 measurements. Secondly, the effect precision errors in $B_1{}^+$, T_1 and registration on K^{trans} and v_e was assessed to determine the sensitivity of small inaccuracies of the different analysis steps on the final DCE parameters. To this end the results of different intermediate steps were manually modified in two different patients: a patient with a medium sized amelanotic tumour with a $B_1{}^+$ of 82% (patient 7) and a patient with a large melanotic tumour and a $B_1{}^+$ of 96% (patient 10). The effect of a precision error in $B_1{}^+$ measurement was assessed by increasing and decreasing the measured $B_1{}^+$ with 2 and 5 percent. The sensitivity to T_1 changes was determined by changing the measured T_1 for all voxels by 30 ms, the measured precision error for the T_1 mapping, or 60 ms, and 2 and 5 percent of the average tumour T_1 respectively. Finally, the effect of imprecise registration was estimated by artificially shifting the images of individual time-points. Regular eye-motion was simulated by a one voxel shift during 2 time-points after 175 seconds, while the most unfavourable case was simulated by the same shift but immediately after bolus arrival. For all cases, the median K^{trans} and v_e of the tumor were compared with the original analyses.

6.2.10 Statistical analysis

The impact of the different analysis steps on the final PKM was evaluated. The K^{trans} values with and without registration and with and without $B_1{}^+$-correction were visualized. The effect of T_1-mapping was evaluated by comparing the K^{trans}

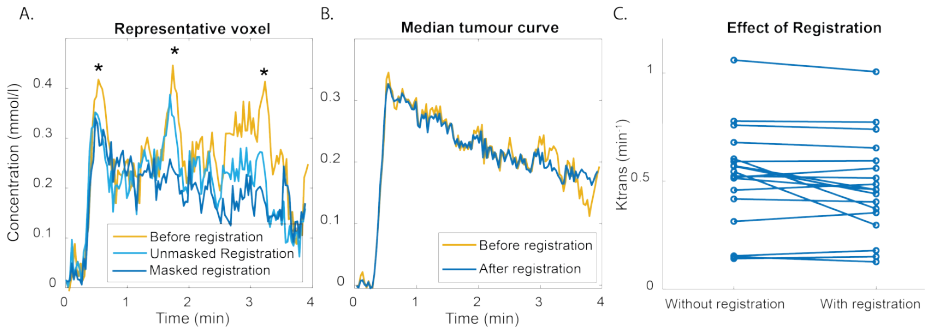

Figure 6.3: (A,B) Concentration time curves of a representative patient (18) before and after registration. Before registration motion artefacts were present (asterisk) furthermore, unmasked registration was not able to fully resolve the motion. A movie of the dynamic scan of patient 18 visualizing the motion in the scan can be found in the supplementary materials. (C) Registration changes the K^{trans} of the UM patients with an average of 0.06 min^{-1}

values based on concentration data with the average T_1 of all patients with the model in which data from the individual T_1 map was used. The difference in K^{trans} between melanotic and amelanotic lesions for a population T_1 and individual T_1 was tested using unpaired t-tests. The reported PKM values in this paper are the median of the voxels within the lesion mask as the values are not normally distributed. The error bars shown in the figures are the 25^{th} and 75^{th} percentile (IQR). The reported unpaired t-tests were calculated using Matlab. A p-value of 0.05 or smaller was considered statistically significant.

6.3 Results

6.3.1 Registration

The centre of the eye moved up to 3.0 mm (average 1.3 mm) during the 4 minutes acquisition of the dynamic time series with rotations of up to 20 degrees (average 6 degrees) with respect to the first time point.

Registration resulted in a significant improvement in the quality of the concentration curves ($Z = 8.9$, $p < 0.001$). Figure 6.3 shows a representative curve before and after registration. Eye-motion can result in changes in the enhancement and concentration curves, as even small eye motion can result in mismatch between the ROI and actual lesion location, as can be seen in figure 6.3. Without registration, there were spikes (figure 6.3, asterisk) in the contrast agent concentration, which were caused by motion, most likely eye blinks or a different gaze angle. In this case, most of the artefacts were no longer apparent after registration of the eye, although still some residual motion artefacts can be seen in the concentration curve. Note that eye motion was not resolved with the unmasked registration.

Before registration 40% (n = 113/285) of the curves were scored as insufficient quality to perform a fit compared to 15% (n = 43/285) after registration. In 55% of the curves (n = 157/285) the curve was scored as improved, in 36% (n = 102/285) of the curves no clear effect of the registration was observed, while in 9% (n = 26/285) the curve was scored as deteriorated after registration although in 15/26 of these curves the curves received the same quality, indicating a minimal difference. No significant difference in scoring was found between the scoring of observer 1 and 2 (p = 0.09).

The reported increase in quality of the concentration curves after registration resulted in a change of the PKM parameter values. The maximum absolute change in K^{trans} was 0.25 min^{-1} with an average absolute change of 0.06 min^{-1} (figure 6.3c & table 6.3).

Patient	Ktrans	Without registration	% change	Without B1+	% change	Average T1	% change
UM 1	0.20	0.18	-10	0.27	36	0.26	31
UM 2	0.46	0.57	24	0.77	68	0.70	51
UM 3	0.37	0.60	62	0.50	33	0.19	-50
UM 4	0.13	0.15	18	0.17	35	0.16	23
UM 5	0.46	0.51	11	0.55	20	0.52	13
UM 6	0.15	0.14	-6	0.18	20	0.11	-28
UM 7	0.30	0.54	84	0.44	49	0.53	80
UM 8	0.40	0.42	3	0.50	24	0.55	35
UM 9	0.35	0.32	-11	0.44	24	0.52	47
UM 10	0.77	0.78	1	0.85	9	0.94	22
UM 11	0.18	0.15	-14	0.29	64	0.19	7
UM 12	0.44	0.57	29	0.44	0	0.43	-2
UM 13	0.65	0.68	4	0.76	16	0.46	-30
UM 14	0.51	0.52	2	0.72	39	0.29	-44
UM 15	0.59	0.59	-1	0.80	35	0.27	-55
UM 16	0.49	0.46	-6	0.61	26	0.20	-59
UM 17	1.01	1.06	5	1.03	3	1.17	17
UM 18	0.56	0.52	-7	0.68	21	0.25	-55
UM 19	0.74	0.76	3	0.70	-6	0.82	10

Table 6.3: K^{trans}

6.3.2 B_1^+ and T_1-mapping

The median lesion T_1 per patient showed a wide range from 522 ms to 1509 ms as is shown in figure 6.4b. The average T_1 of all patients was 1122 ms, this value was used as population T_1 for subsequent comparisons on the effect of $T1_1$ on the PKM. Amelanotic lesions had an average T_1 of 1350 ms while the average T_1 of 888 ms for the melanotic lesions was significantly lower (p = 0.03). The average T_1 of the mixed lesions was 1193 ms. The average achieved B_1^+ in the lesion was 91% (range 77% to 104%). Correction of the flip angles resulted in an average absolute change in T_1 of 208 ms and an absolute change in K^{trans} of 0.11 min^{-1}, figure 6.4c & table 6.3.

When a population average T_1 was used the K^{trans} appeared to mainly resemble the amount of pigmentation, with the melanotic showing a significant lower K^{trans} compared to amelanotic lesions ($p < 0.01$, figure 6.4d). However, when the actual

Sensitivity to inaccuracies in the registration	2-3 minutes after contrast arrival		Immediately after contrast arrival					
Relative change in	Ktrans	ve	Ktrans	ve				
Plateau curve / Medium sized UM	-0.5%	-0.6%	3.0%	-0.5%				
Washout curve / Large UM	-0.2%	0.1%	2.6%	0.1%				
Sensitivity to inaccuracies in B1+	B1+ - 5%		B1+ - 2%		B1++ 2%		B1+ + 5%	
Relative change in	Ktrans	ve	Ktrans	ve	Ktrans	ve	Ktrans	ve
Low achieved B1 (82%)	-10.7%	-7.2%	-3.6%	0.3%	6.4%	10.6%	14.1%	18.7%
Normal achieved B1 (96%)	-11.8%	-7.4%	-5.8%	-1.2%	2.5%	7.5%	8.9%	14.2%
Sensitivity to inaccuracies in T1	T1 - 60ms		T1 - 30ms		T1 + 30ms		T1 + 60ms	
Relative change in	Ktrans	ve	Ktrans	ve	Ktrans	ve	Ktrans	ve
Amelanotic UM	10.7%	9.4%	5.4%	4.8%	-5.0%	-4.7%	-8.9%	-9.2%
Melanotic UM	6.7%	6.0%	3.3%	3.1%	-3.4%	-2.8%	-6.8%	-5.8%

Table 6.4: Error propagation

T_1 was included in the analysis, the K^{trans} changed with 0.15 min^{-1} on average (figure 6.4d & table 6.3) and the bias was resolved as no systematic difference was found between the K^{trans} of melanotic and amelanotic lesions ($p = 0.37$).

The strong effect of the melanin concentration on the perfusion quantification can be seen in a mixed lesion with both a melanotic and amelanotic lobe, Figure 6.5. On the TIC, the amelanotic part of the lesion appeared to be enhancing stronger than the melanotic part, 225% vs 150%. The melanotic lobe has, however, an almost 1000 ms shorter T_1 than the amelanotic lobe, on average 494 ms vs 1464 ms respectively. When the T_1 was included in the conversion to concentration, a very similar concentration was found in both lesions, although still a higher peak concentration was measured in the early timepoints of the amelanotic lobe.

6.3.3 Pharmacokinetic parameters

When all corrections were applied, a wide range of K^{trans} values was observed (figure 6.6c). The median K^{trans} per lesion ranged from 0.13 to 1.0 min^{-1} with a mean of 0.46 min^{-1}. The median v_e was 0.22 on average with a range from 0.10 to 0.51. Within lesions a wide distribution of K^{trans} and v_e was observed. The maximum IQR (75^{th} -25^{th} percentile) of the K^{trans} was 0.99 min^{-1} and the average IQR was 0.40 min^{-1}. For the v_e the maximum IQR was 0.83 and the average IQR was 0.18.

6.3.4 Error propagation

The average precision error of the achieved $B_1{}^+$ and $T1_1$ was 0.2% and 30 ms respectively. Major inaccuracies (5%) in the measurement of the achieved $B_1{}^+$ can result in a difference up to 12% in the determined K^{trans} and 19% in the determined v_e (table 4). Differences in the T_1 measurement (30 ms) can lead to changes in K^{trans} and v_e up to 5% (table 4). Imprecisions in the registration during the second half of the acquisition had a minimal effect on the outcomes of K^{trans} and v_e ($< 1\%$), while a similar imprecisions directly after contrast uptake resulted in 3% change in Ktrans.

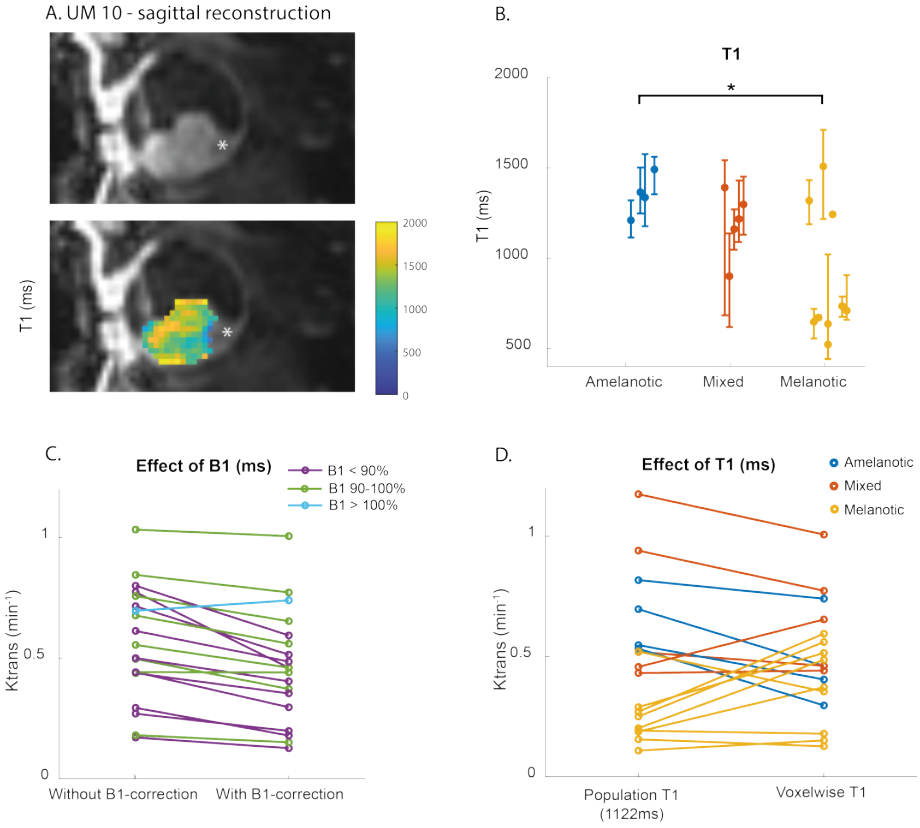

Figure 6.4: T1-mapping
(A) Slice of UM patient 10 showing an inhomogeneous T_1 of the lesion. The retinal detachment (Asterix) is excluded from the analysis. (B) T_1 values of amelanotic, mixed, melanotic and non-UM lesions (median and IQR). The three melanotic lesions with a higher T_1 are small lesions most likely suffering from partial volume effects. The T_1 between amelanotic and melanotic lesions is significantly different ($p = 0.03$). No significant difference was found between mixed lesions and either amelanotic or melanotic lesions. (B,C) $B_1{}^+$-correction change the K^{trans} with an average of 0.11 min^{-1}. (D) When a population T_1 was used the K^{trans} mainly resembled the amount of pigmentation with a low K^{trans} for melanotic lesions. When the actual T1 was used the Ktrans changed with an average of 0.15 min^{-1}.

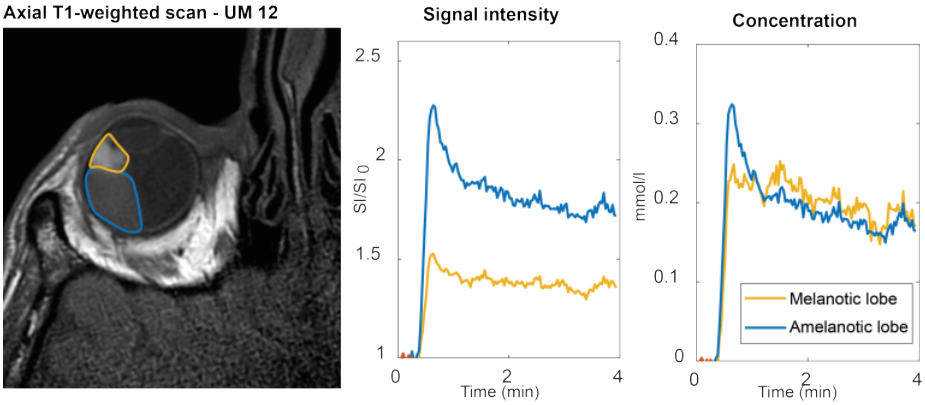

Figure 6.5: The effect of T_1 on the signal intensity
Bilobar lesion with both an amelanotic and a melanotic lobe. The amelanotic part of the lesion appears to be enhancing stronger than the melanotic part. When, however, the actual T_1 was included in the calculation of the contrast agent concentration, a very similar concentration was found in both lesions, although still a distinct difference was present in the early timepoints.

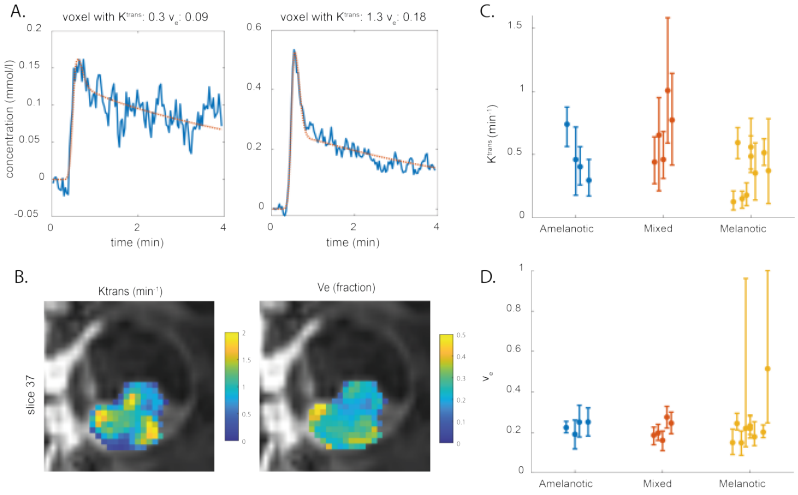

Figure 6.6: Pharmacokinetic modelling results
(A) Concentration curve and fit of two voxels of patient 10 showing the inhomogeneity of the lesion. (B) A sagittal slice of UM patient 10 showing K^{trans} and v_e maps showing an inhomogeneous values of K^{trans} and v_e in the lesion. (C&D). The median and IQR of the K^{trans} and v_e in the lesion. All patients except one UM had a v_e lower than 0.3.

6.4 Discussion

Recent developments in ocular MR-imaging allow for the acquisition of DCE-images with sufficient temporal and spatial resolution to perform DCE-MRI in the eye, as the currently achievable isotropic spatial resolution of 1 mm is sufficient to assess the smaller intraocular lesions, while the 2 s temporal resolution yields more than sufficient time points to determine the inflow characteristics of the lesion[19]. With this improved protocol, DCE-MRI was performed in 19 intraocular lesions and the effect of eye specific challenges on the quantification was investigated.

As the eye can rotate within the head, registering the complete Field-of-View(FOV) of all time points is not sufficient to correct for eye motion. Therefore a dedicated registration method was developed to mitigate the effect of gazing variations on the measured concentration curve. These corrections resulted in absolute changes in K^{trans} up to 0.25 min^{-1}. Although rigid registration of the complete FOV has been proposed to correct for motion of intraocular lesions[21], we proved with our experiments that it is not sufficient, since the eye moves within the head. We showed that masked-registration improved the quality of the curves significantly, however, still the quality of 15% of the concentration curves was scored as insufficient to perform an automatic fit on. Smaller lesions had a higher percentage of insufficient quality voxels indicating that our registration cannot fully resolve effects of motion at the edge of the lesion. In 4% ($n = 10/285$) of the curves, across different subjects and tumour sizes, registration seemed to have deteriorated the quality at some timepoints although the deterioration was minor compared to the improvement by the registration in the other voxels. This mostly occurred at the edge of the tumour and might be attributed to partial volume effects, although inhomogeneities in the tumour might play a role as well. A MRI-protocol with an increased resolution might therefore also be favourable to decrease the effect of these residual errors in the registration. Although cued blinking might be implemented to reduce motion during acquisition, the resulting twofold reduction in temporal resolution will likely not be beneficial for the pharmacokinetic modelling[8,9]. It might be beneficial to register all scans to the higher resolution $3DT_1$gd instead of one of the dynamic timepoints.

Only one paper[21] was found that used T_1 -mapping for the quantitative DCE analysis of ocular lesions. We found a significant difference in T_1 between melanotic and amelanotic lesions and a strong effect on the quantification indicating that T_1 -mapping is a crucial step in DCE quantification. We therefore recommend to include the actual T_1 in the analysis of DCE of ocular lesions to prevent the bias introduced by the amount of melanin in the tumour. The effect of melanin can be seen clearly in patients with a bilobar lesion, as shown in figure 5. A similar effect was observed between lesions, where amelanotic lesions appears to enhance more than melanotic lesions. This was, however, primarily the result of its longer T_1 and not of an increased contrast agent concentration.

Finally, our results indicate that registration and $B_1{}^+$-correction are important steps in the quantitative analysis of ocular DCE, but these steps affect the pharmacokinetic

parameters to a lesser extent than the differences in T_1 , and are independent of the type of lesion. DCE scans are clinically often evaluated by assessing the Time Intensity Curves (TIC), instead of the actual gadolinium concentration which can be calculated from these intensities[17–20]. However, by comparing these TICs between lesions, the potential differences in T_1 between these lesions are ignored, which can lead to erroneous interpretation of the data. A higher (maximum) relative enhancement or area under the curve might, for example, be interpreted as an increased perfusion in the lesion, but might actually be the result of a less pigmented lesion which has therefore a higher T_1. As the overall shape of the TIC is not affected by the scaling effect of the T_1, a classification based on the curve pattern can still be useful when only the signal intensity is available.[35,36]

In line with earlier genetic and pathology studies,[37–40] our results indicate that uveal melanomas are inhomogeneous, making a voxel wise volumetric assessment of ocular lesions preferred over a single 2D ROI analysis. The relatively thick slices of 3 mm used in the study of Kamrava[21], likely still resulted in representative sample of the lesion, due to averaging in the slice-direction, resulting in the observed correlation between monosomy 3 and Ktrans. However, a lower resolution limits the possibility for motion correction and analysis of small intraocular lesions, making a higher resolution with a voxel wise analysis preferred. Overall, ROI based (semi-)quantitative DCE-MRI analysis without T_1 -mapping for ocular lesions is not recommended as this would result in a significant bias as most DCE measures are dependent on the baseline T_1.

There are areas in which ocular DCE can be further improved. First of all, the flip angle of the DCE-MRI acquisition was 5 degrees for the first eight patients and 13 degrees for subsequent patients. For the determination of reference PKM values of lesions a standardized protocol should be used for all patients. On the hardware side, a multichannel eye-coil[41,42] might result in multiple advances in ocular DCE. An increased channel count might not only enable an increased temporal or spatial resolution, but also a potential larger FOV which can be used to determine the AIF on a patient-specific level. As with the single loop-coil approach no major blood vessels were available within the FOV, we relied on a population based AIF. Population based AIFs are a widely used approach but result a less accurate estimation of especially K^{trans} as the AIF is be influenced by body mass and cardiac output[43,44]. Eye muscles were investigated as reference tissue, but the perfusion of the eye muscles appeared not to be consistent within a single subject and might be also influenced by lesion location and therefore unreliable.

Although the spatial and temporal resolution achieved with our protocol are high compared to other ocular DCE studies, the spatial resolution of $1.25 \times 1.5 \times 1.5$ m^3 is still a limiting factor for small ocular lesions. The smallest lesion included in this study was 32 voxels. A higher resolution would be preferred as this allows for the edge voxels to be removed from the analysis, as the results from these voxels are less reliable due to partial volume effects, not only of the dynamic scan, but also in the T_1-mapping. Therefore, for the current resolution, DCE-MRI of small lesions small lesions (i.e. thickness < 2 mm) is likely less accurate. In situations where the

conditions are less optimal (e.g. no orbital coil is or only a 1.5 T MRI is present) DCE-MRI of intraocular lesions could be performed, although the decrease in image resolution would increase the lesion size required for reliable results. Moreover, although the TWIST-sequence successfully reduces the motion artefacts by reducing the acquisition time per dynamic, the effective spatial resolution for rapidly changing concentrations, in particular the inflow of the contrast agent, might be lower. Nevertheless, the effect of precision errors in analysis steps, such as T_1 determination or registration, on the obtained pharmacokinetic parameters generally showed to be less than 5%. Furthermore, some choices in the proposed analysis pipeline might benefit from a more thorough evaluation to further improve the analysis, such as the optimal reference image for the registration, the potential benefit of applying the median filter to the source FA-series images instead of the resulting T_1-map and other PK-models, such as the extended Tofts model to include a vascular component[45]. Finally, it is important to assess the reproducibility of DCE-MRI for ocular lesions between visits and centers.

Some of the proposed steps to enable reliably ocular DCE-MRI, such as the eye-specific registration, might be less easily incorporated into clinical practice. However, the inclusion of differences in T_1 between lesions in the analysis, which has the strongest effect on the PK-measures, is available in various clinical software packages. Although the elementary TIC-classification, eg. a distinction between a washout and plateau curve, is not affected by the T_1, other elementary measures, in particular the relative enhancement, are significantly affected. Clinically, this conversion to concentration is particularly important as conversely to UM, the majority of other intraocular lesions are non-pigmented, resulting a biased evaluation. When the pharmacokinetic parameters have been determined in a larger cohort of patients with intraocular lesions, they could aid to differentiate between benign and different malignant intraocular lesions. Although the eye specific motion correction is currently not available clinically, head motion can still be corrected with regular registration methods. When only this form of registration is available, a careful evaluation of the individual data is needed to screen for motion and to potentially remove motion-corrupted time points. We anticipate that this approach will be clinically sufficient to aid in the differential diagnosis, especially as other information, such as DWI, can be included in the considerations. This research furthermore showed that some UM are inhomogeneous in composition. For subsequent studies to assess these inhomogeneities, and assess their potential relation to genetic factors and the patients' prognosis[21], full motion correction will be needed, as these inhomogeneities can amplify the effect of eye motion on the final parameters.

6.5 Conclusion

Although MRI of eyes is challenging in many aspects, we showed that quantitative DCE-MRI analysis can be performed for intraocular lesions by increasing the temporal and spatial resolution of the dynamic scan and using dedicated registration and T_1-mapping with $B_1{}^+$-correction in the analysis. In the clinic DCE-MRI analysis

might aid in the diagnosis, prognosis and follow-up of intraocular masses.

6.6 References

[1] M. G. Jaarsma-Coes, T. A. Ferreira, P. J. van Houdt, U. A. van der Heide, G. P. Luyten, and J.-W. M. Beenakker, "Eye-specific quantitative dynamic contrast-enhanced mri analysis for patients with intraocular masses," *Magnetic Resonance Materials in Physics, Biology and Medicine*, pp. 1–13, 2021.

[2] IKNL, *NKR cijfers*. [Online]. Available: https://iknl.nl/nkr-cijfers.

[3] S. Kaliki and C. L. Shields, *Uveal melanoma: Relatively rare but deadly cancer*, 2017. DOI: 10.1038/eye.2016.275.

[4] C. L. Shields *et al.*, "Metastasis of uveal melanoma millimeter-by-millimeter in 8033 consecutive eyes," *Archives of Ophthalmology*, vol. 127, no. 8, pp. 989–998, 2009, ISSN: 00039950. DOI: 10.1001/archophthalmol.2009.208.

[5] I. D. Fabian and M. S. Sagoo, "Understanding retinoblastoma: epidemiology and genetics," *Community eye health*, vol. 31, no. 101, p. 7, 2018, ISSN: 0953-6833.

[6] V. M. Cohen, "Ocular metastases," in *Eye (Basingstoke)*, 2013. DOI: 10.1038/eye.2012.252.

[7] C. L. Shields *et al.*, "Choroidal nevus transformation into melanoma: Analysis of 2514 consecutive cases," *Archives of Ophthalmology*, 2009, ISSN: 00039950. DOI: 10.1001/archophthalmol.2009.151.

[8] J. W. Beenakker, G. A. van Rijn, G. P. Luyten, and A. G. Webb, "High-resolution MRI of uveal melanoma using a microcoil phased array at 7 T," *NMR in Biomedicine*, 2013, ISSN: 09523480. DOI: 10.1002/nbm.3041.

[9] B. A. Berkowitz, C. McDonald, Y. Ito, P. S. Tofts, Z. Latif, and J. Gross, "Measuring the human retinal oxygenation response to a hyperoxic challenge using MRI: Eliminating blinking artifacts and demonstrating proof of concept," *Magnetic Resonance in Medicine*, vol. 46, no. 2, pp. 412–416, 2001, ISSN: 07403194. DOI: 10.1002/mrm.1206.

[10] T. Niendorf *et al.*, *Ophthalmic Magnetic Resonance Imaging: Where Are We (Heading To)?* 2021. DOI: 10.1080/02713683.2021.1874021.

[11] T. Ferreira *et al.*, "MR and CT Imaging of the Normal Eyelid and its Application in Eyelid Tumors," *Cancers*, vol. 12, p. 658, Mar. 2020. DOI: 10.3390/cancers12030658.

[12] K. R. Keene *et al.*, "The feasibility of quantitative MRI of extra-ocular muscles in myasthenia gravis and Graves' orbitopathy," eng, *NMR in biomedicine*, vol. 34, no. 1, e4407–e4407, Jan. 2021, ISSN: 1099-1492. DOI: 10.1002/nbm.4407. [Online]. Available: https://pubmed.ncbi.nlm.nih.gov/32893386%20https://www.ncbi.nlm.nih.gov/pmc/articles/PMC7757175/.

[13] L. van Vught, D. P. Shamonin, G. P. Luyten, B. C. Stoel, and J.-W. M. Beenakker, "MRI-based 3D retinal shape determination," *[submitted]*, 2021.

[14] J. W. M. Beenakker *et al.*, "Clinical evaluation of ultra-high-field MRI for three-dimensional visualisation of tumour size in uveal melanoma patients, with direct relevance to treatment planning," *Magnetic Resonance Materials in Physics, Biology and Medicine*, vol. 29, no. 3, pp. 571–577, 2016, ISSN: 13528661. DOI: 10.1007/s10334-016-0529-4.

[15] E. Fleury *et al.*, "3D MRI-based treatment planning approach for non-invasive ocular proton therapy," *Medical Physics*, 2020, ISSN: 0094-2405.

[16] P. V. Foti *et al.*, "Uveal melanoma: quantitative evaluation of diffusion-weighted MR imaging in the response assessment after proton-beam therapy, long-term follow-up," *Radiologia Medica*, 2017, ISSN: 18266983. DOI: 10.1007/s11547-016-0697-3.

[17] X. Jiang *et al.*, "Dynamic contrast-enhanced MRI of ocular melanoma," *Melanoma Research*, 2015, ISSN: 14735636. DOI: 10.1097/CMR.0000000000000142.

[18] W. Wei *et al.*, "Dynamic Contrast-Enhanced Magnetic Resonance Imaging of Ocular Melanoma as a Tool to Predict Metastatic Potential," *Journal of Computer Assisted Tomography*, 2017, ISSN: 15323145. DOI: 10.1097/RCT.0000000000000598.

[19] T. A. Ferreira, L. G. Fonk, M. G. Jaarsma-Coes, G. G. van Haren, M. Marinkovic, and J. W. M. Beenakker, "MRI of uveal melanoma," *Cancers*, vol. 11, no. 3, pp. 1–20, 2019, ISSN: 20726694. DOI: 10.3390/cancers11030377.

[20] F. Rodjan *et al.*, "Retinoblastoma: Value of dynamic contrast-enhanced MR imaging and correlation with tumor angiogenesis," *American Journal of Neuroradiology*, 2012, ISSN: 01956108. DOI: 10.3174/ajnr.A3119.

[21] M. Kamrava *et al.*, "Quantitative multiparametric MRI in uveal melanoma: increased tumor permeability may predict monosomy 3," *Neuroradiology*, vol. 57, no. 8, pp. 833–840, 2015, ISSN: 14321920. DOI: 10.1007/s00234-015-1546-0.

[22] M. Y. Chang, N. P. Rao, B. L. Burgess, L. Johnson, and T. A. Mccannel, "Heterogeneity of monosomy 3 in fine needle aspiration biopsy of choroidal melanoma," *Molecular Vision*, 2013, ISSN: 10900535.

[23] J. L. Chien, K. Sioufi, T. Surakiatchanukul, J. A. Shields, and C. L. Shields, *Choroidal nevus: A review of prevalence, features, genetics, risks, and outcomes*, 2017. DOI: 10.1097/ICU.0000000000000361.

[24] W. S. Enochs, P. Petherick, A. Bogdanova, U. Mohr, and R. Weissleder, "Paramagnetic metal scavenging by melanin: MR imaging," *Radiology*, 1997, ISSN: 00338419. DOI: 10.1148/radiology.204.2.9240529.

[25] L. A. Tudorica *et al.*, "A feasible high spatiotemporal resolution breast DCE-MRI protocol for clinical settings," *Magnetic Resonance Imaging*, 2012, ISSN: 0730725X. DOI: 10.1016/j.mri.2012.04.009.

[26] E. D. Baron, M. Di Nicola, and C. L. Shields, *Updated ajcc classification for posterior uveal melanoma: A case example of a patient with choroidal melanoma is discussed in light of the latest edition of this cancer staging manual*, 2018.

[27] D. De Naeyer, J. Verhulst, W. Ceelen, P. Segers, Y. De Deene, and P. Verdonck, "Flip angle optimization for dynamic contrast-enhanced mri-studies with spoiled gradient echo pulse sequences," *Physics in Medicine & Biology*, vol. 56, no. 16, p. 5373, 2011.

[28] K. Nehrke and P. Börnert, "DREAM-a novel approach for robust, ultrafast, multislice B1 mapping," *Magnetic Resonance in Medicine*, 2012, ISSN: 07403194. DOI: 10.1002/mrm.24158.

[29] P. S. Tofts, "T1-weighted DCE imaging concepts: modelling, acquisition and analysis," *signal*, vol. 500, no. 450, p. 400, 2010.

[30] F. Ritter *et al.*, "Medical Image Analysis: A Visual Approach," *IEEE Pulse*, vol. 2, no. 6, pp. 60–70, 2011, ISSN: 2154-2287. DOI: 10.1109/MPUL.2011.942929. [Online]. Available: http://ieeexplore.ieee.org/xpls/abs_all.jsp?arnumber=6088923&tag=1.

[31] P. A. Yushkevich *et al.*, "User-guided 3D active contour segmentation of anatomical structures: significantly improved efficiency and reliability," *Neuroimage*, vol. 31, no. 3, pp. 1116–1128, 2006, ISSN: 1053-8119.

[32] E. K. Fram *et al.*, "Rapid calculation of T1 using variable flip angle gradient refocused imaging," *Magnetic Resonance Imaging*, 1987, ISSN: 0730725X. DOI: 10.1016/0730-725X(87)90021-X.

[33] R. K. Gupta, "A new look at the method of variable nutation angle for the measurement of spin-lattice relaxation times using fourier transform NMR," *Journal of Magnetic Resonance (1969)*, 1977, ISSN: 00222364. DOI: 10.1016/0022-2364(77)90138-X.

[34] K. Koolstra, J. W. M. Beenakker, P. Koken, A. Webb, and P. Börnert, "Cartesian MR fingerprinting in the eye at 7T using compressed sensing and matrix completion-based reconstructions," *Magnetic Resonance in Medicine*, 2019, ISSN: 15222594. DOI: 10.1002/mrm.27594.

[35] S. R. Ro, P. Asbach, E. Siebert, E. Bertelmann, B. Hamm, and K. Erb-Eigner, "Characterization of orbital masses by multiparametric MRI," *European Journal of Radiology*, 2016, ISSN: 18727727. DOI: 10.1016/j.ejrad.2015.11.041.

[36] Y. Yuan, X. P. Kuai, X. S. Chen, and X. F. Tao, "Assessment of dynamic contrast-enhanced magnetic resonance imaging in the differentiation of malignant from benign orbital masses," *European Journal of Radiology*, 2013, ISSN: 0720048X. DOI: 10.1016/j.ejrad.2013.03.001.

[37] K. G. Griewank and R. Murali, "Pathology and genetics of uveal melanoma," *Pathology - Journal of the RCPA*, vol. 45, no. 1, 2013, ISSN: 0031-3025. [Online]. Available: https://journals.lww.com/pathologyrcpa/Fulltext/2013/01000/Pathology_and_genetics_of_uveal_melanoma.3.aspx.

[38] W. Maat *et al.*, "The Heterogeneous Distribution of Monosomy 3 in Uveal Melanomas: Implications for Prognostication Based on Fine-Needle Aspiration Biopsies," *Archives of Pathology & Laboratory Medicine*, vol. 131, no. 1, pp. 91–96, Jan. 2007, ISSN: 0003-9985. DOI: 10.5858/2007-131-91-THDOMI. [Online]. Available: https://doi.org/10.5858/2007-131-91-THDOMI.

[39] A. K. Miller, M. J. Benage, D. J. Wilson, and A. H. Skalet, "Uveal Melanoma with Histopathologic Intratumoral Heterogeneity Associated with Gene Expression Profile Discordance," eng, *Ocular oncology and pathology*, vol. 3, no. 2, pp. 156–160, Jul. 2017, ISSN: 2296-4681. DOI: 10.1159/000453616. [Online]. Available: https://pubmed.ncbi.nlm.nih.gov/28868288%20https://www.ncbi.nlm.nih.gov/pmc/articles/PMC5566757/.

[40] I. W. McLean, W. D. Foster, L. E. Zimmerman, and J. W. Gamel, "Modifications of Callender's classification of uveal melanoma at the Armed Forces Institute of Pathology," *American journal of ophthalmology*, vol. 96, no. 4, pp. 502–509, 1983, ISSN: 0002-9394.

[41] A. Graessl *et al.*, "Ophthalmic magnetic resonance imaging at 7 T using a 6-channel transceiver radiofrequency coil array in healthy subjects and patients with intraocular masses," *Investigative radiology*, vol. 49, no. 5, pp. 260–270, 2014, ISSN: 0020-9996.

[42] R. K. Glarin *et al.*, "MR-EYE: High-Resolution MRI of the Human Eye and Orbit at Ultrahigh Field (7T)," *Magnetic Resonance Imaging Clinics of North America*, vol. 29, no. 1, pp. 103–116, 2021, ISSN: 1064-9689. DOI: https://doi.org/10.1016/j.mric.2020.09.004. [Online]. Available: https://www.sciencedirect.com/science/article/pii/S1064968920300696.

[43] A. Fedorov *et al.*, "A comparison of two methods for estimating DCE-MRI parameters via individual and cohort based AIFs in prostate cancer: A step towards practical implementation," *Magnetic Resonance Imaging*, 2014, ISSN: 18735894. DOI: 10.1016/j.mri.2014.01.004.

[44] G. J. Parker *et al.*, "Experimentally-derived functional form for a population-averaged high-temporal-resolution arterial input function for dynamic contrast-enhanced MRI," *Magnetic Resonance in Medicine*, 2006, ISSN: 07403194. DOI: 10.1002/mrm.21066.

[45] S. P. Sourbron and D. L. Buckley, "On the scope and interpretation of the Tofts models for DCE-MRI," *Magnetic Resonance in Medicine*, 2011, ISSN: 07403194. DOI: 10.1002/mrm.22861.

7

General discussion

This thesis is part of the Protons4Vision project which aims to improve the accuracy of proton beam therapy and ultimately save the patients vision without the need for surgergical marker placement. At the start of this thesis, ocular MRI was not yet performed regularly in a clinically setting. In the LUMC ocular MRI was mostly performed in a research setting on the ultra-high field MRI scanner. This work contributed to transitioning ocular MRI from the research setting towards the clinic without loss of image quality[1]. Through our collaboration with Philips, this protocol[2,3] is now available worldwide for all their clinical 3T scanners[4]. At the LUMC, ocular MRI is currently contributing to the diagnosis, more accurate ocular PT planning (**chapter 4**) and/or follow-up in over three patients every week.

As part of the protons4vision project, MRI scans have been used by Kilany Hassan to develop an semi-automatic segmentation pipeline to create an MRI based tumour and eye model that can be used for treatment planning[5]. The sclera, cornea, lens, vitreous body, retinal detachment and tumour can be segmented on co-registered T1- and T2-weighted images and subsequently be used to create a eye and tumour model. I used an adapted version of this segmentation technique in (**chapter 2**) to show that the eye and tumour shape does not change between scanning and treatment position.

In **chapter 3** I showed that MRI based GTV delineation has a low observer variation of 0.4mm. This uncertainty in the GTV definition is needed to determine the margin needed for MRI based ocular PT planning systems such as the dose engine developed as part of the protons4vision project[6] by Emmanuelle Fleury. This dose engine calculates the optimal gaze-angle by finding the optimal trade-off between maximizing the tumour dose and limitation of the dose to the organs at risk. Unfortunately, the normal tissue complication probability of organs-at-risk such as the retina are not yet known. This should be known before this dose engine can create clinical relevant optimal gaze-angle estimations.

7.1 Ocular MRI from a ophthalmology perspective

My work and work from and with colleges has contributed to the acceptance of MRI in ocular oncology[7]. In the second part of this discussion I would like to reflect on this work and the work of others, to highlight possible applications for ocular MRI in clinical practise.

7.1.1 Differential diagnosis

Conventional ophthalmic imaging such as ultrasound and fundoscopy is generally sufficient to differentiate UM from other intraocular masses[8,9], although in some cases not all criteria can be evaluated due to the size and/or location of the tumour or presence of opaque media such as cataract, vitreous haemorrhage or massive choroidal effusion. In these cases MRI can be used to assess different aspect of the tumour such as its origin, signal intensity and functional imaging. Although, prospective studies regarding the accuracy of MR-based differential diagnosis of

intraocular masses are lacking, several studies and case reports already provide clear indications of its value for current patients[2,3,10–13].

Based on only anatomical information, such as location, origin and signal intensity from MRI, RPE adenoma's[14], neurofibroma[15] and other types of intraocular lesions[16–31] can be differentiated. However, the appearance on MRI can also be inconclusive for example in the diagnosis of leiomyoma[32,33], lymphoma[34] and differentiation between UM and intraocular metastasis[13,35]. It is therefore recommended to include functional imaging such as DWI[2,3,11,36–40] and PWI[3,41,42] to assess whether the biological characteristics match those of UM[43].

Schwannomas for example, can have similar signal intensities as (amelanotic) UM[26]. In contrast to UM, lesions can be inhomogeneous on T2 and/or show heterogeneous enhancement[17,27,35]. Moreover, in schwannomas progressive time intensity curve have been found[27] in contrast to UMs. Similarly, lymphomas can be difficult to differentiate from UM based on signal intensity alone[34], however, a lower apparent diffusion coefficient (ADC) might help to differentiate a lymphoma from UM[40].

It is important to acknowledge that not all radiological characteristics of the lesions in the differential diagnosis of UM are known, nor have a 100% specificity (figure 7.1), therefore definite diagnoses based on MRI alone can be challenging. If one or more atypical features are present in a tumour an MRI could be requested. MRI can provide detailed information on tumour localization, the layer of origin, tumour extension and perfusion[2,3] (**chapter 3,4,5,6**). In our experience this information can provide important information for the diagnosis or substantiates a (risky) biopsy especially when combined with ophthalmic imaging. However, we also found that there is a learning curve. The radiologist needs to get experience with MRI of intraocular masses and ophthalmologists need to grow in confidence in the radiologist. Having a multidisciplinary meeting discussing the MRI's can help grow understanding and confidence from both sides. Moreover, we found that providing the radiologists with a clear question on the MRI request and adding relevant clinical information is very important to help focus the assessment of the images and formulate a relevant conclusion. For example, if there is doubt between specific diagnoses it would be helpful to provide these diagnoses options as MRI might be able to rule out one of the two.

7.1.2 Therapy planning

Size is important for determination of the optimal treatment and therapy planning. For conventional radiotherapy planning of these tumours, 2D tumour dimensions are used[45]. MRI, however, provides volumetric imaging allowing tumour measurements in all possible angles, which can help to provide a better determination of the tumour prominence[2]. In general, there is an agreement between ultrasound and MRI[3]. However, for large and anterior located tumours MRI was considered more reliable **(chapter 4)**. An analysis of 72 patients, from different studies I participated in, confirmed these findings. Ultrasound measurements were slightly larger than MRI ($p<0.01$, Prominence; median 6.3mm vs 6.1mm and largest basal diameter (LBD);

A.

TIC shape	Progressive	Plateau	Wash-out
UM	0	14	31
Lymphoma	0	6	6
Benign	26	13	4

Peak intensity			
UM (n=42)	1.62±0.42	Ferreira	
UM (n=12)	1.53±0.29	Buerk	
Benign (n=3)	1.14±0.06	Buerk	

B.

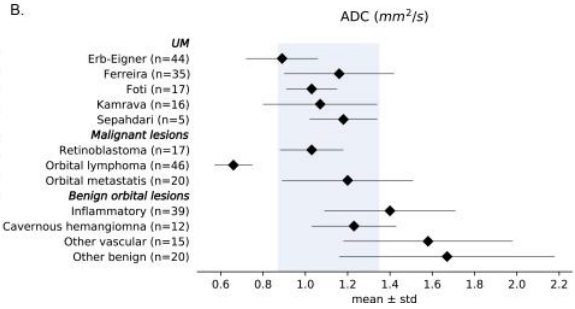

Figure 7.1: (A) UM's generally show a wash-out curve whereas most benign lesions have a progressive curve. Lesions with a plateau curve can be eighter benign or malignant. [3, 41, 42] According to Ferreira and Buerk the peak intensity of a UM is around 1.6 [3, 44]. (B) The ADC value of UM is 1.11±0.24 x10-3 mm2/s (grey area) which is lower than most benign orbital lesions and higher than orbital lymphoma. [3, 11, 37–40]

14.7mm vs 14.0mm). The unreliable ultrasound measurements occurred more often in anterior tumours compared to posterior tumours (73% vs 27%, $p<0.001$), figure 7.2C. Therefore when there is doubt about tumour dimensions and small change in size could change optimal treatment or treatment is planned based on the tumour dimensions, an MRI is recommended.

The second advantage of MRI over ultrasound is that entire orbit is imaged, allowing for assessment of the relation between tumour and different organs at risk. For patients undergoing brachytherapy, MRI might be used for verification of plaque position[46,47]. MRI might also add information to the conventional model based treatment planning especially for measurements of the axial length and distance between tantalum markers and tumour in certain types of tumours **(chapter 4)**. Moreover, it has been shown in that the inter-observer variation in the delineation of uveal melanoma is low with respect to other tumours and ultrasound **(chapter 3)**. Even though MRI based treatment planning has been investigated, it is not yet readily available in clinical practice[48–54]. On the other hand, planning systems such as OCTOPUS and RayOcular have become available and enable incorporation of MRI based information into the traditional model based treatment planning[55–58]. Importantly, it has been shown that MRI can be performed safely and reliable even with surgically placed markers and regardless of tumour and head orientation[59–61] **(chapter 2)**.

7.1.3 Follow-up

In our experience it is very important to provide patients with information about treatment response as early as possible. MRI provides the opportunity for this early treatment response monitoring especially in patients after proton beam therapy as these tumours have been shown to slowly decrease in size.

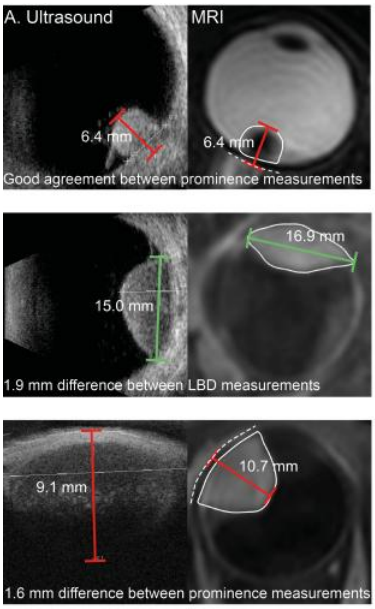

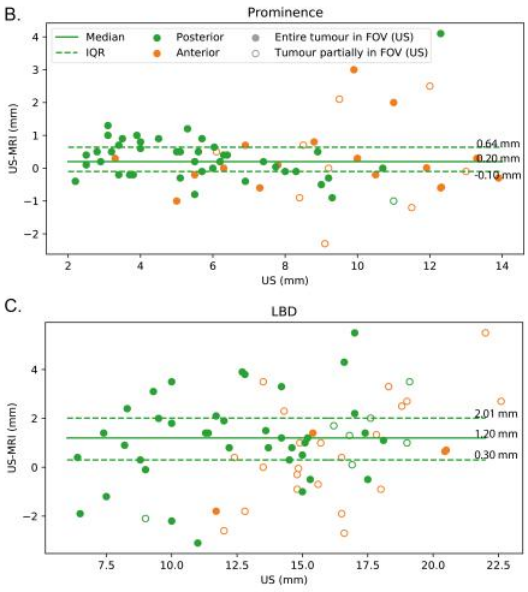

D. Absolute difference between US & MRI (mm)	median (75th percentile)	p-value
Prominence		
Posterior	0.5 (0.8)	0.31
Anterior	0.6 (1.0)	
LBD		
Posterior	1.4 (2.2)	0.20
Anterior	1.4 (2.6)	

E.	full in FOV	part in FOV	p-value (OR)	Small	Large	p-value (OR)
Prominence						
Posterior	44	1	<0.001 (0.05)	42	3	0.003 (0.12)
Anterior	18	9		17	10	
LBD						
Posterior	38	7	<0.001 (0.03)	33	12	0.13 (0.45)
Anterior	4	22		15	12	

Figure 7.2: Difference between tumour dimensions measured on US and MRI. (A) Typical examples of US and MRI measurements adopted with permission from Klaassen et al. (B,C) Difference between US and MRI with posterior tumours in green and anterior tumours in orange. The median and the inter quartile range (IQR) for the difference between MRI and US measurements is visualized for patients with an posterior tumour. (D) The prominence and LBD measurements were larger on US (Wilcoxon signed-rank test, $p<0.01$). Anterior tumours had a higher absolute difference between US and MRI for the prominence measurement. The difference in LBD is less clear. (E) Anterior tumours were more often only partially imaged. Small tumours were defined as prominence <10mm or LBD < 16mm. FOV: Field of view

The follow-up of patients after treatment for UM is primarily focused on the reduction in tumour volume or prominence. In proton therapy however, the reduction in size, measured with ultrasound, is slow and in over 5% of the patients the tumour increases in size in the first 6-12 months[62]. Other disadvantages are the large inter-observer variation (0.3-0.6mm[63,64]) with respect to size reduction and the challenge to find the same plane as previous measurements.

Several studies showed decrease in tumour size using MRI following treatment[65–67]. Together with Michael Tang and other LUMC colleagues we compared MRI and ultrasound based measurements for proton beam therapy and brachytherapy patients. This study found that the measurements between ultrasound and MRI are comparable. Although it was found that ultrasound overestimated the tumour prominence in some patient at 3 and 6 month post treatment due to treatment related effects.

Functional imaging showed changes earlier than size and therefore allows for early treatment response monitoring[11,68]. We have shown a wash-out decrease in the majority of patients as early as 3 month after treatment (figure 1.4). It would be interesting to further quantify these changes using the method proposed in **chapter 6**. The diffusion within the tumour has shown to increase after proton beam therapy and brachytherapy[11,68,69]. Due to the large variation however, DWI might not be a useful biomarker between patients.

Finally, retinal detachment, a common complication after proton beam therapy is often treated with a vitrectomy with silicon oil tamponade. Unfortunately ultrasound imaging is hindered in these patients. Follow-up with MRI is possible after minor adjustments in the imaging protocols **(chapter 5)**. It is important to keep in mind that for treatment response monitoring also a pre-treatment MRI is needed.

7.2 Future perspectives

With the field of ocular MRI still moving forward the possibilities and indications for ocular MRI will most likely increase. First of all, more and more patients receiving ocular PT will get an MRI. In **(chapter 4)** I showed how MRI can contribute to conventional model based ocular PT planning and we see more and more centres starting to perform MRI for this patient group. There are however prospective studies needed to evaluate the effects of MRI on the outcome in these patients. **(Chapter 3)** shows that the uncertainty in the GTV delineation is higher at the sclera edge of the tumour compared to the part of the tumour adjacent to the vitreous. In combination with known differences in uncertainties in the treatment delivery system this could be a starting point to investigate different treatment planning strategies with a margin that varies in different directions. In combination with MRI based treatment planning and the two-beam strategy proposed by Fleury et al[70] this might contribute to reduction in visual impairment after ocular PT.

In this thesis, I have addressed some challenges in the quantification of PWI. We are working together with Philips to implement $B_1{}^+$ mapping and masked registration

into the DCE-MRI analysis software as recommended in **chapter 6**. Implementation of the analysis into clinical software will make quantitative functional MRI more easily available in clinical practice as it currently is a complicate and time consuming process using mostly in-house developed software. Besides implementation in the clinic, additional research in larger cohorts is needed to determine the perfusion characteristics of UM and other intraocular masses. Analysis of a large uveal melanoma cohort is needed in order to determine the expected values in uveal melanoma. It would be valuable to have similar studies to determine the anatomical and functional features of other intraocular masses to further improve the value of MRI in the differential diagnosis of intraocular masses. Moreover, a study is needed on patients with histology and a long follow-up period in order to investigate the possible prognostic value of PWI-MRI as there are already some indications that tumour perfusion can be related to monosomy 3, an important genetic marker for metastatic risk[3,39]. Finally, the first effective treatments for metastatic uveal melanoma are now becoming available[71]. These and other therapies could also be used as (neo)adjuvant treatments for high risk patients. Quantitative PWI analysis could play a role as a non invasive alternative to a biopsy in order to identify high-risk patients that might benefit from these (neo)adjuvant treatments.

With the growing patient population and increasing cost from expensive medicines and high-tech solutions it is important to provide evidence on the cost effectiveness of ocular MRI. There are already clear indications that ocular MRI in the clinical care of uveal melanoma patients can be cost effective[72]. This should be investigated more thoroughly for different indications and health care systems.

Finally, during my thesis I experienced that the field of UM research is sometimes fragmented. One of the reasons is that treatment of UM also is fragmented. For example, it can occur that the centre for the diagnosis and the centre for treatment are over 200 km apart. I was very fortunate to be able to work in such a multidisciplinary team with people who are open for ideas and imaging techniques from other disciplines. This helped bridging the gap between disciplines and has led to new MRI sequences and protocols that improved the care for ocular oncology patients.

7.3 References

[1] M. C. Y. Tang *et al.*, "A comparison of 3 t and 7 t mri for the clinical evaluation of uveal melanoma," *J Magn Reson Imaging*, 2021, ISSN: 1053-1807. DOI: 10.1002/jmri.27939.

[2] T. A. Ferreira, L. Grech Fonk, M. G. Jaarsma-Coes, G. G. R. van Haren, M. Marinkovic, and J. M. Beenakker, "Mri of uveal melanoma," *Cancers (Basel)*, vol. 11, no. 3, 2019, ISSN: 2072-6694 (Print) 2072-6694. DOI: 10.3390/cancers11030377.

[3] T. A. Ferreira *et al.*, "Mr imaging characteristics of uveal melanoma with histopathological validation," *Neuroradiology*, 2021, ISSN: 0028-3940. DOI: 10.1007/s00234-021-02825-5.

[4] Philips. "Orbit with melanoma." (), [Online]. Available: https://www.mriclinicalcasemap.philips.com/global/case/264 (visited on 05/15/2022).

[5] M. K. Hassan *et al.*, "An automatic framework to create patient-specific eye models from 3D MR-images for treatment selection in patients with uveal melanoma," *Advances in Radiation Oncology*, p. 100 697, 2021, ISSN: 2452-1094. DOI: https://doi.org/10.1016/j.adro.2021.100697. [Online]. Available: https://www.sciencedirect.com/science/article/pii/S2452109421000555.

[6] E. Fleury *et al.*, "3D MRI-based treatment planning approach for non-invasive ocular proton therapy," *Medical Physics*, 2020, ISSN: 0094-2405.

[7] J.-W. M. Beenakker *et al.*, "Outcome measures of new technologies in uveal melanoma: Review from the european vision institute special interest focus group meeting," *Ophthalmic Research*, 2022.

[8] K. A. Roelofs *et al.*, "The moles system for planning management of melanocytic choroidal tumors: Is it safe?" *Cancers (Basel)*, vol. 12, no. 5, 2020, ISSN: 2072-6694 (Print) 2072-6694. DOI: 10.3390/cancers12051311.

[9] C. L. Shields *et al.*, "Choroidal nevus transformation into melanoma: Analysis of 2514 consecutive cases," *Arch Ophthalmol*, vol. 127, no. 8, pp. 981–7, 2009, ISSN: 0003-9950. DOI: 10.1001/archophthalmol.2009.151.

[10] P. V. Foti *et al.*, "Histopathologic and mr imaging appearance of spontaneous and radiation-induced necrosis in uveal melanomas: Initial results," *Cancers (Basel)*, vol. 14, no. 1, 2022, ISSN: 2072-6694 (Print) 2072-6694. DOI: 10.3390/cancers14010215.

[11] P. V. Foti *et al.*, "Uveal melanoma: Quantitative evaluation of diffusion-weighted mr imaging in the response assessment after proton-beam therapy, long-term follow-up," *Radiol Med*, vol. 122, no. 2, pp. 131–139, 2017, ISSN: 0033-8362. DOI: 10.1007/s11547-016-0697-3.

[12] J. W. Beenakker *et al.*, "Clinical evaluation of ultra-high-field mri for three-dimensional visualisation of tumour size in uveal melanoma patients, with direct relevance to treatment planning," *Magma*, vol. 29, no. 3, pp. 571–7, 2016, ISSN: 0968-5243 (Print) 0968-5243. DOI: 10.1007/s10334-016-0529-4. [Online]. Available: https://www.ncbi.nlm.nih.gov/pmc/articles/PMC4891368/pdf/10334_2016_Article_529.pdf.

[13] A. J. Lemke *et al.*, "Intraocular metastases: Differential diagnosis from uveal melanomas with high-resolution mri using a surface coil," *Eur Radiol*, vol. 11, no. 12, pp. 2593–601, 2001, ISSN: 0938-7994 (Print) 0938-7994. DOI: 10.1007/s003300100936.

[14] Y. Su, X. Xu, W. Wei, and J. Xian, "Using a novel mr imaging sign to differentiate retinal pigment epithelium from uveal melanoma," *Neuroradiology*, vol. 62, no. 3, pp. 347–352, 2020, ISSN: 0028-3940. DOI: 10.1007/s00234-019-02353-3.

[15] W. B. Wei, Y. Jie, J. Mo, and B. Li, "Clinical characteristics and treatment of neurofibroma of the choroid," *Chin Med J (Engl)*, vol. 125, no. 10, pp. 1832–5, 2012, ISSN: 0366-6999.

[16] E. Altun, E. Aribal, E. Toker, and M. S. Oğüt, "Anterior coloboma with macrophthalmos and cyst: Mr findings," *Clin Imaging*, vol. 29, no. 6, pp. 430–3, 2005, ISSN: 0899-7071 (Print) 0899-7071. DOI: 10.1016/j.clinimag.2005.05.001.

[17] R. C. Brennan, M. W. Wilson, S. Kaste, K. J. Helton, and M. B. McCarville, "Us and mri of pediatric ocular masses with histopathological correlation," *Pediatr Radiol*, vol. 42, no. 6, pp. 738–49, 2012, ISSN: 0301-0449 (Print) 0301-0449. DOI: 10.1007/s00247-012-2374-6. [Online]. Available: https://link.springer.com/content/pdf/10.1007/s00247-012-2374-6.pdf.

[18] P. de Graaf *et al.*, "Guidelines for imaging retinoblastoma: Imaging principles and mri standardization," *Pediatr Radiol*, vol. 42, no. 1, pp. 2–14, 2012, ISSN: 0301-0449 (Print) 0301-0449. DOI: 10.1007/s00247-011-2201-5.

[19] R. Mukhija, N. Lomi, S. Kumar, and S. Sen, "Retinoblastoma in an adult: A diagnostic dilemma," *BMJ Case Rep*, vol. 12, no. 10, 2019, ISSN: 1757-790x. DOI: 10.1136/bcr-2019-230537.

[20] L. Zhou, X. H. Zhu, K. Zhang, R. Hu, and F. Myers, "Case report: Adult retinoblastoma progression in 19 months," *Optom Vis Sci*, vol. 97, no. 11, pp. 1010–1016, 2020, ISSN: 1040-5488. DOI: 10.1097/opx.0000000000001602.

[21] R. W. Jansen *et al.*, "Mr imaging features to differentiate retinoblastoma from coats' disease and persistent fetal vasculature," *Cancers (Basel)*, vol. 12, no. 12, 2020, ISSN: 2072-6694 (Print) 2072-6694. DOI: 10.3390/cancers12123592.

[22] H. R. Garner, H. E. Fazzone, and D. E. Meltzer, "Kikuchi-fujimoto disease with bilateral uveitis," *J Radiol Case Rep*, vol. 3, no. 7, pp. 1–6, 2009, ISSN: 1943-0922 (Print) 1943-0922. DOI: 10.3941/jrcr.v3i7.188.

[23] J. C. Iturralde, C. Bianciotto, S. E. Lally, M. Krasnow, and C. L. Shields, "Massive choroidal effusion and painful secondary glaucoma from underlying uveal melanoma," *Graefes Arch Clin Exp Ophthalmol*, vol. 250, no. 4, pp. 627–30, 2012, ISSN: 0721-832x. DOI: 10.1007/s00417-011-1881-8.

[24] C. L. Shields, S. G. Honavar, J. A. Shields, J. Cater, and H. Demirci, "Circumscribed choroidal hemangioma: Clinical manifestations and factors predictive of visual outcome in 200 consecutive cases," *Ophthalmology*, vol. 108, no. 12, pp. 2237–48, 2001, ISSN: 0161-6420 (Print) 0161-6420. DOI: 10.1016/s0161-6420(01)00812-0.

[25] C. Stroszczynski *et al.*, "Choroidal hemangioma: Mr findings and differentiation from uveal melanoma," *AJNR Am J Neuroradiol*, vol. 19, no. 8, pp. 1441–7, 1998, ISSN: 0195-6108 (Print) 0195-6108.

[26] Y. J. Cho *et al.*, "A choroidal schwannoma confirmed by surgical excision," *Korean J Ophthalmol*, vol. 23, no. 1, pp. 49–52, 2009, ISSN: 1011-8942 (Print) 1011-8942. DOI: 10.3341/kjo.2009.23.1.49. [Online]. Available: https://www.ncbi.nlm.nih.gov/pmc/articles/PMC2655748/pdf/kjo-23-49.pdf.

[27] J. Xian *et al.*, "Mr imaging findings of the uveal schwannoma," *AJNR Am J Neuroradiol*, vol. 30, no. 4, pp. 769–73, 2009, ISSN: 0195-6108 (Print) 0195-6108. DOI: 10.3174/ajnr.A1467.

[28] H. Demirci, C. L. Shields, S. G. Honavar, J. A. Shields, and D. S. Bardenstein, "Long-term follow-up of giant nodular posterior scleritis simulating choroidal melanoma," *Arch Ophthalmol*, vol. 118, no. 9, pp. 1290–2, 2000, ISSN: 0003-9950 (Print) 0003-9950. DOI: 10.1001/archopht.118.9.1290.

[29] G. Kranias, C. Tyradellis, T. P. Krebs, and J. J. Augsburger, "Bilateral atypical nodular posterior scleritis," *Eur J Ophthalmol*, vol. 16, no. 4, pp. 614–7, 2006, ISSN: 1120-6721 (Print) 1120-6721. DOI: 10.1177/112067210601600419.

[30] H. Kiratli, "Persistent intraschisis hemorrhage simulating choroidal melanoma," *Jpn J Ophthalmol*, vol. 46, no. 2, pp. 222–5, 2002, ISSN: 0021-5155 (Print) 0021-5155. DOI: 10.1016/s0021-5155(01)00502-0.

[31] P. Singh, S. Sen, M. Banerjee, and R. Meel, "Choroidal melanoma masquerading as orbital cellulitis," *BMJ Case Rep*, vol. 11, no. 1, 2018, ISSN: 1757-790x. DOI: 10.1136/bcr-2018-227486.

[32] K. J. Oh *et al.*, "Mr imaging findings of uveal leiomyoma: Three cases," *AJNR Am J Neuroradiol*, vol. 26, no. 1, pp. 100–3, 2005, ISSN: 0195-6108 (Print) 0195-6108.

[33] M. N. Richter, N. E. Bechrakis, G. Stoltenburg-Didinger, and M. H. Foerster, "Transscleral resection of a ciliary body leiomyoma in a child: Case report and review of the literature," *Graefes Arch Clin Exp Ophthalmol*, vol. 241, no. 11, pp. 953–7, 2003, ISSN: 0721-832X (Print) 0721-832x. DOI: 10.1007/s00417-003-0766-x.

[34] W. Küker, U. Herrlinger, E. Grönewäller, J. M. Rohrbach, and M. Weller, "Ocular manifestation of primary nervous system lymphoma: What can be expected from imaging?" *J Neurol*, vol. 249, no. 12, pp. 1713–6, 2002, ISSN: 0340-5354 (Print) 0340-5354. DOI: 10.1007/s00415-002-0919-6.

[35] A. Mahajan, A. Crum, M. H. Johnson, and M. A. Materin, "Ocular neoplastic disease," *Semin Ultrasound CT MR*, vol. 32, no. 1, pp. 28–37, 2011, ISSN: 0887-2171 (Print) 0887-2171. DOI: 10.1053/j.sult.2010.12.001.

[36] A. R. Sepahdari, V. K. Aakalu, P. Setabutr, M. Shiehmorteza, J. H. Naheedy, and M. F. Mafee, "Indeterminate orbital masses: Restricted diffusion at mr imaging with echo-planar diffusion-weighted imaging predicts malignancy," *Radiology*, vol. 256, no. 2, pp. 554–64, 2010, ISSN: 0033-8419. DOI: 10.1148/radiol.10091956.

[37] P. de Graaf *et al.*, "Single-shot turbo spin-echo diffusion-weighted imaging for retinoblastoma: Initial experience," *AJNR Am J Neuroradiol*, vol. 33, no. 1, pp. 110–8, 2012, ISSN: 0195-6108 (Print) 0195-6108. DOI: 10.3174/ajnr.A2729.

[38] K. Erb-Eigner, G. Willerding, M. Taupitz, B. Hamm, and P. Asbach, "Diffusion-weighted imaging of ocular melanoma," *Invest Radiol*, vol. 48, no. 10, pp. 702–7, 2013, ISSN: 0020-9996. DOI: 10.1097/RLI.0b013e31828eea67.

[39] M. Kamrava *et al.*, "Quantitative multiparametric mri in uveal melanoma: Increased tumor permeability may predict monosomy 3," *Neuroradiology*, vol. 57, no. 8, pp. 833–40, 2015, ISSN: 0028-3940. DOI: 10.1007/s00234-015-1546-0.

[40] A. R. Sepahdari, L. S. Politi, V. K. Aakalu, H. J. Kim, and A. A. Razek, "Diffusion-weighted imaging of orbital masses: Multi-institutional data support a 2-adc threshold model to categorize lesions as benign, malignant, or indeterminate," *AJNR Am J Neuroradiol*, vol. 35, no. 1, pp. 170–5, 2014, ISSN: 0195-6108 (Print) 0195-6108. DOI: 10.3174/ajnr.A3619.

[41] D. J. Li *et al.*, "[comparative analysis on the significances of contrast-enhanced ultrasound and dynamic contrast-enhanced magnetic resonance imaging in uveal melanoma diagnosis]," *Zhonghua Yan Ke Za Zhi*, vol. 54, no. 3, pp. 194–198, 2018, ISSN: 0412-4081 (Print) 0412-4081. DOI: 10.3760/cma.j.issn.0412-4081.2018.03.009.

[42] Y. Yuan, X. P. Kuai, X. S. Chen, and X. F. Tao, "Assessment of dynamic contrast-enhanced magnetic resonance imaging in the differentiation of malignant from benign orbital masses," *Eur J Radiol*, vol. 82, no. 9, pp. 1506–11, 2013, ISSN: 0720-048x. DOI: 10.1016/j.ejrad.2013.03.001.

[43] M. G. Jaarsma-Coes, T. A. Ferreira, G. P. M. Luyten, and J. W. M. Beenakker, "Reaction on "ocular ultrasound versus mri in the detection of extrascleral extension in a patient with choroidal melanoma"," *BMC Ophthalmol*, vol. 19, no. 1, p. 193, 2019, ISSN: 1471-2415. DOI: 10.1186/s12886-019-1206-y.

[44] B. M. Buerk *et al.*, "Vascular perfusion of choroidal melanoma by 3.0 tesla magnetic resonance imaging," *Trans Am Ophthalmol Soc*, vol. 102, 209–15, discussion 215–7, 2004, ISSN: 0065-9533 (Print) 0065-9533.

[45] A. Kacperek, "Protontherapy of eye tumours in the UK: A review of treatment at Clatterbridge," *Applied Radiation and Isotopes*, vol. 67, no. 3, pp. 378–386, 2009, ISSN: 0969-8043. DOI: https://doi.org/10.1016/j.apradiso.2008.06.012. [Online]. Available: https://www.sciencedirect.com/science/article/pii/S0969804308003205.

[46] E. T. Detorakis *et al.*, "Mri and dual-energy ct fusion anatomic imaging in ru-106 ophthalmic brachytherapy," *Brachytherapy*, vol. 20, no. 4, pp. 828–834, 2021, ISSN: 1538-4721. DOI: 10.1016/j.brachy.2021.01.003.

[47] J. E. Zoberi *et al.*, "Mri-based treatment planning and dose delivery verification for intraocular melanoma brachytherapy," *Brachytherapy*, vol. 17, no. 1, pp. 31–39, 2018, ISSN: 1538-4721 (Print) 1538-4721. DOI: 10.1016/j.brachy.2017.07.011. [Online]. Available: https://www.ncbi.nlm.nih.gov/pmc/articles/PMC6366337/pdf/nihms-1516405.pdf.

[48] C. Ciller *et al.*, "Multi-channel mri segmentation of eye structures and tumors using patient-specific features," *PLoS One*, vol. 12, no. 3, e0173900, 2017, ISSN: 1932-6203. DOI: 10.1371/journal.pone.0173900.

[49] I. Daftari, E. Aghaian, J. M. O'Brien, W. Dillon, and T. L. Phillips, "3d mri-based tumor delineation of ocular melanoma and its comparison with conventional techniques," *Med Phys*, vol. 32, no. 11, pp. 3355–62, 2005, ISSN: 0094-2405 (Print) 0094-2405. DOI: 10.1118/1.2068927.

[50] E. Fleury *et al.*, "Three-dimensional mri-based treatment planning approach for non-invasive ocular proton therapy," *Med Phys*, vol. 48, no. 3, pp. 1315–1326, 2021, ISSN: 0094-2405 (Print) 0094-2405. DOI: 10.1002/mp.14665.

[51] S. Marnitz *et al.*, "Proton therapy of uveal melanomas: Intercomparison of mri-based and conventional treatment planning," *Strahlenther Onkol*, vol. 182, no. 7, pp. 395–9, 2006, ISSN: 0179-7158 (Print) 0179-7158. DOI: 10.1007/s00066-006-1512-1.

[52] H. G. Nguyen *et al.*, "Personalized anatomic eye model from t1-weighted volume interpolated gradient echo magnetic resonance imaging of patients with uveal melanoma," *Int J Radiat Oncol Biol Phys*, vol. 102, no. 4, pp. 813–820, 2018, ISSN: 0360-3016. DOI: 10.1016/j.ijrobp.2018.05.004.

[53] I. Seibel *et al.*, "Proton beam irradiation: A safe procedure in postequatorial extraocular extension from uveal melanoma," *Am J Ophthalmol*, vol. 191, pp. 49–53, 2018, ISSN: 0002-9394. DOI: 10.1016/j.ajo.2018.04.006.

[54] R. Via *et al.*, "Potential and pitfalls of 1.5t mri imaging for target volume definition in ocular proton therapy," *Radiother Oncol*, vol. 154, pp. 53–59, 2021, ISSN: 0167-8140. DOI: 10.1016/j.radonc.2020.08.023.

[55] B. Dobler and R. Bendl, "Precise modelling of the eye for proton therapy of intra-ocular tumours," *Phys Med Biol*, vol. 47, no. 4, pp. 593–613, 2002, ISSN: 0031-9155 (Print) 0031-9155. DOI: 10.1088/0031-9155/47/4/304.

[56] F. Hennings, A. Lomax, A. Pica, D. C. Weber, and J. Hrbacek, "Automated treatment planning system for uveal melanomas treated with proton therapy: A proof-of-concept analysis," *Int J Radiat Oncol Biol Phys*, vol. 101, no. 3, pp. 724–731, 2018, ISSN: 0360-3016. DOI: 10.1016/j.ijrobp.2018.02.008.

[57] J. Hrbacek *et al.*, "Practice patterns analysis of ocular proton therapy centers: The international optic survey," *Int J Radiat Oncol Biol Phys*, vol. 95, no. 1, pp. 336–343, 2016, ISSN: 0360-3016. DOI: 10.1016/j.ijrobp.2016.01.040.

[58] Web Page, 2020. [Online]. Available: https://www.raysearchlabs.com/media/press-releases/2020/new-release-of-groundbreaking-treatment-planning-system-raystation-provides-major-advances-for-proton-pbs-monte-carlo-with-gpu.

[59] H. M. Gach *et al.*, "Magnetic resonance imaging metal artifact reduction for eye plaque patient with dental braces," *J Contemp Brachytherapy*, vol. 9, no. 5, pp. 490–495, 2017, ISSN: 1689-832X (Print) 2081-2841. DOI: 10.5114/jcb.2017.71184.

[60] M. G. Jaarsma-Coes *et al.*, "Measuring eye deformation between planning and proton beam therapy position using magnetic resonance imaging," *Phys Imaging Radiat Oncol*, vol. 16, pp. 33–36, 2020, ISSN: 2405-6316. DOI: 10.1016/j.phro.2020.09.010.

[61] E. Oberacker *et al.*, "Magnetic resonance safety and compatibility of tantalum markers used in proton beam therapy for intraocular tumors: A 7.0 tesla study," *Magn Reson Med*, vol. 78, no. 4, pp. 1533–1546, 2017, ISSN: 0740-3194. DOI: 10.1002/mrm.26534.

[62] C. Maschi, J. Thariat, J. Herault, and J. P. Caujolle, "Tumour response in uveal melanomas treated with proton beam therapy," *Clin Oncol (R Coll Radiol)*, vol. 28, no. 3, pp. 198–203, 2016, ISSN: 0936-6555. DOI: 10.1016/j.clon.2015.08.007.

[63] D. H. Char, S. Kroll, R. D. Stone, R. Harrie, and B. Kerman, "Ultrasonographic measurement of uveal melanoma thickness: Interobserver variability," *Br J Ophthalmol*, vol. 74, no. 3, pp. 183–5, 1990, ISSN: 0007-1161 (Print) 0007-1161. DOI: 10.1136/bjo.74.3.183.

[64] C. Haritoglou, A. S. Neubauer, H. Herzum, W. R. Freeman, and A. J. Mueller, "Interobserver and intraobserver variability of measurements of uveal melanomas using standardised echography," *Br J Ophthalmol*, vol. 86, no. 12, pp. 1390–4, 2002, ISSN: 0007-1161 (Print) 0007-1161. DOI: 10.1136/bjo.86.12.1390.

[65] D. W. Kang, S. C. Lee, Y. G. Park, and J. H. Chang, "Long-term results of gamma knife surgery for uveal melanomas," *J Neurosurg*, vol. 117 Suppl, pp. 108–14, 2012, ISSN: 0022-3085. DOI: 10.3171/2012.8.Gks121002.

[66] T. W. Kim *et al.*, "Clinical outcomes of proton beam therapy for choroidal melanoma at a single institute in korea," *Cancer Res Treat*, vol. 50, no. 2, pp. 335–344, 2018, ISSN: 1598-2998 (Print) 1598-2998. DOI: 10.4143/crt.2017.070.

[67] Z. O. Toktas *et al.*, "Gamma knife stereotactic radiosurgery yields good long-term outcomes for low-volume uveal melanomas without intraocular complications," *J Clin Neurosci*, vol. 17, no. 4, pp. 441–5, 2010, ISSN: 0967-5868. DOI: 10.1016/j.jocn.2009.08.004.

[68] A. Russo *et al.*, "Diffusion-weighted magnetic resonance imaging and ultrasound evaluation of choroidal melanomas after proton-beam therapy," *Radiol Med*, vol. 120, no. 7, pp. 634–40, 2015, ISSN: 0033-8362. DOI: 10.1007/s11547-015-0509-1.

[69] F. Bitencourt *et al.*, "Response evaluation of choroidal melanoma after brachytherapy using diffusion-weighted magnetic resonance imaging (dw-mri): Preliminary findings," *Front Oncol*, vol. 10, p. 825, 2020, ISSN: 2234-943X (Print) 2234-943x. DOI: 10.3389/fonc.2020.00825. [Online]. Available: https://www.ncbi.nlm.nih.gov/pmc/articles/PMC7248391/pdf/fonc-10-00825.pdf.

[70] E. Fleury *et al.*, "Improving organs-at-risk sparing for choroidal melanoma patients: A ct-based two-beam strategy in ocular proton therapy with a dedicated eyeline," *Radiotherapy and Oncology*, 2022.

[71] Y. G. Najjar *et al.*, "Ipilimumab plus nivolumab for patients with metastatic uveal melanoma: A multicenter, retrospective study," *Journal for immunotherapy of cancer*, vol. 8, no. 1, 2020.

[72] L. G. Fonk, T. A. Ferreira, A. G. Webb, G. P. Luyten, and J. W. M. Beenakker, "The economic value of mr-imaging for uveal melanoma," *Clinical Ophthalmology*, 2020, ISSN: 11775483. DOI: 10.2147/OPTH.S238405.

Nederlandse samenvatting

In deze thesis onderzoek ik nieuwe manieren om magnetic resonance imaging (MRI) te gebruiken voor het diagnosticeren, behandelen en opvolgen van patiënten met een oogmelanoom. Een oogmelanoom is een kwaadaardige tumor in het oog en ontstaat uit de pigmentcellen van de uvea (iris, het straalvormig lichaam en het vaatvlies). Dit werk richt zich met name op MRI in relatie tot het plannen van protonentherapie. Protonentherapie is een vorm van bestralen waarbij kleine deeltjes (protonen) met een elektrische lading gebruikt worden om kankercellen te vernietigen. Protonentherapie van het oog wordt gepland op basis van oogheelkundige metingen. Met behulp van echo, fundoscopie, biometrie en intra-operatieve metingen wordt een model van het oog en de tumor gemaakt. De ontwikkeling van een MRI-protocol speciaal voor massa's in het oog maakt het nu mogelijk om ook MRI te gebruiken voor het plannen van protonentherapie van het oogmelanoom in drie dimensies.

Omdat protonentherapie van het oog zittend plaats vindt, maar de MRI scans liggend gemaakt worden, is het belangrijk om te kijken of het verschil tussen deze posities invloed heeft op de vorm van het oog en de tumor. In **hoofdstuk 2** heb ik dit onderzocht in zeven gezonde vrijwilligers en zes oogmelanoompatiënten. Deze personen heb ik gescand terwijl ze op de rug in de scanner lagen maar ook terwijl ze met de kin op de borst zaten. Door ze op deze manier te scannen, werkt de zwaartekracht in de zelfde richting als tijdens de protonen bestraling. De ogen en tumoren heb ik op elkaar geregistreerd en vervolgens de afstanden berekend tussen de twee geregistreerde structuren. De mediane afstand was 0.1mm. Daaruit kan geconcludeerd worden dat de vorm van het oog en de tumor niet worden beïnvloed door de positie en dat deze scans gebruikt kunnen worden voor het plannen van protonentherapie van het oog.

Om het oogmelanoom te kunnen bestralen is het belangrijk om te weten waar de tumor precies zit en welke vorm deze precies heeft. Dit kan door de tumor in te tekenen op MRI. Omdat iedereen dit een beetje anders doet is het nodig om de variatie te berekenen tussen de verschillende intekeningen zodat daar bij het plannen van de protoenen therapie rekening mee gehouden kan worden. In **hoofdstuk 3** heb ik onderzocht wat de variatie is in de intekeningen van het melanoom op MRI tussen verschillende intekenaars. Zes artsen vanuit verschillende disciplines hebben de tumor ingetekend met de Big Brother intekensoftware uit Manchester. De MRI-scans zijn gemaakt op een 3T MRI-scanner met een oppervlaktespoel. De tumoren zijn ingetekend op zowel de 3D T1 na contrast (T1gd) als de 3D T2 gewogen scan (T2). Deze MRI-scans hadden een gereconstrueerde isotrope resolutie van 0.3mm. Het verschil in volume en algehele lokale variatie is bepaald voor elke tumor. Daarnaast

is de lokale variatie berekend voor verschillende overgangen zoals de overgang van tumor naar sclera, vitreus, netvliesloslating en vaatvlies. Uit de resultaten blijkt dat de volumes van de tumoren significant groter zijn als deze gesegmenteerd worden op T1gd (0.57cm^3) in vergelijking met T2 (0.51cm^3, p=0.01). De variatie tussen de intekeningen was echter niet groter (T1gd: 0.41mm vs T2: 0.35mm). Er zijn wel significant grotere verschillen gevonden in de variatie tussen intekeningen op T1gd en T2 bij de tumor-vaatvliesovergang (T1gd: 0.62mm en T2: 0.52mm). Het lijkt dat een groter deel van de peri-tumorale aankleuring op T1gd wordt meegenomen en niet op T2 gewogen opnamen, kan ook verklaren waarom de tumorvolumes op T1gd groter zijn ingetekend. In conclusie, de variatie tussen intekeningen is 0.4mm op MRI. Dit is klein, zeker als je het vergelijkt met de voxelafmeting van de MRI-scans (0.8mm isotroop). Het is echter wel aan te raden om de intekeningen op T1 na contrasttoediening te doen omdat tumoruitloop in het vaatvlies mogelijk gemist wordt op T2.

In december 2019 is het HollandPTC gestart met het behandelen van oogmelanoompatiënten met protonentherapie. Omdat MRI-gebaseerd plannen nog niet beschikbaar is voor het oogmelanoom hebben we een MRI-protocol ontwikkeld om de huidige planning, op basis van een geometrich oogmodel, te ondersteunen. In **hoofdstuk 4** wordt het MRI-protocol beschreven en vergelijk ik de tumor- en oogbolafmetingen en de afstand tussen de marker en de tumor gebaseerd op MRI en conventionele methodes. Verschillen tussen de metingen zijn besproken in een multidisciplinaire setting om de oorzaak van de verschillen te bepalen. We hebben gevonden dat in 16 van de 23 patiënten de aanwezigheid van de tumor de conventionele biometriemeting beïnvloed (gemiddelde verschil tussen MRI en biometrie is 0.63mm). In de zeven patiënten met valide biometriemetingen was het verschil 0.18mm. Op basis hiervan lijken MRI-metingen van de aslengte betrouwbaarder te zijn in oogmelanoompatiënten. In negen van de 23 patiënten kon de tumor niet in zijn geheel in beeld worden gebracht met de echo. Dit heeft geleid tot verschillen tussen echo en MRI tot wel 2.3mm voor de prominentie en 5.5mm voor de basale diameter. In de overige patiënten was een goede overeenkomst te zien (gemiddeld verschil van 0.6mm voor prominentie en 1.6mm voor basale diameter). Voor grote en anterieur gelegen tumoren is de MRI-meting waarschijnlijk betrouwbaarder dan de echometing omdat de echo dan niet altijd de tumor geheel in kan beeld brengen . Het verschil tussen MRI en intra-operatieve metingen van de tumor-markerafstand waren in 55% van de gevallen kleiner dan 1mm. Voor anterieur gelegen tumoren en tumoren met een paddenstoelvorm (25% van de markers) hebben we vastgesteld dat de MRI betrouwbaardere metingen geeft. Platte tumoren waren lastig af te grenzen op MRI. In 20/23 patiënten was tenminste één meting ten behoeve van de planning aangeduid als betrouwbaarder dan de conventionele methode. Daarom kunnen we concluderen dat MRI bijdraagt aan het verbeteren van de protonentherapie planning voor het oogmelanoom.

Patiënten met een oogmelanoom krijgen vaak last van netvliesloslating. Soms wordt tijdens de behandeling van netvliesloslating een tumor ontdekt terwijl de netvliesloslating behandeld is met siliconenolie (SiOil). Na deze behandeling blijft de SiOil

in het oog, waardoor het maken van een echo onmogelijk is. Hierdoor wordt de diagnose en behandelplanning van deze patiënten bemoeilijkt. In **hoofdstuk 5** beschrijf ik een MRI-protocol wat is ontwikkeld voor 3T en 7T MRI-scanners voor ogen met SiOil en evalueren we dit bij drie patiënten. De eerste patiënt heeft SiOil gekregen na behandeling waardoor de follow-up niet mogelijk was. Na twee follow-up scans was er geen terugkeer van tumorweefsel te zien. Bij de tweede en derde patiënt was tijdens vitrectomie in een ander ziekenhuis een massa te zien. De MRI-scans zijn gebruikt voor de diagnose en behandelplanning van deze patiënten. Over het algemeen is de voorgestelde workflow ingewikkelder op 7T dan op 3T, omdat de niet-resonantie effecten lineair schalen met de veldsterkte. Hierdoor moet de methode om het magneetveld homogeen te maken aangepast worden op 7T en kan dit automatisch op 3T. Een voordeel van 7T ten opzichte van 3T is de hogere resolutie van de scans (0.6 vs. 0.8 mm). Uit dit hoofdstuk blijkt dat we met het voorgestelde protocol hoge resolutie MRI-afbeeldingen maken van patiënten met SiOil in het oog, waardoor MRI kan bijdragen aan de diagnose, behandelplanning en opvolging van deze oogmelanoompatiënten.

Tenslotte kan MRI naast informatie over de anatomie ook informatie geven over weefseleigenschappen en het functioneren van weefsel. In **hoofdstuk 6** ga ik in op oogspecifieke uitdagingen in de kwantitatieve analyse van perfusiegewogen MRI-scans. In de klinische praktijk wordt kwantitatieve perfusiegewogen MRI nog niet gebruikt omdat het gaat over relatief kleine inhomogene massa's en scans nog last hebben van bewegingsartefacten door hoofd- en oogbeweging tijdens het scannen. We hebben 19 patiënten gedurende vier minuten gescand terwijl contrastmiddel werd toegediend. Het oog werd tijdens de scan elke twee seconde geheel in beeld gebracht. Deze beelden zijn geregistreerd in twee stappen. In de eerste stap werd het hoofd geregistreerd en daarna alleen het oog. Op basis van de berekende T_1 per voxel is de signaalintensiteit omgerekend naar concentratie contrastmiddel. Op deze concentratiecurve heb ik het Tofts model gefit om de weefseleigenschappen K^{trans} en v_e te bepalen. De registratie heeft geleid tot een significante verbetering in de kwaliteit van de concentratiecurves ($p<0.001$). Zoals verwacht zagen we dat de T_1 van malanotische laesies lager was dan van amelanotische laesies(888 ms vs 1350 ms, $p=0.03$). De gemiddelde K^{trans} was 0.46 min^{-1} (0.13–1.0) en de gemiddelde v_e was 0.22 (range 0.10–0.51). Uit dit onderzoek blijkt dat oogspecifieke analyse van perfusiescans mogelijk is. Deze methode heeft potentie om bij te dragen aan de diagnose, prognose en het vervolgen van oogmelanoompatiënten.

De verschillende hoofdstukken vormen samen een sterke basis voor het klinische gebruik en verder vervolgonderzoek naar toepassingen van MRI voor het verbeteren van het diagnosticeren, behandelen en opvolgen van patiënten met een oogmelanoom .

Acknowledgements

This work would not have been possible without the support of many individuals. On this page I would like to express my gratitude to them.

First of all, Jan-Willem, your skill to introduce new techniques into the clinic has is inspiring and has opened the doors for my clinically oriented and multidisciplinary research projects. I would like to thank you for all the critical questions and feedback on my research. I have appreciate our conversations, professionally and personally very much.

Prof. Webb, dear Andrew, thank you for creating such a vibrant and open research group where I felt welcome and support professionally and personally. I am grateful for being a part of the Gorter group. I enjoyed the inspiring conversations with people from different sides of MRI research and fun during conferences and social events such as the Friday afternoon drinks and game night.

Prof. Luyten, dear Gré, thank you for the trust and support you have given me. I really admire your willingness to step outside the box in research but also in management. I for example found that adding a physicist to the medical staff exemplary.

I would like to thank my colleges from Ophthalmology, Radiology and Radiation oncology departments. Berit, Bianca, Clair, Coen, Eleftheria, Guido, Jaco, Laura, Liset, Marcel, Marina, Myra, Teresa, Khanh, Yvonne, Wouter and the MRI technicians thank you for your contributions to the different projects. The time and effort you all put into these projects made it possible to also implement part of this research into the clinic. I am also very grateful for all patients and volunteers who were willing to participate in the different studies. Being scanned at least ones can be quite an intense experience especially as scans where often performed shortly after receiving the life changing diagnosis of uveal melanoma.

MR-EYE colleges, Kevin, Kilany, Lisa, Lorna, Luc, Michael, Niels and all intern thank you for the inspiration, willingness to help and most of all the fun we had together. I have fond memories of our escape rooms and dinners during our outings. I also cherish the conversations and support from my office mates, Nathalie, Thomas, Wyger, and Yiming. Especially with you Nathalie it sometimes was difficult to work at the office when we were there together as we always had something to talk about.

I am thankful to my friends from Bodegraven and Enschede for distractions when I needed them, and for patience in busy times.

Finally, I would like to thank my family for always showing their interest along the way. I especially thank my mom, my dad, Ruben and Tobian, without your continued love and support, I would not have been where I am now.

Curriculum Vitæ

Myriam Jaarsma-Coes was born on the 12th of June 1991 in Gouda. After graduation from Kalsbeek college she studied Technical Medicine at the University of Twente. She finished her bachelor in 2014 and continued her master in Medical Imaging and Interventions, where she did internships at the department of Orthopaedics (University Medical Center Utrecht, UMCU), department of Vascular surgery (St. Antonius), Intensive Care (UMCU) and at Brain Science Tools BV. In 2017 she received her master's degree in Technical Medicine at the University of Twente after having worked on quantification and analysis of white matter hyper-intensity features on MRI at the UMCU which has led to publication in at least seven journal papers. In November 2017 she started her PhD within the protons4vision project at the department of Radiology and Ophthalmology of the Leiden University Medical Center (LUMC). The results of her PhD research are described in this thesis. In January 2022 she was appointed as business intelligence developer at st Jansdal hospital where she continues her aim to improve patient care from a different perspective.

List of Publications

1. **M.G. Jaarsma-Coes**, T.A. Goncalves Ferreira, M. Marinkovic, T.H. Khanh Vu, L. van Vught, G.R. van Haren, M.F. Rodrigues, Y.L.B. Klaver, B.M. Verbist, G.P.M. Luyten, C.R.N. Rasch, J.W.M. Beenakker *Comparison of MRI-based and conventional measurements for proton beam therapy of uveal melanoma*, Ophthalmology Retina in press (2022).

2. T.A. Goncalves Ferreira, **M.G. Jaarsma-Coes**, M. Marinkovic, B. Verbist, R.M. Verdijk, M.J. Jager, G.P.M. Luyten, J.W.M. Beenakker *MR imaging characteristics of uveal melanoma with histopathological validation.*, Neuroradiology **64.1**, 171-184 (2022).

3. M.K. Hassan, E. Fleury, D. Shamonin,L. Grech Fonk, M. Marinkovic, **M. Jaarsma-Coes**, G.P.M. Luyten, A. Webb, J.W.M. Beenakker, B. Stoel *An automatic framework to create patient-specific eye models from 3D MR-images for treatment selection in patients with uveal melanoma*, Advances in Radiation Oncology **6.6**, 100697 (2021).

4. M.C.Y. Tang, **M. Jaarsma-Coes**, T.A. Ferreira, L. Zwirs - Grech Fonk, M. Marinkovic, G.P.M. Luyten, J.W.M. Beenakker *A Comparison of 3 T and 7 T MRI for the Clinical Evaluation of Uveal Melanoma*, Journal of Magnetic Resonance Imaging **55.5**, 1504-1515 (2022).

5. **M.G. Jaarsma-Coes**, T.A. Ferreira, P.J. van Houdt, U.A. van der Heide, G.M.P Luyten, J.W.M. Beenakker *Eye-specific quantitative dynamic contrast-enhanced MRI analysis for patients with intraocular masses*, MAGMA **35.2**, 311-323 (2022).

6. M.H.T. Zwartbol, R. Ghaznawi, **M. Jaarsma-Coes**, H.J. Kuijf, J. Hendrikse, J. de Bresser, M.I. Geerlings *White matter hyperintensity shape is associated with cognitive functioning - the SMART-MR study*, Neurobiology of Aging (2022).

7. F. Inglese, **M.G. Jaarsma-Coes**, G.M. Steup-Beekman, R Monahan, T Huizinga, M.A. van Buchem, I Ronen, J. de Bresser *Neuropsychiatric systemic lupus erythematosus is associated with a distinct type and shape of cerebral white matter hyperintensities*, Rheumatology (2021).

8. R. Ghaznawi, M.I. Geerlings, **M.G. Jaarsma-Coes**, J. Hendrikse, J. de Bresser *Association of White Matter Hyperintensity Markers on MRI and Long-term Risk of Mortality and Ischemic Stroke*, Neurology **96.17**, e2172-e2183 (2021).

9. I.M.J. Kant, A.J.C. Sloter, **M.G. Jaarsma-Coes**, S.J.T. van Montfort, T.D. Witkamp, J. Hendrikse, J. de Bresser *Preoperative MRI brain phenotypes are related to postoperative delirium in older individuals*, Neurobiology of Aging **101**, 247-255 (2021).

10. E. Fleury, P. Trnkova, E. Erdal, M. Hassan, B. Stoel, **M. Jaarsma-Coes**, G. Luyten, J. Herault, A. Webb, J.M.W. Beenakker, J.-P. Pignol, M. Hoogeman *Three-*

dimensional MRI-based treatment planning approach for non-invasive ocular proton therapy, Medical Physics / Early View (2020).

11. M.H.T. Zwartbol, R. Ghaznawi, **M. Jaarsma-Coes**, H.J. Kuijf, J. Hendrikse, J. de Bresser, M.I. Geerlings *The association between white matter hyperintensity shape and cognitive functioning: The SMART-MR study*, Alzheimer's & Dementia **16.S4** (2020).

12. **M.G. Jaarsma-Coes**, M. Marinkovic, E. Astreinidou, M.S. Schuurmans, F.P. Peters, G.M.P Luyten, C.R.N. Rasch, J.W.M. Beenakker *Measuring eye deformation between planning and proton beam therapy position using magnetic resonance imaging* , Phys Imaging Radiat Oncol. **16**, 33-36 (2020).

13. T.A. Goncalves Ferreira, C.F. Pinheiro, P. Saraiva, **M.G. Jaarsma-Coes**, S.G. van Duinen, S.W. Genders, M. Marinkovic, J.W.M. Beenakker *MR and CT Imaging of the Normal Eyelid and its Application in Eyelid Tumors*, Cancers **12.3**, 658 (2020).

14. **M.G. Jaarsma-Coes**, T.A. Ferreira, G.P.M. Luyten, J.W.M. Beenakker *Reaction on "Ocular ultrasound versus MRI in the detection of extrascleral extension in a patient with choroidal melanoma"*, BMC Ophthalmol. **19.1**, 193 (2019).

15. I.M.J. Kant, H.J.M.M. Mutsaerts, S.J.T. van Montfort, **M.G. Jaarsma-Coes**, T.D. Witkamp, G. Winterer, C.D. Spies, J. Hendrikse, A.J.C. Sloter, J. de Bresser, BioCog Consortium *The association between frailty and MRI features of cerebral small vessel disease*, Sci Rep. **9.1**, 11343 (2019).

16. T.A. Goncalves Ferreira, L. Grech Fonk, **M.G. Jaarsma-Coes**, G.R. van Haren, M. Marinkovic, J.W.M. Beenakker *M̈RI of Uveal Melanoma* , Cancers **11.3**, 377 (2019).

17. **M.G. Jaarsma-Coes**, T.A. Goncalves Ferreira, G.R. van Haren, M. Marinkovic, J.W.M. Beenakker *M̈RI enables accurate diagnosis and follow-up in uveal melanoma patients after vitrectomy*, Melanoma Res. **29.6**, 655-659 (2019).

18. **M.G. Jaarsma-Coes**, R. Ghaznawi, J. Hendrikse, C. Slump, T.D. Witkamp, Y. van der Graaf, M.I. Geerlings, J. de Bresser on behalf of the SMART Study Group *MRI phenotypes of the brain are related to future stroke and mortality in patients with manifest arterial disease: The SMART-MR study.*, J Cereb Blood Flow Metab **40.2**, 354-364 (2020).

19. R. Ghaznawi, M.I. Geerlings, **M.G. Jaarsma-Coes**, M.H.T. Zwartbol, H.J. Kruijf, Y. van der Graaf, T.D. Witkamp, J. Hendrikse, J. de Bresser on behalf of the SMART Study Group *The association between lacunes and white matter hyperintensity features on MRI: The SMART-MR study*, J Cereb Blood Flow Metab **39.12**, 2486-2496 (2019).

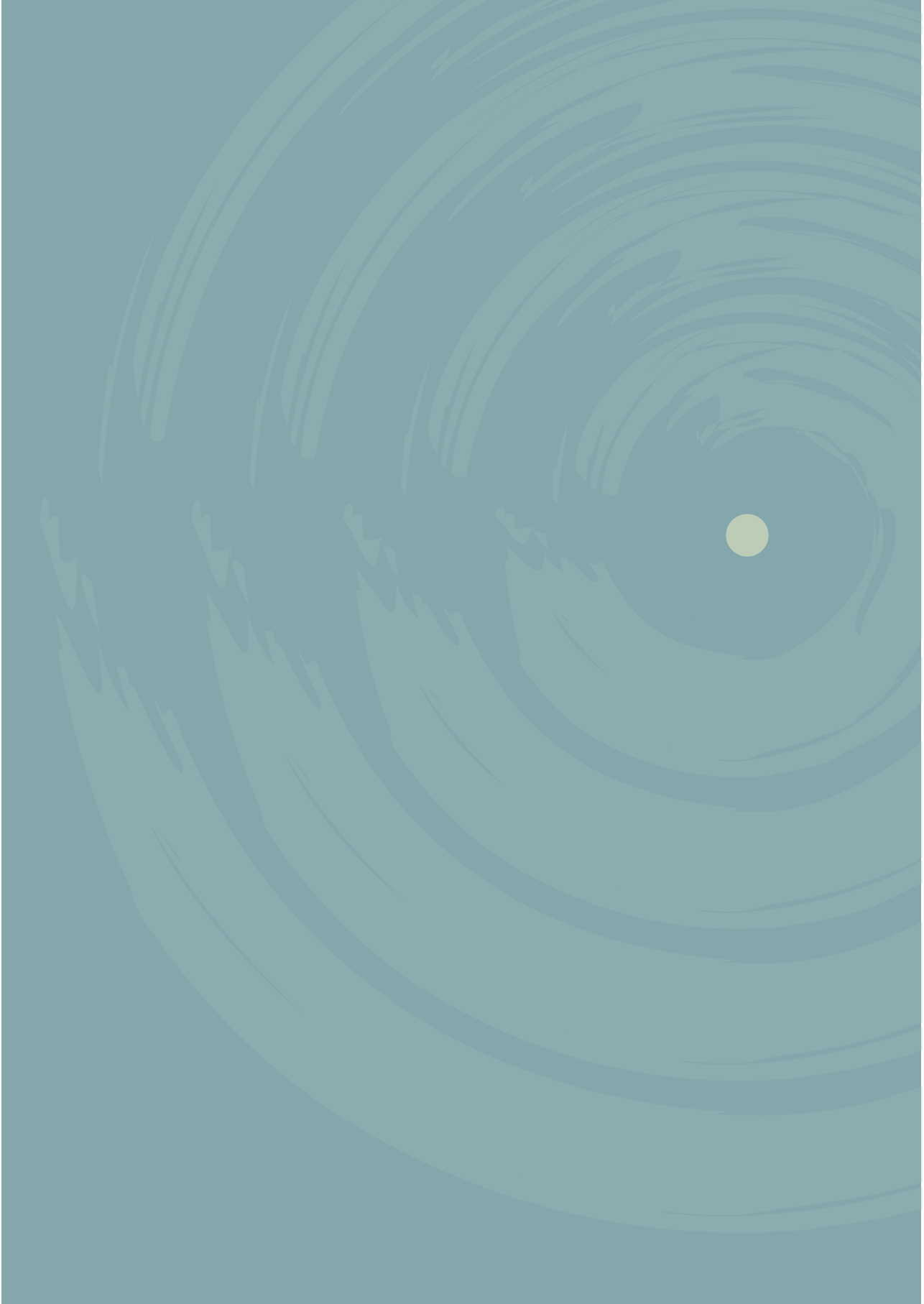

Stellingen

behorende bij het proefschrift

MRI for planning and characterization of uveal melanoma patients treated with proton beam therapy

door

Myriam Jaarsma-Coes

1. MRI scans acquired in prone position can be used to plan seated ocular proton beam therapy.*(this thesis)*
2. MRI-based tumour segmentation will in most patients provide a more accurate representation than a geometric model based on ultrasound. *(this thesis)*
3. Implementation of MRI into the proton beam therapy planning work-flow is an essential step to improve the visual outcome of uveal melanoma patients. *(this thesis)*
4. Pharmacokinetic modelling is most likely the future of metastatic risk prediction for uveal melanoma patients. *(this thesis in combination with Ferreira et al. Neuroradiology.,2022 https://doi.org/10.1007/s00234-021-02825-5)*
5. All uveal melanoma patients with a prominence over 6 mm on ultrasound and more than one treatment option should be offered a pre-treatment MRI.
6. As parts of the intra-ocular tumour can be missed on non-contrast-enhanced MR-Images, MRI for ocular oncology should at least include contrast administration and preferably be performed at 3T. *(in reply to the conclusion of Via et al. j.radonc.,2022 https://doi.org/10.1016/j.radonc.2022.06.021)*
7. Communication between ophthalmologists and radiologist is essential to maximize the clinical benefit of MRI scans.
8. Multidisciplinary cooperation is essential to move the field of uveal melanoma research forward.
9. All hospitals and all departments of an academic hospital should employ at least one technical physician.